FACULTY OF SCIENCE
UNIVERSITY OF COPENHAGEN

Master of Science in Physics at the Niels Bohr Institute

Spectroscopy of Advanced Integrated Nanophotonic Devices and Quantum Dots

Adam S. Knorr

jmb649@alumni.ku.dk

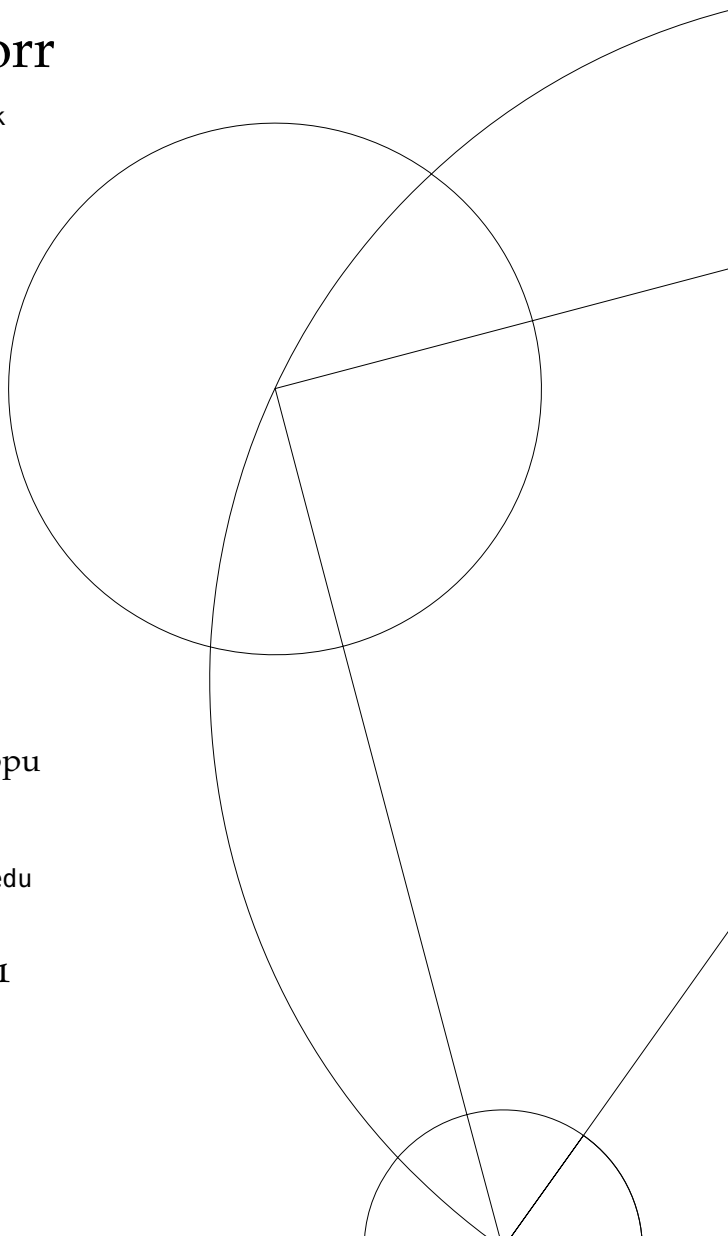

Prof. Peter Lodahl

Asst. Prof. Ravitej Uppu

lodahl@nbi.ku.dk

ravitej-uppu@uiowa.edu

17th of May, 2021

Adam S. Knorr: *Spectroscopy of Advanced Integrated Nanophotonic Devices and Quantum Dots* , Master of Science (Cand.scient.), © 17th of May, 2021

SUPERVISORS:
Prof. Peter Lodahl
Asst. Prof. Ravitej Uppu

ABSTRACT

A quantum mechanical based internet requires efficient generation, collection and manipulation of photonic quantum bits (qubit). Semiconducting quantum dots have shown great promise in fulfilling the required role of a single-photon emitter in generating qubits. Polarization entangled photonic qubits can also be generated through cascaded emission from a "twice-excited" quantum dot namely the biexciton. Efficient collection of linearly polarized quantum dot emission can be done at near unity efficiency when coupled to the highly symmetric photonic crystal waveguide.

In this thesis: A low strain GaAs semiconducting quantum dot features small fine structure splitting compared to the more wide spread InAs type of quantum dot. Low fine structure splitting is desirable for stable entangled photon generation, which can be produced with the biexciton cascade. The GaAs quantum dot can also be operated as a single photon source and so its single photon properties are measured and compared to the state-of-the-art InAs single photon source. The biexciton is also excited in the quantum dot and its decay rate is measured.

With low fine structure splitting the otherwise linearly polarized photon states from the biexciton cascade degenerates, producing circularly polarized photons instead. A new type of photonic crystal "the glide-plane waveguide" has parity broken symmetry, leading to circular polarization solutions to the Bloch equations, which from time reversal symmetry induces chiral coupling of circular polarized light from emitters in the glide-plane waveguide. This also opens the possibility of transforming polarization entangled sources e.g. cascaded emission from a GaAs biexciton, to path entangled sources. The coupling capabilities of a quantum dot to the glide-plane waveguide is measured with resonant transmission spectroscopy. The quantum dot resonance is controlled with induced Stark shift and resonant fluorescence is performed across multiple voltages, displaying great control of quantum dots in the glide-plane environment.

Topological photonics promise reduced backscattering for edge-mode transmission between two topologically distinct insulators. This has the possibility of greatly increasing on chip propagation efficiency. Experimentally the topological edge mode is found in topologically interfaced devices, and the transmission through the devices is characterized. A method of characterizing the group index of the nanobeam waveguides and topological devices is proposed and performed. Results are compared with simulations seeming to agree besides for some systematic errors.

SAMMENFATNING

Realisering af et kvantemekanisk baseret internet kræver effektiv generering, samling og manipulation af fotoniske kvante bits (qubit). Halvleder kvantepunkter har vist sig at opfylde alle af de kriterier, der stilles til en enkelt-fotons kilder til generering af fotoniske qubits. Kvantepunkter kan også generere polarisations-entangled qubits igennem emissions kaskaden fra et kvantepunkt i en dobbelt exciteret tilstand – en biexciton. Effektiv indsamling a lineært polariseret emission fra kvantepunkter placeret i yderst symmetriske nanofotoniske strukturer såsom den fotoniske krystal bølgeledere kan nå nær 100 procent effektivitet. I denne afhandling: En lav stress GaAs halvlederkvantepunkt har en mindre finstruktur splitning sammenlignet med de mere gængse InAs kvantepunkter. En lille finstruktur splitning er favorabel for stabil produktion af entangled fotoner genereret igennem biexcitonskaskaden. GaAs kvantepunkter har også potentiale til at være en god kilde af enkelt-fotoner, så deres enkelt-foton egenskaber bliver målt og sammenlignet med en af nutiden bedste InAs baserede enkelt-foton kilder. Biexciton tilstanden bliver også produceret og dens henfaldsrate bliver målt. Med en lille finstruktursplitning bliver den ellers lineært polariserede foton tilstand fra biexcitonkaskaden cirkulært polariseret i stedet. En ny slags fotonisk crystal "glideplan bølgelederen" har brudt paritets symmetri, hvilket medføre løsningerne til Bloch ligningerne der gennem "omvendt tids symmetri" tillader cirkulær polarisation og chiral kobling af lys. Dette åbner op for muligheden for at omdanne en polarisations-entangled kilde fx biexcitonkaskaden fra GaAs til en vej-entangled kilde. Hvor godt et kvantepunkt kobler til strukturen bliver målt med resonant transmission spektroskopi. Kvantepunktets resonans kan kontrolleres med et eklektisk felt induceret Stark shift. Resonant fluorescens bliver påvist over flere spændingsfald, og viser god kontrol over kvantepunktet i glideplan bølgelederen. Topologisk fotonik gisner om reduceret tilbage refleksion i en transmitterende kanttilstand imellem to forskellige topologiske isolerende materialer. Dette skaber muligheder for at forøge de effektive lysudbredelses distancer i halvledere. Eksperimentalt bliver den topologiske kanttilstand bliver fundet i topologiske nanostrukturer og transmissionen igennem strukturerne bliver karakteriseret. En metode, til hvordan man kan finde gruppe indeks af nanobjælke bølgeledere og topologiske strukturer bliver brugt, og målingerne, udover nogle systematisk fejl, stemmer overens med simuleringer.

ACKNOWLEDGEMENTS

I would like to acknowledge Peter Lodahl, for enabling all the great time I have spent in the lab and with the group, Hy-Q is a great place to be and you take less credit than you deserve for surrounding yourself with lovely people.
Ravi, for all the countless things you have taught me, as well all the countless hours we have spent in the lab together.
Freja, for always being there when i had a question or needed help.
Nils, for introducing me to the wild west that is topology and taking me on a journey there.
I also want to thank the entire Hy-Q group for creating an environment that makes it fun, interesting and exciting to do research in.
Lastly i want to thank my good friends, supportive family and lovely girlfriend, who supported me along the way.

INTRODUCTION

The World Wide Web was invented in 1989 when Sir Tim Berners-Lee wrote a proposal to the CERN management of a new method for sharing information between an enormous set of computers (Berners-Lee [1]). This was the start of a technological revolution which has lead to the modern era today where internet is an integral part of technological infrastructure, entertainment and communications.

Quantum supremacy! In October 2019 scientists at Google showcased that they had successfully operated a quantum computer manipulating 53 quantum-bits to perform a calculation in 200 seconds, that same calculation on a state-of-the-art supercomputer would take 10.000 years (Arute et al. [2]). This is by many seen as the first big step into a new era of quantum technology.

In the new quantum era the realization of a quantum internet is the next big step (Kimble [3]).

Where the classical internet relies on information encoded in bits of light either off(0) or on(1) the quantum internet relies on information encoded in quantum bits (qubits), made of single-photon states $|0\rangle$ and $|1\rangle$ and super positions thereof $a|0\rangle + b|1\rangle$ with $|a|^2 + |b|^2 = 1$. Using qubits the quantum internet can feature secure transfer through quantum key distribution and encryption utilizing the BB84 protocol (Bennett and Brassard [4]). The BB84 protocol relies on qubits for information transfer which cannot be measured without being destroyed, and also can not be cloned (Wootters and Zurek [5]). This allows certain detection of potential eavesdroppers, whom would only acquire partial information from eavesdropping on quantum based communication. Such secure communication is necessary in the new quantum era since, the current method of encrypting messages on the internet (RSA) can be broken in record time on quantum computers using Shor's algorithm (Shor [6]).

Realization of quantum communication protocols like BB84 require deterministic on-demand single photon generation. In recent years semiconducting quantum dots coupled to integrated nanophotonic structures have shown to be great contenders to this end (Lodahl, Mahmoodian, and Stobbe [7]). Semiconducting quantum dots in coupled nanophotonic devices can produce rapid, efficient and consistent single photons, with Uppu et al. [8] demonstrating a InAs quantum dot producing 122 million photons per second, at 84% efficiency, while more than 100 photons in a row are highly indistinguishable. This source is the current state-of-the-art.

One of the problems with BB84 is the if two people Alice and Bob wish to communicate they both require the means of producing and

measuring single photons. The E91 protocol (Ekert [9]) solves this issue, by having a third party, which could even be an eavesdropper create entangled photon states which are then sent to Alice and Bob, and still provides secure quantum key distribution. Single photons can be interfaced in a Mach-Zehnder interferometer to produce a path entangled state that can be used for communication protocols like E91. But a method to skip this extra step is to produce an entangled photon source directly. This can be done using a "twice-excited" state of a quantum dot called the biexciton (Lodahl, Mahmoodian, and Stobbe [7]). The biexciton decays in a cascade releasing two photons in rapid succession. The two photons are inherently circular polarization entangled (Oliver Benson and Yamamoto [10]).

Due to the no-cloning theorem (Wootters and Zurek [5]) efficient transport photon qubits is highly sought after. Since loss of qubits can significantly slow down communications, or not have it occur at all. One of the limitation of integrated nanophotonics is that light propagation in semiconducting material suffer from back-reflections (Ling Lu and Soljačić [11]). This reduces the success rate of quantum protocols performed on a photonic chip.

In this thesis I will investigate three recent proposed advancements within quantum dots and photonics:

1) Droplet GaAs in AlGaAs quantum dots are highly symmetric due to their growth method and low strain between the semiconducting lattices, this gives them an inherent low fine structure splitting. When generating entangled photons through the biexciton cascade unintentional fine structure splitting in a quantum dot projects the polarization into a linear basis which adds a random phase to the entangled state which reduces the consistency and thereby efficiency of the source (Keil et al. [12])(Huber et al. [13]). The GaAs droplet dots feature a low fine structure splitting compared to InAs quantum dots which makes it a better candidate for an entangled photon source. Droplet dots have also been shown to produce good single photon properties (Schöll et al. [14][15]). Spectroscopy droplet GaAs quantum will be presented, and biexciton excitation performed.

2) Common photonic waveguides are symmetric, solutions of possible intra electric fields of these structures are predominantly linearly polarized due to parity symmetry (Joannopoulos et al. [16]). This is great for single photon sources, but circular polarized light from e.g. low fine structure splitting biexciton cascades is suppressed. A new photonic structure, the glide-plane waveguide allows circular polarization dependent chiral coupling through a parity symmetry break of the photonic crystal lattice (Mahmoodian et al. [17]). Meaning it predominantly couples circular polarized light. And it can be used to convert polarization to path entanglement of an emitter located in a chiral point in the glide-plane waveguide. Spectroscopy of glide-plane

waveguides will be presented, and an InAs quantum dot is coupled to the waveguide.

3) Transferring quantum information requires extremely high efficiency (Gisin et al. [18]), one limiting factor in the efficiency budget is backscattering, at every interface or defect there is a probability light is reflected and lost. With many interfaces or long distances this quickly adds up. A proposed way of reducing backscattering is through topologically protected edge states where propagation is theorized to be unidirectional even under significant defects making backscattering effects heavily suppressed (Ling Lu and Soljačić [11]). Spectroscopy of topological devices will be presented for characterization of the edge mode.

Topics and experiments are presented as follows:

Chapter 1. First an introduction necessary background knowledge for subsequent chapters. This includes introducing: Quantum dots as single photon sources, their decay dynamics, the entangled photon generation through the biexciton cascade, and how the quality of quantum dot emission is quantified. Next the nanophotonic devices used throughout the thesis are presented. At the end of the chapter an introduction to general topological photonics is presented with specifics presented in a later chapter.

Chapter 2. The different methods of spectroscopy utilized throughout the thesis are introduced and compared. This includes different excitation methods of the quantum dot, and transmission measurements of nanophotonic devices. Experimental set-ups and equipment utilized are also introduced here.

Chapter 3. This chapter focuses on quantifying the emission of a droplet quantum dot. This includes probing the coupling to a photonic nanostructure and single photon properties under different excitation methods. The chapter also features biexciton excitation and measurement of the decay rate. The chapter concludes with the design of the next generation of the sample featuring GaAs quantum dots.

Chapter 4. The transmission of glide-plane waveguides is measured. An InAs quantum dot is probed with excitation through the waveguide quantifying coupling between quantum dot and waveguide. Next resonant fluorescence is performed on a quantum dot in a glide-plane, and tuned by inducing Stark shift in the quantum dot. The quantum dot lifetime is also measured. At the end of the chapter a measurement of polarization-dependent AC-Stark shift in the quantum dot emission is performed.

Chapter 5. Transmission of topological waveguides and insulators is compared in the search for edge modes and the photonic parameter space's influence on edge mode transmission is characterized. At the

end of the chapter a method is presented for measuring the group index of the topological devices.

Chapter 6 will round up results presented in the thesis and present an outlook to further developments.

CONTENTS

1 QUANTUM DOTS AND NANOSTRUCTURES

1.1 QUANTUM DOTS - SINGLE PHOTON EMITTERS

Semiconducting quantum dots exploit the discretization of the conduction,- and valance band energy levels when confined in a small space, analogous to the famous particle in a well (Lodahl, Mahmoodian, and Stobbe [7]). Here the potential walls are created by a bulk semiconducting material with a higher energy bandgap while the bottom of the well itself is a semiconductor with a smaller bandgap (see Figure 1). By changing the size of the quantum dot the discrete energy levels of the semiconductor also change. Engineering these quantum dots and the environment to emit into different frequencies by selecting the semiconductor and altering their size is one of the many advantages of quantum dots.

Figure 1: Scanning tunneling microscope (STM) image of a InAs quantum dot grown on GaAs. Figure is adapted from (Marquez, Geelhaar, and Jacobi [19])

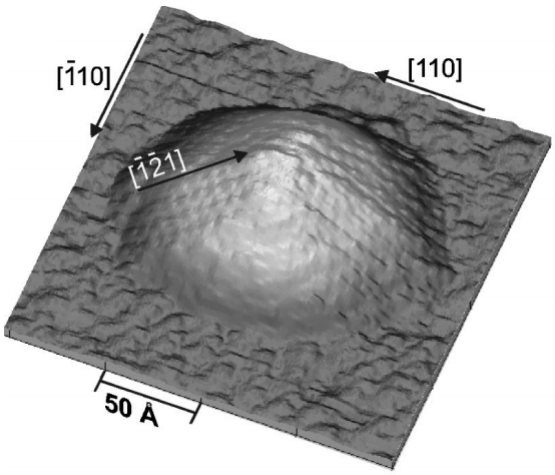

When exciting a quantum dot an electron excites from the valence band to the conduction band while creating a hole where it left. In quantum dots the electron-hole entity is called an exciton (see fig. 2). The exciton can undergo recombination where the electron $\left(\text{spin: } J_e = \pm\frac{1}{2}\right)$ and hole $\left(J_h = \pm\frac{3}{2}\right)$ merge producing a photon in the process. Recombination requires the electron-hole to have different spin e.g. $|\uparrow\Downarrow\rangle$ to produce a spin ± 1 photon. Recombination is a spontaneous process, making it very similar to spontaneous emission of atoms that happens randomly with an exponential decay with rate γ_{rad}. While excited the electron can undergo a spin-flip, this puts

Figure 2: Different excitation schemes of quantum dot. Left: Bright exciton $|X_b\rangle$ displayed with its coupling γ_{db} to a dark state $|X_d\rangle$. The energy difference between the bright and dark state is usually negligible unless a magnetic field is present. Excitons spin-flipping to the dark state produces blinking. Centre: Exiton level split by the FSS of the quantum dot, where the two states $|X_b\rangle$ and $|Y_b\rangle$ are bright excitons with respectively $\frac{1}{\sqrt{2}}(|\downarrow\Uparrow\rangle \pm |\uparrow\Downarrow\rangle)$ spin-hole configurations. Recombination produces respectively horizontal and vertically polarized photons. Right: By exciting two excitons within the quantum dot at the same time a biexciton state $|XX\rangle$ is produced. Figure adapted from (Lodahl, Mahmoodian, and Stobbe [7]).

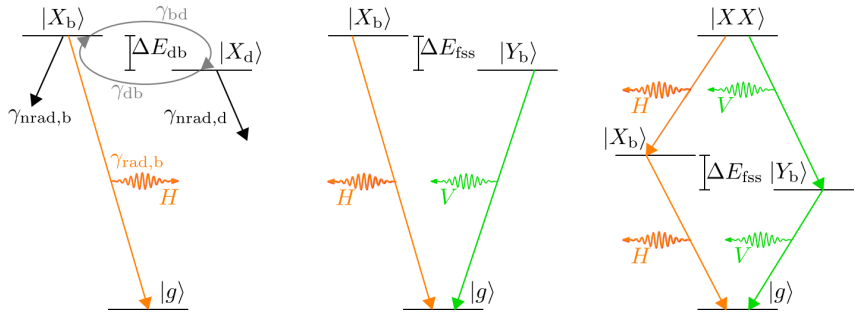

the exciton into a "dark state" $|X_d\rangle$ where it is unable to recombine. This effectively creates a time window where the quantum dot if "off". Spin-flipping back into a "bright state"$|X_b\rangle$ re-enables the operation of the quantum dot, this on-off switching is called blinking and is a highly undesirable trait of the quantum dots, since it reduces the overall brightness of the dot but more importantly blinking can greatly increase the effective decay rate. If one wishes to operate a blinking quantum dot deterministically, it has to be done slower than the blinking which can be thousands of times slower.

Due to strain on the quantum dot its excited state becomes non-degenerate and splits with a fine structure splitting (FSS). The exciton has two bright states $|X_b\rangle = \frac{1}{\sqrt{2}}(|\downarrow\Uparrow\rangle + |\uparrow\Downarrow\rangle)$ and $|Y_b\rangle = \frac{1}{\sqrt{2}}(|\downarrow\Uparrow\rangle - |\uparrow\Downarrow\rangle)$, split in energy by the fine structure splitting of the quantum dot.

It is possible to excite the quantum dot with two simultaneous excitons known as the biexciton. Due to the Pauli exclusion principle they are ensured to have different spin. The first recombination of the two produce lower energy than the exciton due to Coulomb interaction between the two excitons. To excite the biexciton two photons, with higher energy than the Columb interaction plus resonance, have to excite the quantum dot at exactly the same time. Consistent excitation to the biexciton therefore requires high power, which is often obtained though pulsed laser action. The biexciton emission cascade can be used as a single photon source but also as a entangled photon source (see more in Section 1.1.3).

When operating quantum dots dipoles with pulsed action, their excitation can be described by the Rabi model (Gerry and Knight [20]). The Rabi model describes the probability of exciting a Two Level

System (TLS). The probability depends on the laser detuning from the TLS resonance Δ as well as the light-matter interaction $\mathcal{V} = -\hat{\mathbf{d}} \cdot \mathbf{E}_0$ between the laser field $\mathbf{E}_0$ and TLS dipole moment $\hat{\mathbf{d}}$. These together constitute the Rabi frequency $\Omega_R = \sqrt{(\Delta^2 + \mathcal{V}^2)}$. The probability of exciting the TLS oscillates as $P_e(t) \propto \sin^2(\frac{\Omega_R \cdot t}{2})$. By increasing laser power that enters through the Rabi frequency can be tuned to the pulse duration t such that: $P_e = 1$, this happens when a phase π is produce yielding the highest probability of exciting the quantum dot and so dubbed a π-pulse. This can be used for finding the pumping power of the quantum dot under pulsed action.

Quantum dots sit in local charge environments dependant on the bulk semiconductor and eventual modifications to it. This is not a stable environment as charges can flow in and out of the quantum dot at random. Whenever an electron enters the quantum dot the emission is shifted in a process called spectral diffusion, effectively increasing the linewidth of quantum dot emission. Placing a quantum dot into a controlled charge environment (such as in a capacitor) can change the Fermi level of the quantum dot, thereby controlling the amount of electron states available in the quantum dot, reducing noise spectral diffusion. Either adding or subtracting electrons from the quantum dot changes the recombination energy to a new level. These states are called the positive and negative charge excitons $|X^+\rangle$ and $|X^-\rangle$. These will not be explored in this thesis but their existence is worth acknowledging. Another benefit of controlling the quantum dot charge environment is producing a Stark shift. In between the abrupt emission changes from an electron breaking the Coulomb blockade and flowing into the quantum dot, the quantum dot will tune linearly in emission with an applied electric field. The tuning arises from the field straining the dot to either expand or contract.

Similar to how quantum dot emission can change by applying a DC electric field, this is also true for AC-fields. When the quantum dot experiences a strong oscillating electric field e.g. Laser light it experiences the AC-Stark effect(M. Kroner and Karrai [21]). In a nutshell the AC-Stark effect tunes the quantum dot emission with laser power. Complete mapping of the frequency shifts from AC-Stark effect for quantum dots is difficult since it relies heavily on the individual quantum dot size and shape. To give a rough reference of the scale of the effect, in: M. Kroner and Karrai [21] they measured the shifts below saturation to ~ 9 GHz/μW.

1.1.1 *Selfasembled InAs/GaAs Quantum dots*

For this thesis two different kinds of quantum dots are studied: The more widely used self assembled InAs in GaAs quantum dots, and the less explored but promising droplet GaAs is AlGaAs quantum dots.

Self-assembled InAs quantum dots in GaAs, are currently the overall best performing single photon emitter (Uppu et al. [8]). They are the main workhorse when it comes to producing: Rapid, low second order correlations, highly indistinguishable, single photons (I. Aharonovich [22]).

The quantum dots are grown using the Stranski-Krastanov method that utilizing the self-assembly of InAs on GaAs due to the lattice mismatch between the two [7]. Epitaxially growing monolayers of InAs on GaAs forms small clusters of InAs. The clusters are 15-20 nm in diameter and 5-10 nm in height (Pedersen [23]). After the clusters have formed, they are capped off with another layer of GaAs, completing the quantum dot. There is a certain randomness to the growth of these quantum dots as precise control of the size of the InAs clusters depends on the spontaneous self-assembly. The layers created before self assembly grow what is called a wetting layer which is a sort of alloy of the two semiconductors. The lattice mismatch that creates strain, also makes the quantum dots slightly elliptical. This makes the quantum dot dipoles differ slightly effectively introducing a fine structure splitting in the order of 2.5 - 25 GHz (Lodahl, Mahmoodian, and Stobbe [7]). High fine structure splitting is undesirable for creating an entanglement source, but it matters not for producing a good two-level single photon source and for InAs quantum dots it is difficult to circumvent.

1.1.2 *Droplet GaAs/AlGaAs Quantum dots*

Droplet quantum dots consist of GaAs embedded into AlGaAs. The creation of these dots involves a droplet of Al etching a hole into the AlGaAs wafer, wherein GaAs can be deposited, and then capped off (see Figure 3).

Figure 3: Droplet dot growth. Al droplets are scattered on the AlGaAs wafer, etching away a hole into the AlGaAs. By depositing a layer of GaAs fills the hole. Capping the hole off with AlGaAs finishes the creation of the quantum dot. Figure adapted from (Keil et al. [12]).

The strain between the AlGaAs and GaAs lattices is considerably lower than the InAs quantum dots and the droplet hole etching makes for a higher symmetry of the quantum dot. This allows the creation of droplet dots with consistently low FSS in the order of 0.5 - 1.4 GHz (Huo, Rastelli, and Schmidt [24]). This makes for an interesting candidate for a stable entangled photon source. Investigation into the single photon source properties of droplet quantum dots are also $g^{(2)}(0) = 7.4 \cdot 10^{-5}$ (Schöll et al. [15]).

1.1.3 *Entangled photon generation through the biexciton cascade*

Entangled photon states are core in the evolution of the quantum internet (Kimble [3]). The most commonly used photon entangled states are Bell states. Bell states constitutes a set of 4 orthogonal entangled states with maximum entanglement. A lot of (if not all) quantum information processes utilizing entangled states (e.g. E91 (Ekert [9])) have a higher success rate dependent on the "entangled-ness" of states. Let us therefore look at a method for producing maximally entangled states. The emission from the biexciton-exciton cascade is a two photon state here described in the linear polarization basis (similar to Huber et al. [13]):

$$|\psi(t)\rangle = \frac{1}{\sqrt{2}}\left(|H_{XX}H_X\rangle + e^{\frac{iSt}{\hbar}}|V_{XX}V_X\rangle\right) \tag{1}$$

$\psi(t)$ is an entangled photon state, where H_{XX} is a horizontally polarized photon emitted by the biexciton and V_X is a vertically polarized photon emitted from the exciton, and S is the FSS. When the biexciton decays it emits a photon and the quantum dot is placed in the exciton state, here it acquires a phase $\frac{St}{\hbar}$ before emitting again, producing the two photon state. For any $S \cdot t = n_i\pi$, ψ this is a Bell state, however regardless of phase it is still a maximally entangled state, it is just not orthogonal to Bell states but rather to another set rotated like itself. Protocols like E91 require that the entangled states form a perfect set, for completely secure communications. But if the source produces entangled states with random phases, it might not be as effective even though it is maximally entangled. The extra phase can be made up for by having λ plates to shift the entangled state back into phase with the Bell states, but that introduces efficiency loss and would require the λ plates to adapt to the spontaneous decay of the exciton, which is an extra step best to avoid. The most elegant solution is to get a better entangled photon source with low to zero FSS compared to the decay rate of the exciton state of the source Figure 4. Reducing the fine structure splitting makes the exciton state degenerate such that $|X\rangle = |\uparrow\Downarrow\rangle$. This makes it more favourable to examine the 2-photon state in the circular polarization basis.

In the circular polarization basis the two-photon state oscillates between two Bell states at a rate of the fine structure splitting.

$$|\phi^+\rangle = \frac{1}{\sqrt{2}}\left(|R_{XX}R_X\rangle + |L_{XX}L_X\rangle\right) \Leftrightarrow |\psi^+\rangle = \frac{1}{\sqrt{2}}\left(|R_{XX}L_X\rangle + |L_{XX}R_X\rangle\right) \tag{2}$$

So in the $S \approx 0$ a Bell state is always produced, but which one oscillates at a the interval of the fine structure splitting. The lower the fine structure splitting is the more easily manageable it becomes.

Figure 4: Comparison of the biexciton exciton cascade with significant and non significant fine structure splitting.

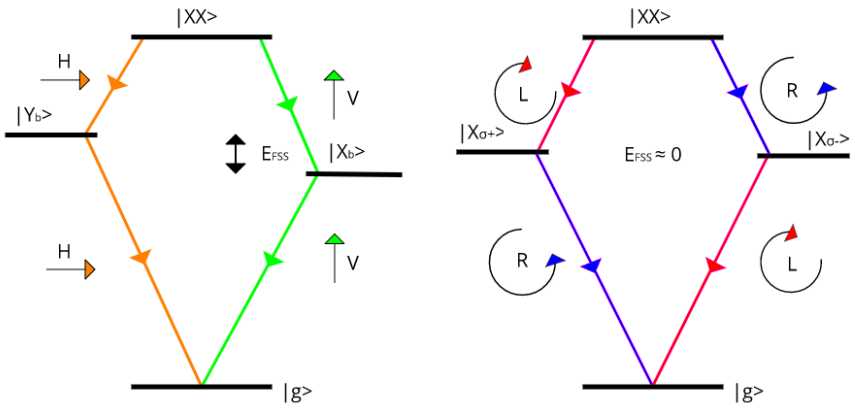

1.1.4 *Quantifying quantum dot emission quality*

In the beginning of this thesis I state that we require: "Rapid, efficient, and consistent" photon production. In this section i will touch on how these measures are quantified.

When we say we want rapid photons from a quantum dot it roughly translates to require excitons to have a short lifetime/fast decay rate. The spontaneous decay rate of a quantum state is governed by Fermi's golden rule (number 2 Gerry and Knight [20]). The rule states that spontaneous decay from one quantum state to a another specific state in a continuum is governed by the local density of states, and the transition strength which for light matter interaction is governed by the dipole moment. A by-product of the rule is that by reducing the amount of available states spontaneous decay to the remaining states is increased. This led E. Purcell to discover the Purcell factor (Purcell [25]) for optical states in resonators, which has later led on to a more generalized expression of Purcell enhancement (Lodahl, Mahmoodian, and Stobbe [7]):

$$F_p = \frac{\gamma_{rad}}{\gamma_{hom,rad}} \tag{3}$$

Where F_p is the Purcell factor describing how fast an enhanced decay γ_{rad} is compared to a decay rate in a homogeneous medium $\gamma_{hom,rad}$. The optical environment of the quantum dots can be controlled to reduce the local density of optical states and thereby allows great Purcell enhancement which increases emission rates. High Purcell enhancement is desirable for increasing the rapidity of photon generation for quantum technology.

Figure 5: Hanury-Brown Twiss optical experiment. A light source (here a quantum dot) is excited and emits onto a beam splitter. If one photon enters at a time, only one detector will click at a time giving a $g^2(0) = 0$. However if two photons enter sometimes the photons will split 50:50 and both detectors click at the same time giving a $g^2(0) = 1$. If multiple photons enter at the same time $g^2(0) > 1$. The two paths of the beamsplitter might not be completely the same length but an adaptable time delay τ allows for the calibration.

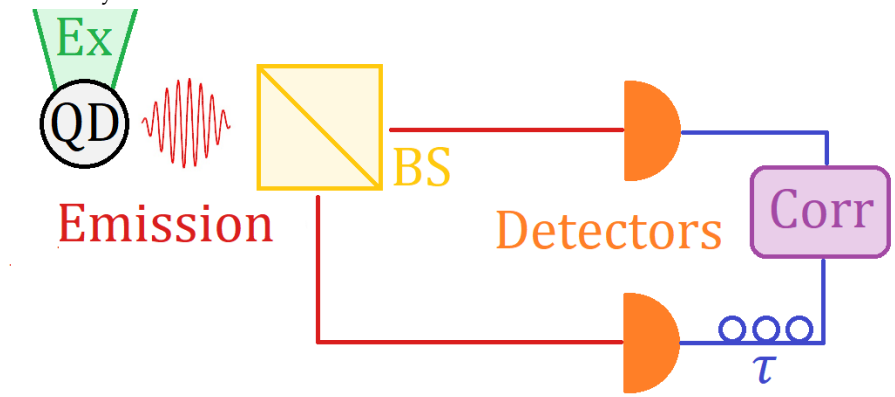

A single photon source is most efficient when it emits actual single photons. This can be quantified through the second order correlation function:

$$g^2(t,\tau) = \frac{\langle a^\dagger(t)a^\dagger(t+\tau)a(t+\tau)a(t)\rangle}{\langle a^\dagger(t)a(t)\rangle^2} \tag{4}$$

Where $a(t)$ & $a^\dagger(t)$ are the field destruction and creation operators at time t and $t+\tau$. The function is best understood in the respect to the Hanbury-Brown Twiss (HBT) experiment (Brown and Twiss [26])(see Figure 5).

In layman's terms the $g^2(t,\tau)$ is an expression of how often two photons are created at time t and τ. Usually t is fixed at zero making a great single photon source have $g^2(\tau = 0) = 0$, meaning that two photons *never* occur in the two detectors at the same time. However this is very difficult, and a lot of systematic errors often enter. Background light can enter into the experiment and give a false two photon detection. Coherent sources like lasers function through stimulated emission where photons are always created in pairs. This gives them a $g^2(\tau = 0) = 1$. Therefore if laser light leaks from the quantum dot excitation into the HBT experiment, the measured g^2 will be increased. Of cause there is also the probability that the source does not always produce single photons. Pulsed and continuous excitation will produce different $g^2(\tau = 0)$. Under continuous excitation the single photon source should have $g^2(\tau) \approx 0$ while the correlation of two photons at all other time delays should be 1. For pulsed excitation we see correlation peaks going to 1 at a separation of the time between laser pulses, while remaining near 0 at $\tau = 0$. g^2 measurements are also great for detecting blinking, which will be seen in Section 3.2.

The efficiency speaks of the probability that if a single photon is requested, then what is the total probability that the quantum dot is excited and emits a photon into a mode that is later collected and used. The wish is that the photon generation is deterministic i.e. one request leads to one photon. Here some of the biggest losses often do not come from the quantum dot emission but rather the optical transport of photons (Uppu et al. [8]). Coupling light from a quantum dot into an optical mode and collecting it with a fiber or though free space optics, reduce the overall efficiency at every interface. One way of combating this is of cause the "simple" matter of optimizing optical set-ups to the brim. Others try integrating optics like phase shifters and beam splitters into the wafer of the quantum dot to reduce coupling losses (Papon et al. [27]). Such that an experiment like the HBT could be performed on chip. But on chip propagation also suffers from loss, so long on-chip experiments will be less and less efficient with increased propagation lengths.

Lastly the consistency of the source or indestinguishability of the photons produced. The indestinguishability of photons will not be measured in this thesis but i want to touch on it quickly for completeness. From *Introductory Quantum Optics* (Gerry and Knight [20]), we learn of the beam splitter relations of two indistinguishable photons incident from different input paths of a beam splitter: The two indistinguishable photons will always emerge in the same output mode. If the two photons are distinguishable they will choose output paths randomly. An experiment measuring the indestinguishability was realized by Hong, Ou and Mandel (Hong, Ou, and Mandel [28]). By controlling the independent polarization of the two photons incoming on the beam splitter, they can be fully co,- and cross-polarized. In this way both the distinguishable and indistinguishable case. The comparison of these cases give the indestinguishability:

$$V = \frac{A_{\perp} - A_{\parallel}}{A_{\perp}} \tag{5}$$

Where the HOM visibility V is determined by the by the total coincidences A of photons when polarization is in either co,- $\parallel$ or cross-polarization $\perp$. A great single photon source has near unity visibility also multiple photons apart (Uppu et al. [8]).

1.2 NANOPHOTONIC STRUCTURES FOR EFFICIENT COLLECTION

Bulk quantum dots emit photons in all directions allowed by its dipoles, into the semiconducting wafer and out of the plane making high collection efficiency a challenging task. Nanophotonic structures is a solution to the problem. By etching the bulk surrounding the quantum dot into a waveguide where only one (or few) optical modes exist, the probability of the quantum dot emitting into the waveguide can be en-

Figure 6: Left: A freely suspended NBWG featuring two shallow etched gratings for out of plane coupling. SEM image by Freja Pedersen. Right: Dispersion relation of NBWG of GaAs. Only the first Brillouin zone is displayed. The yellow area is the light cone, modes therein are not confined through total internal reflection and are scattered out of the NBWG. The graph also displays higher order modes (green and blue), these are not present in NBWGs with a smaller width "w". Figure adapted from MSc. thesis of Kasper Prindal-Nielsen.

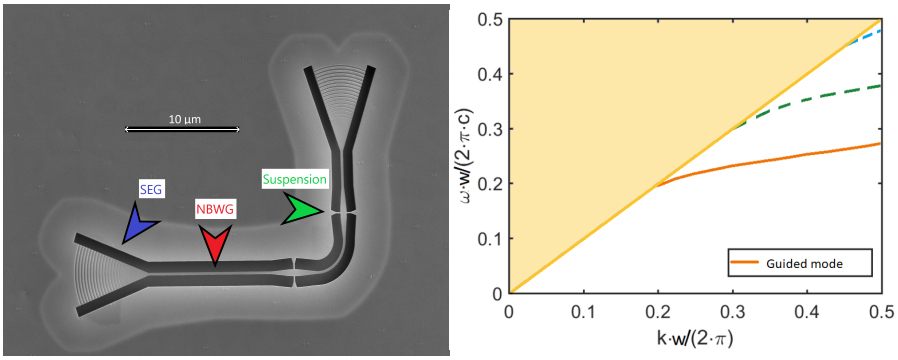

gineered to near unity efficiency (Lodahl, Mahmoodian, and Stobbe [7]).

Etching the wafer around a quantum dot decreases the local density of states. As we saw in the previous section this means that the quantum dot will experience Purcell enhancement. This makes interfacing quantum dots and nanophotonics an ideal match for single photon operation.

1.2.1 *Nanobeam waveguide and shallow etched gratings*

The NanoBeam WaveGuide (NBWG), consists of simply etching a freely suspended beam in the wafer. This creates a single high-low group index interface, causing total internal reflection. The nanobeams width can be made slim enough to only allows single modes of propagation (see Figure 6). Simply making light emit into a nanobeam is not enough, the light also needs to be couple out of the plane for collection. For this the use of Shallow Etched Grating (SEG) (Zhou et al. [29]) is optimal. The SEG diffracts light out of the plane for free space collection from the nanobeam. The diffraction can be engineered to fit the frequencies supported by the NBWG and are optimized to reduce reflections back into the NBWG however at low frequencies they become less effective and start reflecting. SEGs have an overall efficiency of ~75%.

1.2.1.1 *Cavity effects in photonic structures*

The Shallow etched gratings can have a significant reflection coefficient at the low wavelength part of its transmission. If these reflections are significant the SEGs will form an optical cavity. Traditionally opti-

Figure 7: Left: Illustration of the cavity between shallow etched gratings in the reflective case. Right: The transmission of an optical cavity. The distance between two peaks is called the free spectral range.

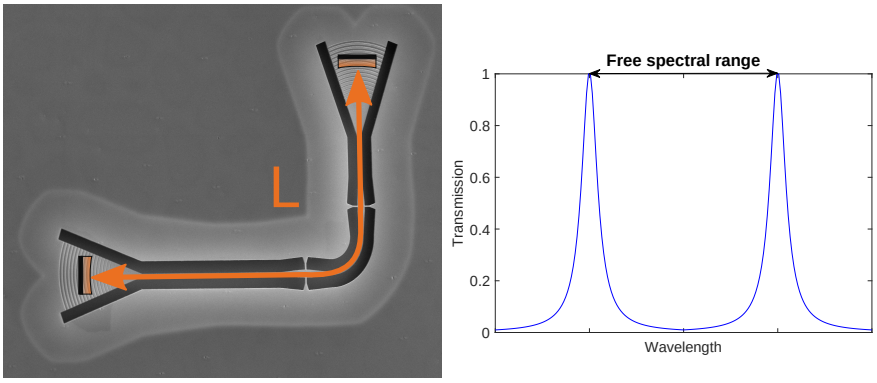

cal cavities consist of two mirrors separated a distance L where light coupled into the cavity is reflected back and forth between the two mirrors, creating a standing wave with nodes at the mirror interface. Interference between the light and itself discriminates wavelengths that do not fulfil $m_i\lambda = L$ where m_i is an integer. The higher the reflectivity of the mirror the higher is the electric fields interaction with itself and thereby the discrimination, this is called the Fabry-Pérot effect. The wavelength space between two modes fulfilling $m_i\lambda = L$ is called the Free-Spectral-Range (FSR), and is dependent on the wavelength λ, the length of the cavity L and the group index of refraction n_g:

$$FSR = \frac{\lambda^2}{2n_g L} \tag{6}$$

Usually this can be avoided by working in wavelengths where the reflectivity of the SEGs is low, but this is not always possible.

1.2.2 *Photonic Crystal Waveguides*

Photonic crystals consist of a crystal structure of periodic changes in refractive index to promote optical Bragg scattering (Lodahl, Mahmoodian, and Stobbe [7]). For the work in this thesis, it is done by introducing periodic holes in a triangular lattice with constant "a" and hole radius "r" of air ($n_{1,air} \approx 1$) into bulk semiconductor material (e.g. $n_{2,GaAs} \approx 3.5$). The Bragg scattering can be engineered to disallows certain wavelengths of light from propagating in the material through destructive interference, opening up a photonic bandgap. In the photonic bandgap the density of optical states is zero for given frequencies. By creating a line defect in the crystal, propagation of a single Bloch mode(s) can be introduced into the photonic bandgap see Figure 8. This constitutes the Photonic Crystal Waveguide (PCW).

Figure 8: Left: Illustration of a photonic crystal waveguide, where "a" is the lattice constant and r is the radius of air holes. A line defect runs in the middle of the waveguide. Right: Simulated dispersion relation of photonic crystal waveguide. The yellow triangle to the top left is the light cone where light scatters out of plane. The purple area in the top and bottom are bulk modes, surrounding the white bandgap in the centre. The two orange lines are modes allowed in the bandgap. (Both figures adapted from Freja Pedersen, simulation is by Nils Hauff)

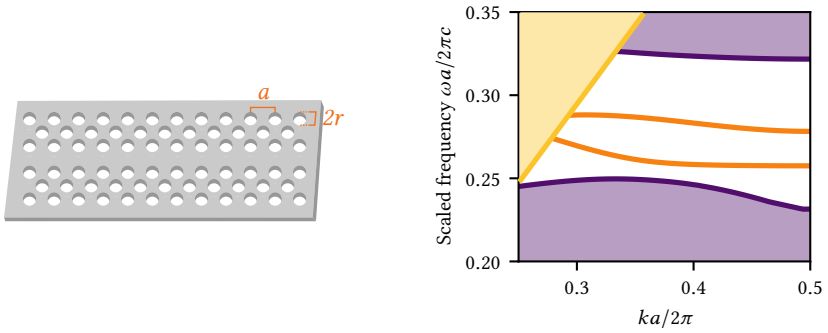

The group velocity of a mode can be found given by the non-linear dispersion relation:

$$v_g = \left.\frac{d\omega(k)}{dk}\right|_{k=k_0}, \tag{7}$$

where $\omega(k)$ is the frequency given a wave vector k. The group velocity is the speed of a wave packet of light moving through a medium. Looking at the slope of the dispersion relation in Figure 8, it is quite flat at the band edge. This means that the group velocity is significantly slower in the guided mode than it would be in e.g. vacuum. This phenomena is called slow light. Instead of talking about speeds of light it is more convenient to convert the group velocity to the group index:

$$n_g = \frac{c}{v_g} = c\left(\left.\frac{d\omega(k)}{dk}\right|_{k=k_0}\right)^{-1} \tag{8}$$

In regions of slow light, near the edge of the photonic bandgap, the group index can increase dramatically to the range of hundreds of times that of vacuum. Increasing the group index increases which in turn increases the effective density of optical states into the mode. A quantum dot which emits into a high n_g frequency region will therefore experience Purcell enhanced emission. The PCW is an amazing device for archiving high light-matter interaction.

This can be circumvented by only creating one SEG and closing the crystal in one end. With this design the possibility of in-plane excitation of the quantum dot is sacrificed for higher efficiency, we will not study this single sided device in this thesis but it is one solution.

Figure 9: Left: Illustration of GPW lattice. The lattice is offset by a/2, which breaks the waveguide symmetry, making the guided mode circular polarized. Illustration adapted from (Mahmoodian et al. [17]). Center: Calculated electric field of quantum dot emission into the guided mode for right(blue),- and left(red) handed circular polarization. Figure is adapted form: (Söllner et al. [30]). Right: Simulated band structure of highly directional GPW as shown in the centre figure. While not shown here, the GPW can also feature a photonic band gap similar to the PCW. Figure adapted from Pedersen [23]. Simulation is by Nils Hauff.

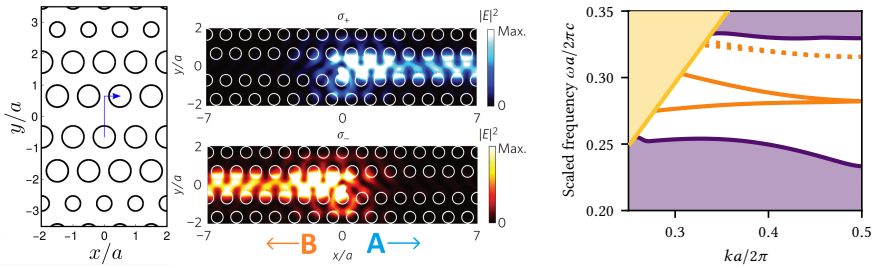

The vast majority of the PCW bandgap mode couples to linear polarization, meaning that there is a very low chance that an emitter would be placed where it could couple (i.e. emit) into a circular polarization basis (e.g. low FSS Biexciton cascade). This comes from the periodicity of the crystal which ensures that the Bloch mode $\mathbf{E}_{\mathbf{k}}(\mathbf{r})$ with wave vector k in the waveguide is translational symmetric (Mahmoodian et al. [17]):

$$\mathbf{E}^{*}_{\pi/a}(\mathbf{r}) = \mathbf{E}_{-\pi/a}(\mathbf{r}) = \mathbf{E}_{\pi/a}(\mathbf{r}) \tag{9}$$

This is manifest due to the translational symmetry of the waveguide, the electric field must be its own complex conjugate for any π/a translation. This excludes circular polarized light from the PCW. The model above is a quite simple one, and in reality PCW do have few areas where circular polarization is allowed (close to the edge of the waveguide).

1.2.3 *Glide plane waveguide*

The Glide Plane Waveguide (GPW) features a photonic crystal lattice where on side of the middle defect is offset by $a/2$ (see Figure 9). This breaks the translational symmetry of the waveguide. And Equation 9, is no longer valid. The Bloch mode now needs to change phase of $\pm i$ every $k = \pi/a$ lattice. This makes circular polarized light the solution to the polarization of the guided mode. To satisfy time-reversal symmetry, two counter propagating modes must exist. This makes the left and right handed polarization propagate in different directions.

The GPW is useful for converting the polarization entanglement of a biexciton cascade to path entanglement. A quantum dot situated in a GPW can emit into the circular polarization basis, and its photons

will chirally coupled to emitted along either the positive(A) or negative(B) x-direction (Figure 9). This makes the 2-photon state of the biexciton cascade from Equation 2 become:

$$|\psi^+\rangle = \frac{1}{\sqrt{2}}\left(|R_X L_X\rangle + |L_X R_X\rangle\right) \Rightarrow |\psi^+\rangle = \frac{1}{\sqrt{2}}\left(|A_X B_X\rangle + |B_X A_X\rangle\right) \tag{10}$$

Path entanglement in free space is usually quite finicky as it requires precise control of the two paths length. On integrated photonics this is not a problem since the path lengths can be very precisely engineered from fabrication.

1.3 TOPOLOGICAL PHOTONICS

Topology is a recent field to make its way into the world of photonics. With topological phase protection promising: Increased system stability in the face of defects (Miguel A. Bandres [31]), scattering free edge state with 120° bends (Mikhail I. Shalaev and Litchinitser [32]), unidirectional, zero backscattering light transport (Ling Lu and Soljačić [11]). All of these are incredible features, however as the field is still new, the promises are still being tested, quantified and explored.

In this thesis i will not go into full detail of topological transport, with the field still in development I will focus on the basics, with a focus on giving the understanding needed to analyse the measurements I have done on topological photonic devices. I will also split this theory section in two, here focusing on general topology and its fusion with photonics and in Chapter 5 the focus will be on the actual studied devices.

Topology is the field of mathematics studying spacial geometry and deformation thereof. The popular example of what topology studies is "whether or not a geometry can be deformed into another". A coffee mug and a doughnut have the same topological phase, since without tearing or gluing they could deform continuously into the other. In 2D photonics this phase is characterized by the Berry Phase, and can be calculated as the integral of the Bloch mode phase along a unit cell. Integrating the Berry-phase around the Brillouin Zone results in a so called Chern number. The Chern number is the indication of what topological phase the unit cell is and takes the form of full or half integers depending on what kind of topology is produced(Ling Lu and Soljačić [11]).

Let us look at a modified lattice element similar to the structures we have studied so far (see Figure 10). This modified version creates a hexagon pattern when the cells are placed in a lattice configuration. Since the crystal is periodic this creates what is called a honeycomb pattern, similar to what can be found in graphene. The band diagram of this type of crystal mimics that of graphene and produces what is

Figure 10: Trivial photonic honeycomb lattice. The honeycomb lattice produces dispersion similar to band diagrams in graphene. In k-space the K and K′ points are symmetric which leads to degeneracy. The integral of the Berry phase around the Brillouin zone results in a Chern number of 0. The banddiagram displays the bulk modes in orange that are connected i.e. degenerate. Photons here can move in both positive and negative direction in he lattice.

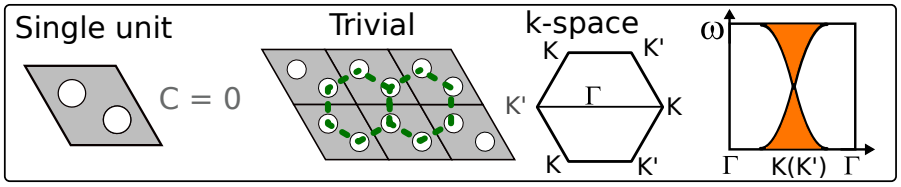

Figure 11: Breaking the lattice element symmetry lifts the degeneracy at K and K′ and opens a topological bandgap. The new unit cell features a Chern number of ±½ depending on the orientation. A phase vortex in the magnetic H_z field is created in the honeycomb and, its rotational direction produces pseudo spin.

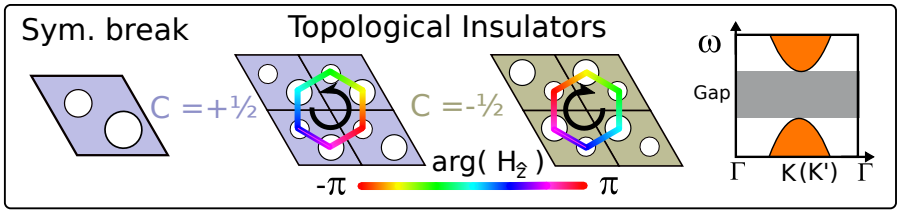

called Dirac cones in k-space. As can be seen of the illustrated band diagram of the photonic structure the honeycomb lattice does not feature a photonic band gap. The honeycomb lattice is C6 symmetric, meaning it can be rotated 60deg, and mirrored along any side or edge without changing the structure. This leads to the points K and K′ in k-space to be symmetric from which a degeneracy of the upper and lower band follows (Zee [33]). Calculating the Chern number of such a unit cell produces net zero and is called topologically trivial. All the structures we have studied so far have been k-space symmetric (even the GPW) from which it follows they have all been topologically trivial.

To create a topological band gap the degeneracy needs to be lifted. One could simply apply a magnetic field, this would break the time reversal symmetry, opening a band gap (Xiaodong Xu and Heinz [34]). In our case we wish to interface with quantum dots that are sensitive to magnetic fields, so this is not an option. We wish to introduce something similar to the Hall effect.

Another method is to break the C6 symmetry (see Figure 11). If we change one of the holes in the single lattice (make it bigger/smaller or reshape it entirely), we break the symmetry. The system becomes 3-fold symmetric, meaning that if we rotate 60° or mirror the structure along a centre line we have inverted the structure i.e. K (K′) → K′ (K). Breaking symmetry lifts degeneracy and splits the degenerate bulk modes and creates a gap encased at K and K′. This also creates a

Figure 12: Interfacing topological insulators of different topological phase i.e. Chern numbers allows a mode to travel along the interface. The edge modes have either positive or negative group velocity, but due to topological protection the intersection is non-degenerate, unlike the trivial case.

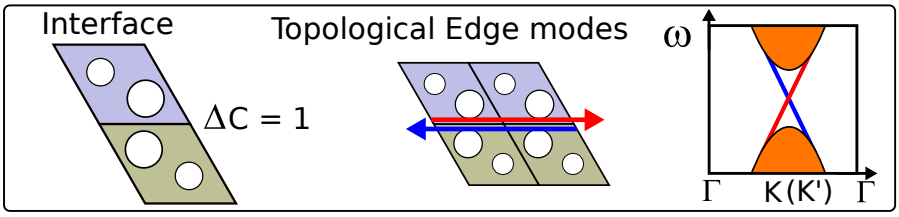

phase vortex of the Bloch modes magnetic field H_z in the honeycomb (Xin-Tao He and Dong [35]). The rotational direction can be thought of as a spin ½ pseudo-spin. This gives the integral of the Berry-phase non-zero values and the Chern number of this type of unit cell comes out to C = ½ making it topologically non-trivial. This combined with its bandgap have dubbed it a topological insulator. Now if we are to invert the unit cell i.e. big holes become small and vice versa, the now rotated cell will have different inverted symmetry. That means K and K' effectively switch places. This also flips the pseudo spin. Calculating the Chern number of this inverted cell comes out to C = -½ (see Figure 11). Being able to create bandgaps with topology is cool, but in and of itself it is not much more useful than a photonic crystal.

It gets interesting when placing two insulators of different topological phase together. This creates what is called an edge mode at the interface (Ma and Shvets [36]) (see Figure 12). The edge mode is a product of the topological phase discretely changing at the insulators interface. This mode is distinct from the one we have seen in the PCW, while the PCW mode travels in an intentional "defect" of the photonic crystal lattice, the edge mode travels at the interface edge effectively in the bulk of the crystal. This area is very confined making the physical size of the mode span multiple µm into the topological crystal. Reading the group velocity it can be seen that the two modes created propagate in either positive or negative direction, these modes are topologically locked, meaning that switching between them is similar to transforming a spoon into a doughnut without making a hole - it cannot be done. This is from where the idea of the backscattering protection arises.

2

EXPERIMENTAL SET-UPS AND METHODS

2.1 QUANTUM DOT EXCITATION SCHEMES IN PHOTONIC STRUCTURES

Spectroscopy of quantum dots in photonic structures is a big bulk of the experimental work performed in this thesis. There is a multitude of ways to excite quantum dots and they all serve different purposes, and have distinct advantages. It is important to understand how these methods work and what results they produce. The quantum dots studied in this thesis are all situated inside one or another type of photonic structure. Before looking at the individual methods of excitation let us first take a general look at quantum dot excitation in a photonic waveguide structure (see Figure 13).

Figure 13: Excitation of a quantum dot situated in a photonic crystal waveguide. The quantum dot (yellow) is excited with laser action (green). The quantum dot can emit in either direction of the waveguide (orange). Emission is directed out of plane by the shallow etched gratings, depending on their rotation the collected light will either be linear x,- (blue) or y-polarized (red). Figure adapted from Pedersen [23].

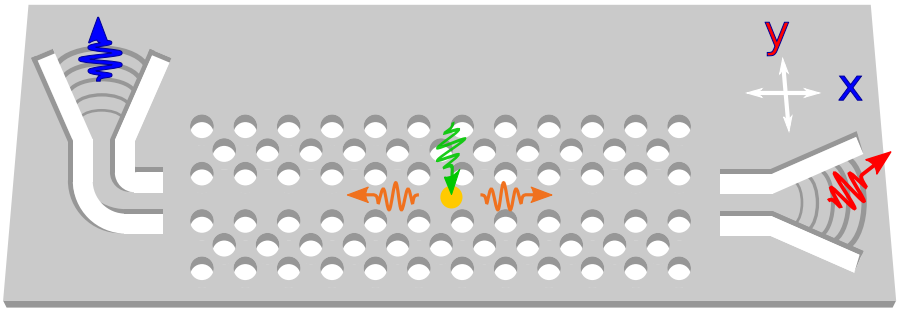

A quantum dot can be excited with laser action perpendicular to the waveguide plane. Both the x,- and y-directional dipoles of the quantum dot can be excited this way (although one often couples weaker than the other), and high energy excitation can promote exciton diffusion into the quantum dot (see more in Chapter 3). Depending on the exact location of the quantum dot in regards to the intra-electric field i.e. Bloch mode of the photonic crystal waveguide (PCW) one of the dipoles might have a stronger coupling to the waveguide, making emission from said dipole more prominent. Once the quantum dot is excited it can emit into the two waveguide directions. The light is then incident on a shallow etched grating (SEG) (either direction). The SEGs project the polarization into the linear basis, and angles the propagation direction upward(z) by 82°. The polarization of the light out of plane is therefore dependent on the propagation

Figure 14: An exemplary semiconductor quantum dot and several of excitation/decay schematics. From left to right are the excitations depicted: Aboveband,- Wetting Layer,- Quasi resonant,- p-shell,- and Resonant Excitation. The majority of excited states non-radiatively decays to the s-shell where electronic band gap is the smallest before recombination.

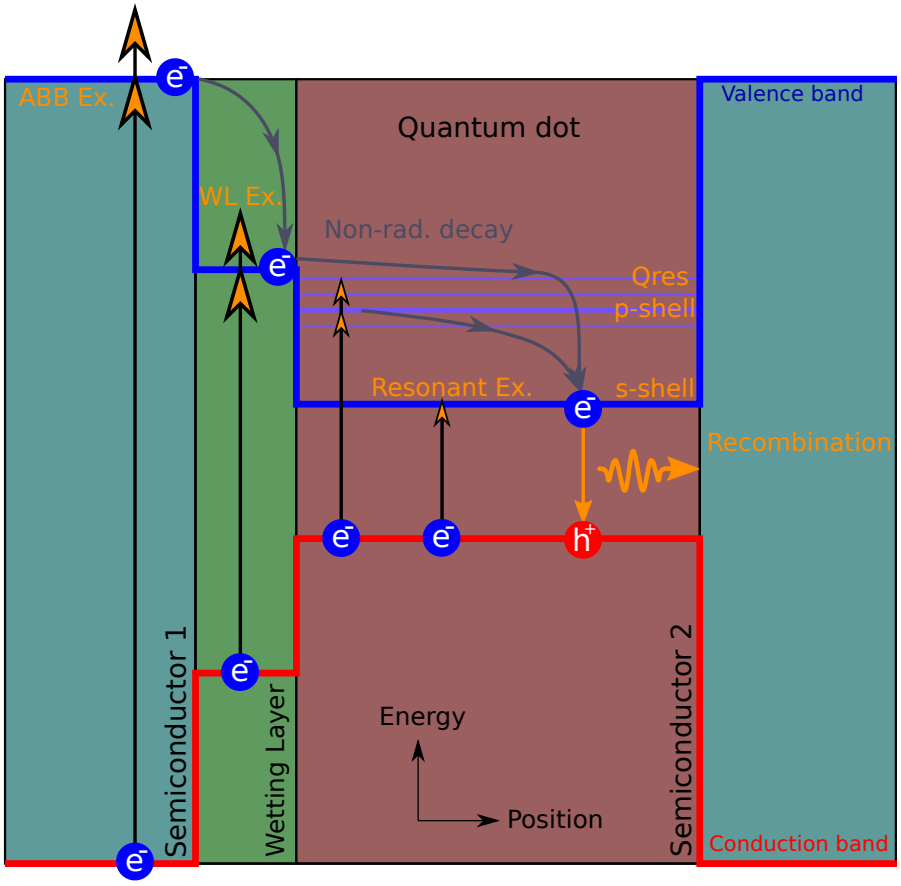

direction of the in-plane light. The photons from the two SEGs depicted in Figure 13 are perpendicularly polarized. They can also be build with the same coupling polarization, but preventing cross talk between the waveguides is often more desirable.

Let us now jump into the specifics of exciting the quantum dot.

2.1.1 *Aboveband Excitation*

Aboveband(ABB) excitation relies on a high energy laser incident on a semiconductor. Providing high energy to bulk semiconductor material (semiconductor 1 in Figure 14) allows electrons to excite from the valence band to, and importantly, *above* the conduction band leaving a quasi-particle hole behind. The combination of electron and hole form an excited quasi-particle called an exciton. The exciton diffuses towards lower potential for recombination. If the exciton has been provided enough energy it can diffuse into a quantum dot where it non-radiatively decays to the first excited state (s-shell) and then re-

combines and emits a photon. Less likely, it can also recombine from higher order states emitting at a lower wavelength photon, which is probably most of the less intensive emission lines in the exemplary ABB spectrum in Figure 14. This method requires very low laser precision, since the diffusive distance of an excitons in conventional semiconductor can be up to ~14 µm (M. Niemeyer and Lackner [37]). As long as carriers with enough energy to diffuse into the quantum dot are created this method produces quantum dot emission. The efficiency is not excellent since the excitons also scatter elsewhere and excite other quantum dots if they are within diffusion range, but it does circumvent having to deal with dipoles. An example of an ABB spectrum is shown in Figure 15. Here is also depicted one of the advantages of the ABB excitation. Due to its wide range it is possible to find multiple quantum dots in the same spectrum, which is excellent when searching for quantum dots. However, if only analysis of a single quantum dot is required, it can sometimes be tricky to do with ABB since the carriers will diffuse to all nearby quantum dots in range and produce noisy spectra, together with decay from higher states. This can be counteracted by having a lower density sample, or turning down the laser power significantly or, switching to a different method. ABB excitation in this thesis will be used for finding quantum dots and roughly aligning the laser through optimizing emission.

Figure 15: Example of an aboveband excitation spectrum with a 780 nm laser onto an InAs quantum dot with 3.3 µW of power. The sample is medium-low density so only few quantum dots show. A slightly power broadened quantum dot situated at 924 nm, and another less so at 930 nm (indicating it sits further away). The rest of the spectrum is messy and hard to analyze.

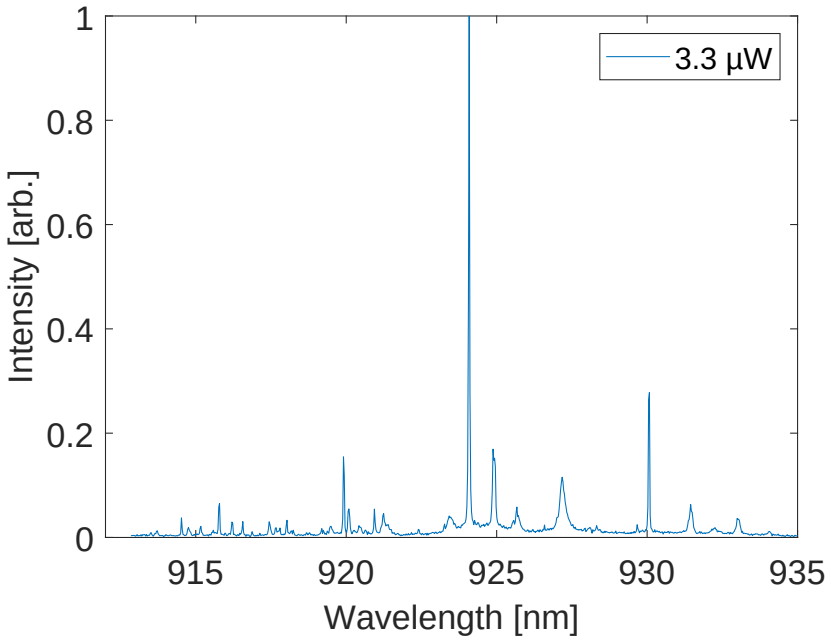

2.1.2 *Wetting Layer Excitation*

The wetting layer (WL) is an alloy between the quantum dot and wafers semiconducting material, and is therefore situated in proximity to the quantum dot. Therefore excitation of the WL requires a somewhat more accurate laser aim. Here excitons are created in the same manner as with the ABB method, but it requires less energy since the bandgap is smaller (see Figure 14). Due to requiring less energy, WL excitation also excites fewer random transitions and generally produces a cleaner spectrum than ABB. (It is not used in this thesis, but i wanted to include it for completion).

2.1.3 *Quasi-resonant / p-shell Excitation*

Quasi-resonant (Qres) excitation utilizes the higher order quantized energy levels of the quantum dot. The p-shell is one of those quasi-resonant states in analogy to how atom states are named in atom physics. That carry the Unlike ABB and WL excitation where creating carriers is all that matters, here consideration for the dipole interaction between the quantum dot and the electric field needs to be taken into account, as seen through the light-matter interaction Hamiltonian $\mathbf{H_{int}} = -\hat{\mathbf{d}} \cdot \mathbf{E}$ (Gerry and Knight [20]). Optimal excitation of the quantum dot now requires the electric laser field $\mathbf{E}$ to have its polarization aligned with the quantum dot dipole(s) $\hat{\mathbf{d}}$. A quantum dot situated in a photonic waveguide experiences an increased optical density of states it can emit into due to Purcell enhancement. Due to Fermi's golden rule for spontaneous emission, this means that the coupling strength to other modes is decreased, meaning that exciting a quantum dot through dipole interaction is less effective when the quantum dot is in a photonic waveguide. Therefore Qres / p-shell (and resonant fluorescence) is more difficult on quantum dots in photonic structures compared to ABB/WL that only depend on exciton diffusion. The quasi-resonant levels usually decays to the s-shell in a few picoseconds [7] much faster than the s-shell decay. This makes it a good method of exciting the quantum dot. Exciting though quasi-resonant states means that emission possible from this excitation scheme in general will have less energy than the WL excitation, but still there is always a chance that the exciton recombines directly from the p-shell / Qres layer.

2.1.4 *Resonant Excitation / Fluorescence*

Exciting resonantly with the quantum dot requires the highest amount of laser accuracy, while also requiring high control of the laser frequency,- and polarization all while the excitation couples to a dipole that is weakened through Purcell effect. It is difficult to perform. When

performing resonant spectroscopy a problem arises due to excitation laser and the emission have the same frequency making it very difficult to distinguish. When performing resonant spectroscopy it is therefore often advantageous to excite one dipole of the quantum dot and collect the other e.g. excite with horizontal polarization and use a linear polarizer in the collection to only collect vertically polarized light (Schöll et al. [15]). This method is not perfect, and fully suppressing the laser while still getting quantum dot signal is a finicky task. This is most apparent on the difference of second order photon correlations, where resonant excitation is by far the more difficult method to produce a great (low) $g^{(2)}(0)$ compared to quasi resonant excitation (or two-photon excitation), due to laser light leakage (Schöll et al. [15]).

2.1.5 *Resonant Transmission*

The excitation schemes we have seen so far have been exciting from outside the plane of the quantum dot. Resonant transmission happens from within the plane. Utilizing a SEG in tandem with a photonic structure allows coherent interaction with the quantum dot (see Figure 16).

Figure 16: Illustration of resonant transmission. Three different coloured photons are coupled into the shallow etched grating and guided to the quantum dot. The photon in yellow is resonant with the quantum dot, and is therefore reflected. The two other photons do not interact with the quantum dot and continue to be collected from the second shallow etched grating. At "yellow frequency" one would expect a dip in transmission with linewidth similar to the quantum dot. Figure adapted from (Pedersen [23]).

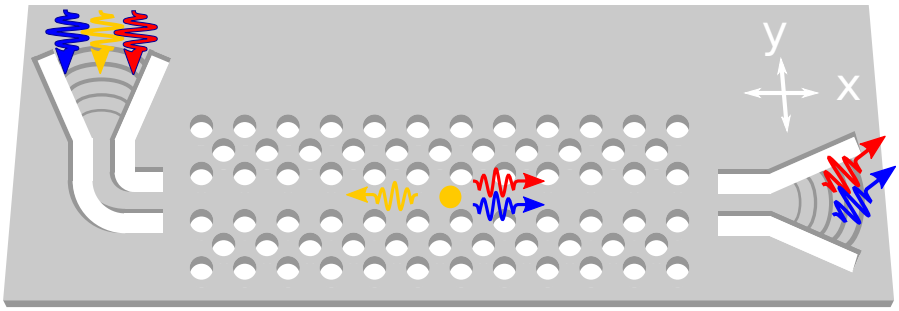

This makes the quantum dot reflect light resonant with the quantum dot due to interference. This means that when looking for a quantum dot in Resonant Transmission (RT) we look for dips in transmission instead of peaks. When working within the plane of the quantum dots the SEGs play a large role in the transmission spectrum. The SEGs have a limited optimal wavelength range and toward long wavelengths it starts being reflective. If this reflection is significant it will produce cavity effects in the waveguide with the SEGs as the cavity mirrors (see more in Chapter 5). This convolves the quantum

Figure 17: Main optics set-up (simplified). Green area: Starting from the left, lasers can be connected to a Diffraction limited path and a shallow etched grating (SEG) optimized path. The diffraction limited path is used when exciting quantum dots perpendicular the sample plane, while the SEG path matches the mode of the SEGs. Beam polarization and power is controlled with respectively λ plates and a photo diode connected to a PID-circuit with the laser. The input can be combined with an aboveband laser if so chosen. Yellow area: Light from the green area is incident on an interchangeable beam splitter, 50/50 for transmission and 90/10 for quantum dots. Incident light in red/green interacts with the sample through an objective. The sample sits in a vacuum and is cooled by copper block cooled by a suspended cold finger. The sample can be illuminated with white light(blue). Red area: The collection path is polarization controlled to optimize collection from SEGs. White light can be interjected here to go to the sample. Collection can happen from two arms, but mainly Out1 is used.

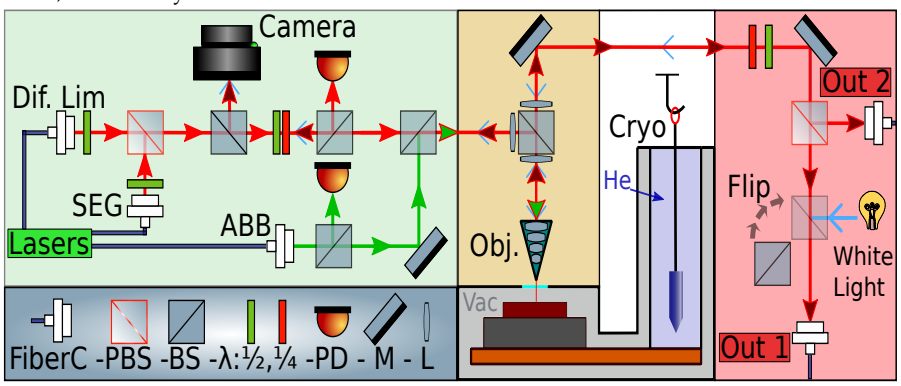

dot emission with the cavity modes creating a "Fano lineshape" (Fano [38]) (see more in Chapter 4).

2.2 OPTICAL SET-UPS FOR SPECTROSCOPY

The main optical set-up can be found in Figure 17. The set-up consists of two main fiber input ports, a diffraction limited one, which creates as small a laser dot on the sample as diffraction allows (Optimized to 790 nm). This input path is optimal for exciting the quantum dot out of plane for Res/Qres excitation. Quantum dots are tiny so to get the theoretical optimal coupling to them the laser dot would have to be very small - going to the diffraction limit is as small as we can go without going through complicated loops. The second input path is optimized to match the modes of the SEGs. The two input ports are operated one at a time. Utilizing the λ½-plates after the fiber couplers the two laser paths are combined on a Polarized Beam Splitter (PBS) at full power but cross polarization between the two paths. Both for coupling into the SEGs, and to excite the quantum dots dipoles for RF/QRes excitation polarization control is important and it is controlled with the λ-plates. A camera is combined into the optics path here which provides visual feedback of the sample and laser position while conducting spectroscopy. Next a Beam Splitter (BS) splits the light onto a photo diode connected to a PID-control loop with the

laser(not visualized). The PID loop allows intricate control of the laser power, and applying it late in the optics set-up is desirable for a more correct reading of the power. Next a BS combines the first and the second with a third input path. This path is meant for an ABB laser. ABB excitation does not require polarization control and is therefore optimal to combine the beams at this stage. At times the BS has also been replaced by a diachronic mirror, allowing less wasted input power. The combined red and green laser paths are visualized with a red arrow filled with green.

The laser beam makes its way to the focusing unit. Here a configuration of 4 lenses (3 + the objective) ensures the focus specifications as given by the input paths. Visible light (in blue, for the camera) is also combined here. The combined input beam is now focused on the sample space. The sample space is situated inside an Advanced Research Systems (ARS) Cryostat. A sample sits in a vacuum "box" secured to the same optical table as the optics. The cryostat cools the sample by cooling a cold finger suspended above a copper block. Cooling action on a cold finger can cause major vibrations of said cold finger. If these vibrations were to be connected to the sample, precise laser positioning would not be possible, and major intensity fluctuations would occur. Instead of letting the cold finger rest on the copper block, ambient helium-4 gas is utilized for thermal exchange between the two. This allows the sample to be cooled to a temperature of ~ 6 Kelvin with minimal vibrations. Prolonged cryo operation can lead to water build up in the helium chamber (1-3 weeks), this freezes on top of the copper block decreasing the thermal contact between the cold finger and the copper block. This creates a steady increase in temperature with time. The accumulated water can reach a critical amount where the copper block and cold finger are connected with ice. This creates a rigid bridge for the cold finger vibrations to travel to the sample. Once the cryo reaches this point a thermal cycle is required to empty out the water. Operation, monitoring and maintenance of the cryostat has been a large part of the day to day work on the set-up, and getting it to reach and operate at low temperatures has been a long term struggle.

To allow for translation of the laser position on the sample and not just angling adjustments, the entire optical (green, yellow and red areas) set-up is mounted on a motorized horizontal plane translational stage. The stage sits on the same table as the sample vacuum box, but the sample box is not on the translational stage. This means that we can move the entire optical set-up relative to the sample. Normally it is easier to move the sample with a XYZ piezo stack - but the ARS has limited available space and installing a piezo stack would further increase an already high heat-load.

After the input beam has interacted with the sample in a desired way it is emitted out of plane from a SEG which creates a $\sim 8°$ an-

gle normal to the plane. Switching between the two SEGs therefore requires realignment of the collection. The emitted light (in red with a dark red arrow) is send through two λ plates to optimize the collection from SEG, and allows polarization control for biexciton collection. The light is then passed through a PBS which splits the light to two different output ports. The two different output ports can be focused upon two different SEGs and collect two different polarizations at the same time.

2.2.1 *Secondary set-ups*

Some secondary set-ups are used for special measurements. I will introduce them here.

Some of the detectors used are photon detectors, meaning they unlike spectrometers do not see colour. That means that filtering of the light previous to the detector is crucial. For this means a grating filter is employed. The filter allows high resolution filtering by scattering light off a diffraction grating, and collecting the first order reflection (i.e. not direct) Figure 18. The light scatters at different angles with wavelength dependence similar to white light through a prism. A telescope is used before the grating to ensure the biggest area of interaction with the grating. The light is then coupled into a fiber, which in effect acts like a narrow slit for which we can select the wavelength we desire. It is aligned by setting a narrow linewidth laser to the same wavelength as quantum dot emission and optimizing the collection. The diffraction grating used has a density of 1200 lines/mm with at beam diameter of ~4cm giving a resolution of 4.5 GHz (or 0.02 nm).

Next is a HBT set-up for doing g^2 measurements. Photons are coupled into the HBT set-up (usually after having been around the grating filter) and is split on a BS. If only single photons arrive at the set-up the two photo detectors should never click at the same time i.e. $g^2(0) = 0$. But from e.g. a coherent laser field two photons always arrive together creating correlations of $g^2(0) = 1$. When measuring photons there is some timing jitter in when exactly the photon is detected. That is there is a layer of uncertainty in time given to the measurement by the detector used. The amount of jitter is dependent on the instrument response function of the detector (and optical system).

For measuring the lifetime/decay rate of a quantum dot it is key to have a pulsed laser with a trigger. The pulsed laser produces a trigger signal which is sent to a timer with a delay matching that of the time it takes a photon to travel through the set-up and be detected. This way, the exact round trip time of the photon can be known. Hopefully in the set-up the only significant difference between two photons arrival time should be given by the randomness of spontaneous decay of the quantum dot. As with the g^2 lifetime measurements are also prone to

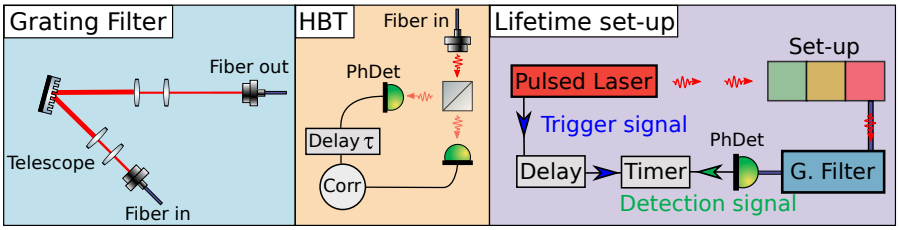

Figure 18: Secondary optical set-ups. Left: The grating filter scatters light continuously dependent on wavelength. By angeling the grating a specific wavelength can be coupled to the fiber. Centre: HBT set-up for g^2 measurements. Photons are incident on a beam splitter. If only a single photon enters only a single photo detector will click. Right: Set-up used for lifetime measurements. A pulsed laser sends a trigger signal upon emission. The trigger is delayed such that it arrives shortly before photon detection.

the timing jitter of detectors, which artificially changes the quantum dot decay rate unless taken into account.

2.3 EXCITATION AND COLLECTION HARDWARE

A multitude of lasers and photon collectors have been utilized for the experiments for this thesis. I will here give a short introduction to them and how they are used.

2.3.1 *MIRA Laser*

The Coherent MIRA laser is the main laser utilized for our droplet dot experiments. It by far one of the most versatile lasers in our lab. It features wavelength tuning from 700-1000 nm, can switch between continuous wave (CW) and pulsed laser action. It has a sub quantum dot line-width, which can be utilized to scan out the different dipoles of a quantum dot. This laser is manually frequency tuned. Which means after finding a quantum dot in ABB, manual tuning using a knob was required to tune the laser to the desired frequency. This makes it a perfect tool for doing resonant, quasi resonant and biexciton,- excitations, where parking the laser at a given transition is in most cases enough. But having to manually tune a knob for a transmission scan of a waveguide is a painful endeavour.

2.3.2 *CTL*

The Toptica Photonics Continuously Tunable Laser (CTL) is a highly precise tunable laser in the range of 900-980 nm, featuring a sub quantum dot linewidth. This laser is outside the range of the droplet structures and could not be utilized for that experiment. The laser frequency is motor operated which allows programmed measurement sessions such as very fine resonant transmission scans, or full scans

of the transmission of a photonic structures. In addition to the tunable frequency the CTL is coupled to a high precision wavemeter, allowing programming to lock the laser frequency for improved stability.

2.3.3 *SuperK*

If the CTL is a precision knife the SuperK is a shotgun. The NKT Photonics Supercontinuum "SuperK" laser, produces a spectrum from 410-2400 nm, and is effectively a "white light laser source". This is an amazing tool when producing transmission measurements of waveguides. Combined with a spectrometer this can instantly produce the complete transmission spectrum of a photonic structure, only limited by the resolution of the spectrometer. Whenever the SuperK is used it is usually colour filtered. Whilst performing a transmission measurement of a structure that have transmission in the 910-960 nm range, it is undesirable for the rest of the laser spectrum to not to simultaneously induce ABB emission. The optical density is not constant they fluctuate on time scales $\sim$ 1 hour. Therefore doing measurements with the SuperK should not be long-term, and any long term measurements would require recalibration of the optical density faster than the fluctuations.

2.3.4 *Collection: Spectrometer, and Photo detectors*

The spectrometer used thorough the thesis uses a high resolution and a low resolution grating. The low resolution grating has a wide range, and is useful for transmission measurements where we wish to scan out a wide array of wavelengths. It has a resolution of $\Delta\lambda \approx 0.25$ nm (90 GHz). The high resolution grating has a lower range, and is useful for inspecting quantum dot emission $\Delta\lambda \approx 0.025$ nm (9 GHz). The spectrometer does not have the resolution to resolve the natural linewidth of the quantum dots at $\sim$1 GHz.

Where as the spectrometer can distinguish the colour of photons the Avalanche Photo Diode (APD) cannot, it simply "counts" photons. Therefore filtering must happen prior to the APD (e.g. the grating filter). These have been mainly used for scans involving the CTL. The same goes for the Superconducting-Nanowire Single-Photon Detector (SNSPD). It is very similar to the APD, except is has a faster instrument response function meaning it can resolve measurements with a lower timing jitter. These were mainly used for gathering g^2 and lifetime data, since it requires high timing resolution.

3

DROPLET DOTS IN NANOSTRUCTURES

This chapter will feature spectroscopy of a droplet quantum dot in a photonic crystal waveguide (PCW). A measure of the quantum dot's coupling to the photonic waveguide will be probed using power-series. Single photon properties will be characterized with measurements of the second order correlation under different excitation schemes and then the decay rate of both the exciton and biexciton will be compared. At the chapters close, design of the next generation sample in this series is presented using measurements from this generation.

Measurements in this chapter are performed on sample "AS-275" features non-gated (passive) GaAs in AlGaAs droplet quantum dots. This means that there is no electrical control of the quantum dots. This is one of our group's early experiments with producing nanostructures on a wafer containing droplet quantum dots. Therefore the nanostructures produced on the sample span out a multitude of parameters in hopes of coupling the quantum dots to nanostructures, meaning that only a few of the structures actually had parameters fitting the quantum dots. The quantum dots had been checked with aboveband excitation in bulk previously, and had shown generally broader linewidths than expected, likely attributed to spectral diffusion. All this made measurements difficult, and required a lot of trial and error. Unfortunately towards the end of measurements the sample was rendered non-functional in an accident.

3.1 DROPLET DOT ABOVEBAND EXCITATION IN PHOTONIC CRYSTAL WAVEGUIDE

A thorough search of quantum dots in photonic crystal waveguides with aboveband (ABB) excitation lead to finding a lot of non-optimal quantum dots due to: Wide emission lines, being located surrounded by unexplainable features, or just did not couple well to the photonic crystal, probably due to being situated inside the photonic crystal and not in the waveguide itself. Out of roughly 42 photonic crystals, 14 had decent transmission of quantum dot emission and in those PCW about 5 quantum dots had a narrow linewidth but poor brightness and 1 featured a narrow linewidth and decent brightness. The quantum dot featured in this chapter is the best found but not excellent.

Figure 19: SEM image of an arbitrary photonic crystal waveguide (PCW) from the AS-275 sample. It is similar to the one featured with a quantum dot in this chapter. The actual PCW has a lattice constant a = 206 nm and hole radii r = 46 nm. In green the approximate position of the quantum dot.

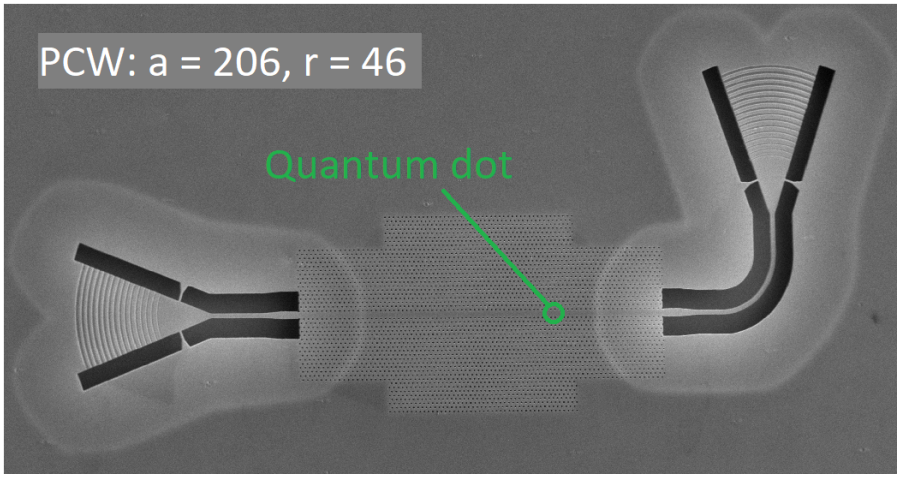

The quantum dot was located in the PCW by translating a 532 nm laser (a simple 532 nm laser pointer available for commercial use) from the ABB-path (see Figure 17 for a refresh) over the waveguide of the PCW, while collecting light from the SEGs to the high resolution spectrometer grating. Using this method the quantum dot was located near the centre of the waveguide (see Figure 19). A power series of the quantum dot using the ABB laser was performed to check if the quantum dot was tuning with power and saturates (see Figure 20).

This quantum dot had somewhat low brightness compared to InAs quantum dots. Here at 1 µW there is about 3500 counts. With similar settings (spectrometer included) on InAs tens of thousands of counts are common place. The power series is performed by increasing laser power and taking a spectrum. The resolution of the spectrometer is ~ 9 times higher than the quantum dot linewidth, this means that as long as the quantum dot does not experience significant AC-Stark shift, it remains within a single wavelength bin. Operation in the non-saturated domain is preferable, since the quantum dot has a linear response to photons. Increasing laser power increases the brightness of the dot, but it also broadens the emission linewidth (notice the bottom of the quantum dot emission features a wide blob). There is a trade-off between going to high power for better photon statistics and linewidth.

A reference g^2 measurement using ABB laser was performed for comparison with later measurements (see Figure 21). This data set will give insight into what is going on in later g^2 measurements, but no final conclusions about the dataset itself will be drawn.

Figure 20: Aboveband excitation of droplet quantum dot in photonic crystal waveguide - using 532 nm CW laser pointer. Left: Spectrum, featuring the quantum dot at 801 nm. Around 803 nm another quantum is visible with additional features. Right: Power series of the quantum dot at 801 nm. Fitting the data with: $C(P) = C_{max}(1 - exp(P/Psat))$ reveals a saturation power of 1.92 µW.

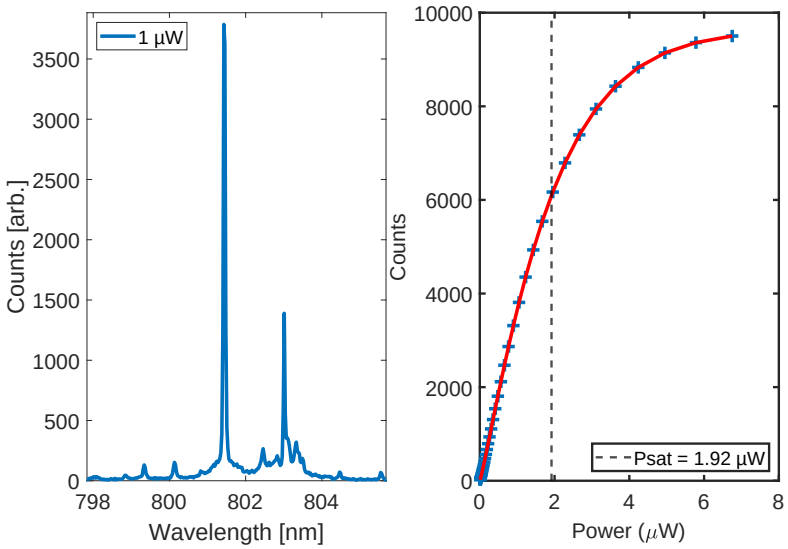

Figure 21: Quantum dot in photonic crystal waveguide g^2 with aboveband CW MIRA laser excitation. Left: The raw g^2 was impossible to discern this curve has been smoothed by 10 points for better visibility of $g^2(0)$. A rough estimate of the $g^2(0)$ comes out as $g^2(0) \approx 0.96$. There might be some single photons in there but it is mostly drowned in background noise form the ABB laser. Right: g^2 figure plotted in logarithmic x-axis with negative values projected onto the positive axis. Figure hints at blinking at ~ 0.5 µs time scale, but with low counts it is a very unreliable measure.

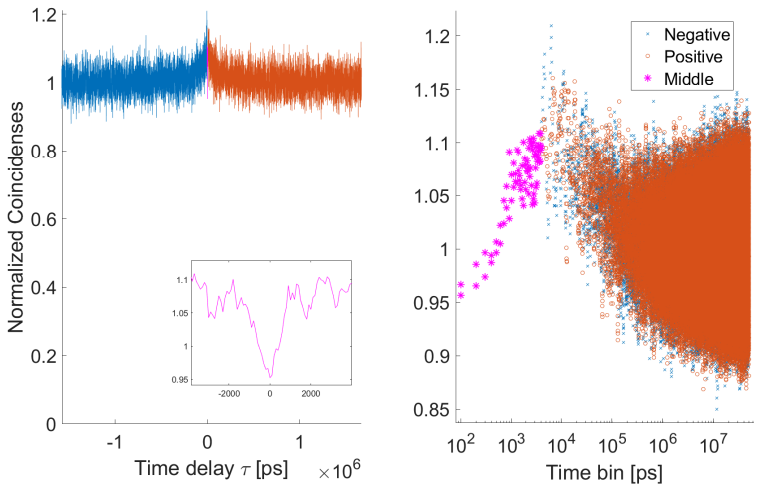

We can give a rough estimate of the g^2 at zero time delay:

$$g^2(0) \approx 1 - \frac{(Mean(CC) - CC(\tau = 0))}{Mean(CC)} \approx 1 - \frac{(142 - 137)}{142} = 0.96$$

Where CC are the Coincidence Counts. A $g^2(0)$ of 1.0 is representative of a coherent stream of photons, while a value slightly below is indicative of there being some single photons mixed in with the stream. This result is not very reliable, but it wasn't meant to be. The bunching surrounding $\tau = 0$, arise from the quantum dot blinking i.e. having a dark state exciton and then being excited by a bright exciton. After the first exciton decays the dark state can flip to a bright and then emit. This results in two photons being emitted in rapid succession, creating bunching close to $\tau = 0$. We can extract the blinking time scale by looking at how far the region of bunching extends. A rough estimate of when the blinking stops would be around 0.5 µs; this is where the slope from the bunching seems to stop (this is later done with a fit). Blinking at this time scale is limiting for deterministic operation of the quantum dot. The quantum dot is expected to have a decay rate of ~ 1 ns^{-1} where this blinking effect comes out in the µs regime. Continuous deterministic operation of this quantum dot would therefore be limited by the blinking, approximately 500 times slower than the quantum dot decay rate.

After these measurements an attempt at producing resonant fluorescence in the quantum dots were tried but unfortunately produced near-noise photon statistics. Therefore quantifying the quantum dot with CW p-shell excitation is the next step.

3.2 DROPLET DOT QUASI-RESONANT/P-SHELL EXCITATION IN PHOTONIC CRYSTAL WAVEGUIDE

Claiming p-shell excitation requires the knowledge of the wavelength difference between resonant and p-shell, otherwise the excitation might very well be quasi-resonant (Qres). The exact energy levels for these quantum dots have not been mapped out and therefore we need to look for the p-shell. To do this the wavelength of a MIRA laser is scanned 5-20 nm below the resonant emission, which is the region that InAs quantum dots have their quasi-resonant levels. However, these quantum dots did not react to laser excitation in the quasi-resonant wavelength range at all. The solution found is that the quantum dots can be turned "on" and "off" using 30 nW of ABB laser. Spectroscopy with ABB and MIRA individually did not produce any notable emission, but the combination produced a spectrum that was more than the sum of their parts. This is a puzzling phenomenon that I will not explore further, compiling a model of exactly what is happening is outside the scope of this thesis. This oddity means that 30 nW of ABB excitation will be present in every measurement from

Figure 22: Droplet quantum dot quasi-resonant excitation with CW MIRA. Left: Compared with the spectrum produced by the aboveband excitation in Figure 20 this spectrum is more clean. The astute reader will notice a slight offset in centre wavelength between this and the aboveband spectrum. The Qres excitation is done at ~3 Kelvin lower temperature which tunes the emission wavelength. Right: The quantum dot now saturates at considerably higher power suggesting that the quasi resonant excitation is not as efficient as the aboveband.

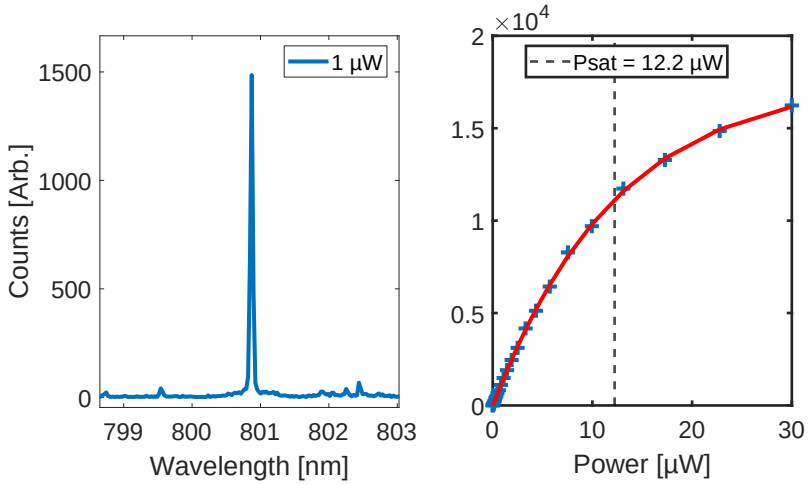

this point on for the rest of the chapter. Scanning in the Qres region the frequency producing the brightest emission is identified. This *is* theorized to be the p-shell, but it could be Qres. The maximum emission was found with the laser at 790 nm ~11 nm lower than resonant (see Figure 22).

Comparing the saturation power between the ABB and Qres excitations, the Qres is significantly less efficient. A power series of the Qres transition indicate a significantly higher saturation power than that of the ABB. This indicates that the quantum dot is well coupled to the waveguide experiencing slight Purcell enhancement reducing the coupling to the out of plane dipole modes. Between the previous ABB measurement and the Qres, a thermal cycle of the cryostat had been performed lowering the temperature of the sample by approximately 3 K, this also slightly changes the emission wavelength due to thermal contraction straining the quantum dot.

A CW g^2 measurement of the quantum dot emission from Qres excitation is performed. Emission is collected and filtered on the grating filter and then using the HBT set-up the photons are correlated (from Figure 18). After an attempt at low power it was realized that the photon statistics were too low for meaningful measurements, so the power was set 1 µW below saturation, as illustrated in Figure 24.

To calculate the g^2 a fit of the centre dip at $\tau = 0 \pm 10^4$ ps is required. The dip is a convolution between the Gaussian instrument response function (IRF) and a double sided exponential representing the quantum dot decay rate Γ; exciton lifetime exponentially decays, so in a plot with "negative time" it becomes a double sided exponen-

Figure 23: Second order photon correlations of quasi resonant excitation of droplet quantum dot in a photonic crystal waveguide. Left: $g^2(\tau)$ Right: The centre ± 10 ns coincidences. The lowest measured data point is 0.37, but with fitting we can find something closer to the natural g^2. The data is fitted with a convolution of a Gaussian instrument response function and double sided exponential for the quantum dot decay rate.

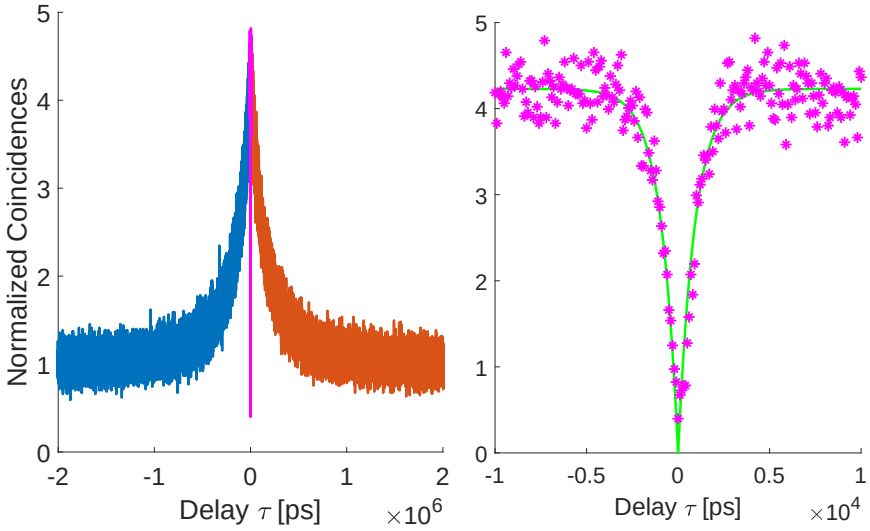

tial. The IRF can be thought of as the temporal resolution of optical set-up and detector. This stems from the response time and timing jitter that occurs in the set-up and detector. The IRF increases the width of the $g^2(0)$ dip with a Gaussian shape, and has been found to have a width of $\sigma = 180$ ps. The decay rate is 0.714 ns^{-1}, please refer to Figure 29. The Gaussian IRF remains constant but the decay rate of the quantum dot is used as a fit parameter for a convolution fit of a double sided exponential from the quantum dot decay. With the mentioned start parameters the convolution fit gives the double sided exponential dip a depth of 0.95 which corresponds to a $g^2(0) = 1 - 0.95 = 0.05$. However, this fit was highly volatile, and simply by changing one starting parameter 10% the g^2 comes out as 0.85. This may not be the correct method of fitting this specific dip, since the uncertainties are also calculated to be in the thousands. Therefore the I will present two g^2s:

1) Using the convolve fit but fitting the data multiple times, each time changing one start parameter up or down 10%, then I take the mean of the $g^2(0)$ and report the standard error on the g^2s. This comes out as $g^2(0) = 0.3 \pm 0.3$.

2) Using the simple method as in the previous chapter. Here the $g^2(0)$ is calculated from a single data point. I assume the coincidences follow Poissonian statistics, such that the uncertainty on the time bin is the square root of coincidences in the bin and divide it by the mean of data points further than the bunching caused by blinking.

Figure 24: Quasi-resonant g^2 with CW MIRA in log(|τ|). The bunching effect from blinking is fitted with an exponential decay. This shows blinking happening on 5.79 µs time scales.

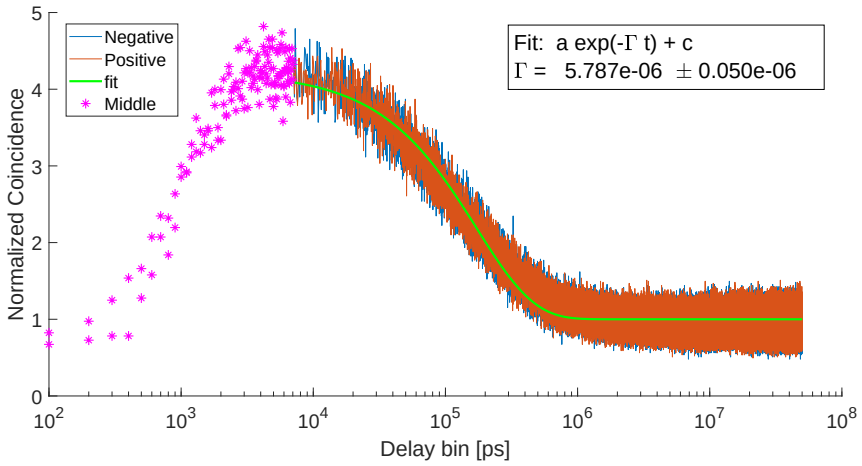

This comes out to $g^2(0) = 0.37 \pm 0.07$. Since the second method is more accurate, this is the one I will move forward with and report.

By plotting the $g^2(\tau)$ in log-time with the negative time values projected onto the positive axis, the photon bunching surrounding $\tau = 0$ becomes very apparent Figure 24

The exponential fit of the bunching part of the g^2 reveals that blinking with a duration $1/\Gamma = 5.79 \pm 0.05$ µs. This measurement was taken at a power close to saturation, to increase the amount of otherwise very low photon statistics. This has probably induced more blinking events in the quantum dot than what could be done with these dots at lower power, but that does not necessarily translate to longer blinking duration. When the quantum dot blinks it gives rise to instabilities in timing of single photon measurements as no photons are produced for the blinking duration. It can be circumvented by using pulses slower than blinking to excite the quantum dot, but that significantly reduces the speed at which the quantum dot operates. For comparison blinking on the 100 ns time-scale has been reported for InAs quantum dots [39].

3.2.1 *Pulsed - Quasi-resonant Excitation in Photonic Crystal Waveguide*

Having done CW measurements on the quantum dot, the next step would be to see if coupling and g^2 would improve switching from CW to pulsed measurements. The MIRA laser produces pulses with a repetition rate of 72 MHz. This ensures that the quantum dot has time to relax before the next pulse, even considering blinking. The same measurement procedure from the previous chapter is followed, to produce both power series and g^2. A notable change to the saturation measurement is that excitation of the ground state to the quasi-

Figure 25: Pulsed MIRA Quasi-resonant saturation fitted with Rabi oscillation. Psat describes the power required for a π pulse.

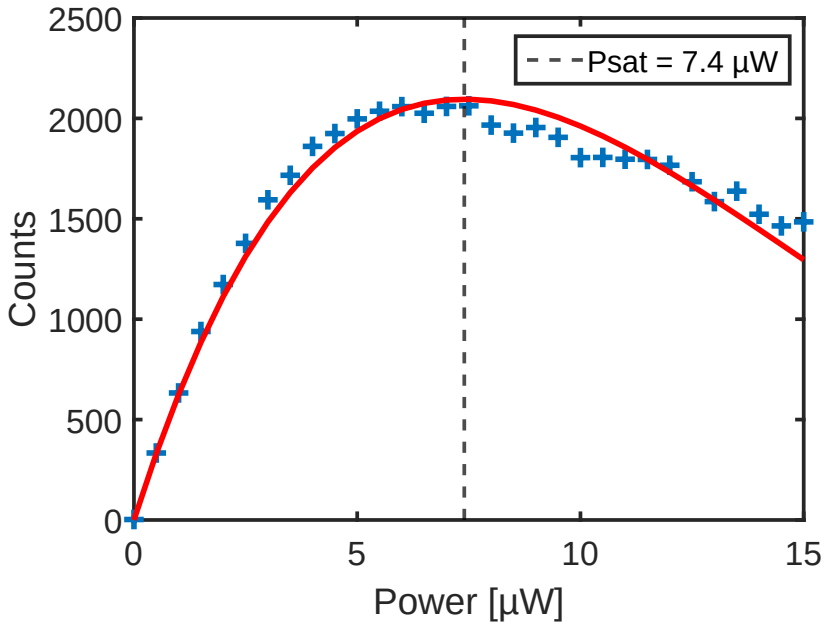

resonant state form a two-level-system that under pulsed excitation follows the Rabi model. Therefore calculating the saturation power is different. The quasi-resonant pulsed power series can be found in Figure 25.

Under pulsed excitation the quantum dot saturates at lower power than with CW action. This is due to the pulse concentrating more photons in shorter time intervals increasing the instant chance the quantum dot is excited.

Performing g^2 measurements with pulsed excitation reduce the chance of laser pollution in the measurement. This benefit is largest when performing resonant spectroscopy, since we easily filter the light with the grating filter. Photon correlation measurements with pulsed excitation look different to CW. Instead of having $g^2(\tau \neq 0) = 1$, there are no photons in between laser pulses meaning that the g^2 of pulsed action switches from 0 to 1 at the rate of the laser repetition which comes out to $1/72$ GHz = 14 ns. In the "lattice" of peaks there will be one missing at $\tau = 0$. This means that we can fit multiple peaks and use their width as a benchmark for the width of an integration of coincidences to get $g^2(0)$. The g^2 can be seen in Figure 26.

Due to blinking causing bunching around $\tau = 0$ the $g^2(0)$ is calculated by fitting peaks further out than the blinking, and using them as reference for $g^2 = 1$. As can be seen in Figure 26 the convolve fit does not quite fit the $g^2 = 0$ area particularly well, which is why instead of using the fit function for calculating the $g^2(0)$ I will integrate the area around $g^2(0)$ with the Full-Width Half-Maximum (FWHM) of

Figure 26: Quasi-resonant g^2 with pulsed MIRA excitation. The data was fitted with the convolution of a two-sided exponential and the instrument response function. The fit does not quite fit the data points at $g^2(0)$, so to find $g^2(0)$ the data points were integrated in a width around 0 delay, equal to the mean FWHM of photon-bunching peaks outside of blinking time-scales giving $g^2(0) = 0.12 \pm 0.04$

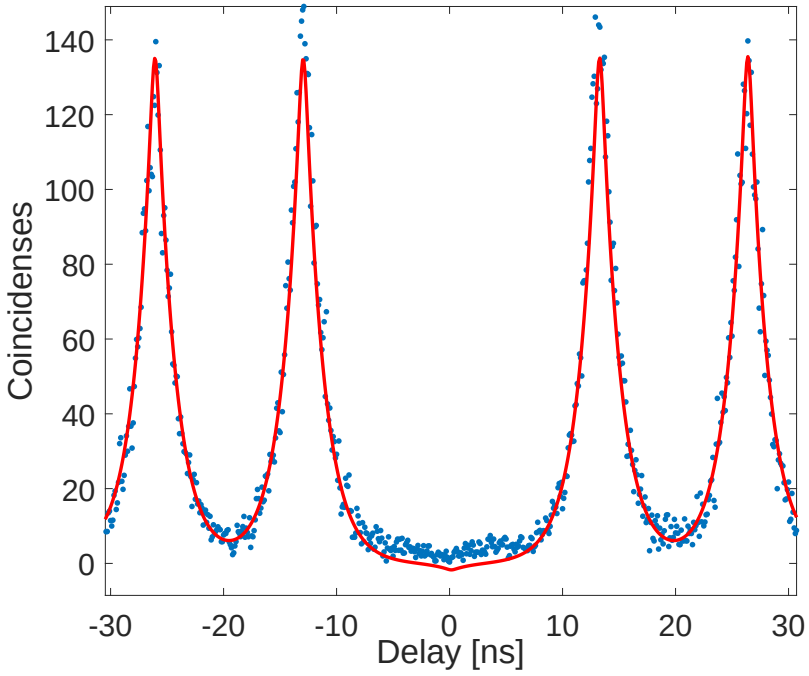

Figure 27: Spectrum of phonon assisted biexciton using pulsed MIRA. The laser is situated at lower wavelength just outside the view of the spectra. The exciton and biexciton are located at 800.9 nm and 802.4 nm respectively.

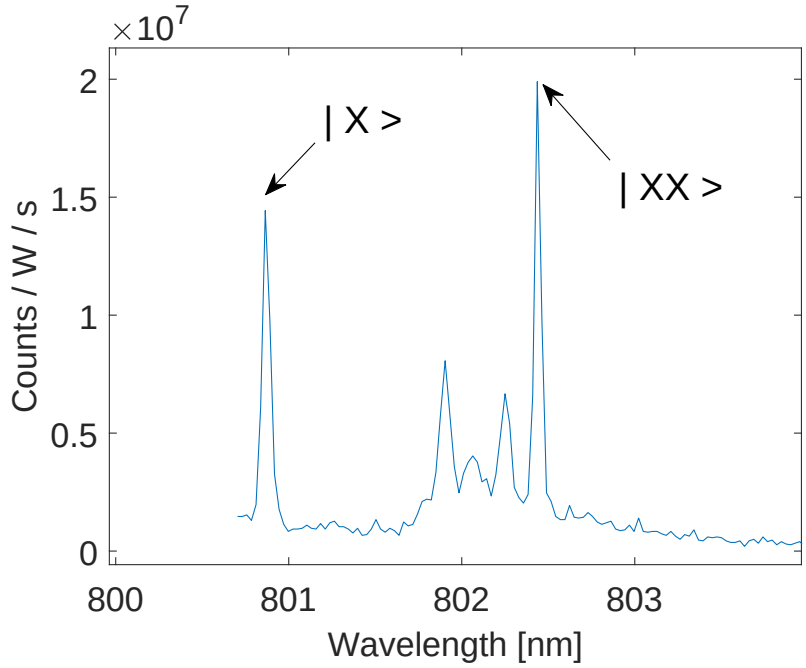

the peaks far away. This method results in $g^2(0) = 0.12 \pm 0.04$. Where the error is found from the standard error on the FWHM of peaks far away. This $g^2(0)$ is significantly lower and more precise than for CW action.

3.3 BIEXCITON WITH ASSISTED 2-PHOTON EXCITATION

An attempt at a clean two-photon excitation was performed. Scanning the CW MIRA laser wavelength from the exciton towards higher wavelength about 0.5-3 nm no biexciton appeared. We therefore tried a different method. Tuning the laser to just slightly higher energy than the exciton we can excite the quantum dot with a regular exciton and then excite another exciton via a higher level. The second exciton should quickly decay to the biexciton state - creating a phonon assisted biexciton. Exciting through a higher level means that that the full decay dynamics are now more complicated, and this method not recommended for general use. As stated before the quantum dots on this sample behaved anomalous, and this was the only method we could excite a biexciton. The spectrum of the exciton and biexciton can be seen in Figure 27.

By collecting the biexciton and exciton from the same SEG and then splitting them on the grating filter, we can do individual measurements of their saturation Figure 28. Surprisingly the biexciton saturates at much lower power than the exciton. The power for maxi-

Figure 28: Pulsed saturation curve of exciton and biexciton emission from the biexciton cascade. Rabi oscillation fits of the saturation show that the biexciton saturates at lower power than the exciton.

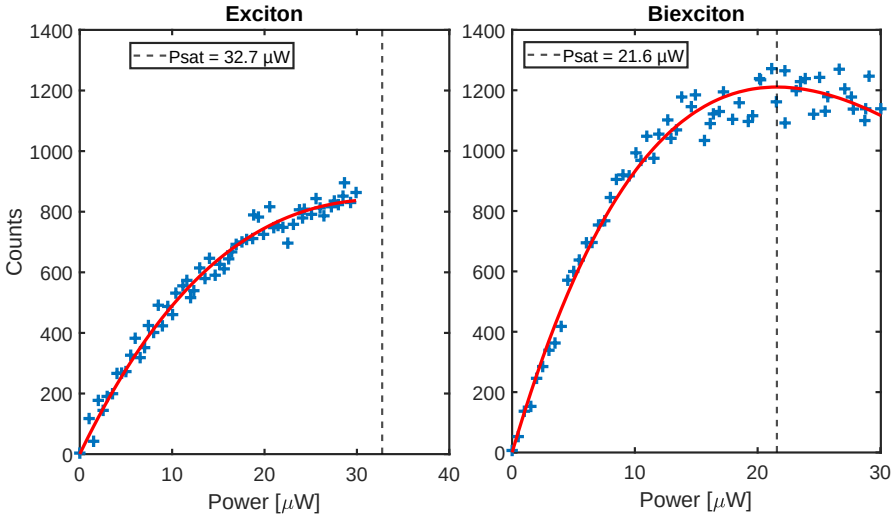

Figure 29: Decay rate of biexciton and exciton. The rates fit such that $\Gamma_X X \approx 2\Gamma_X$

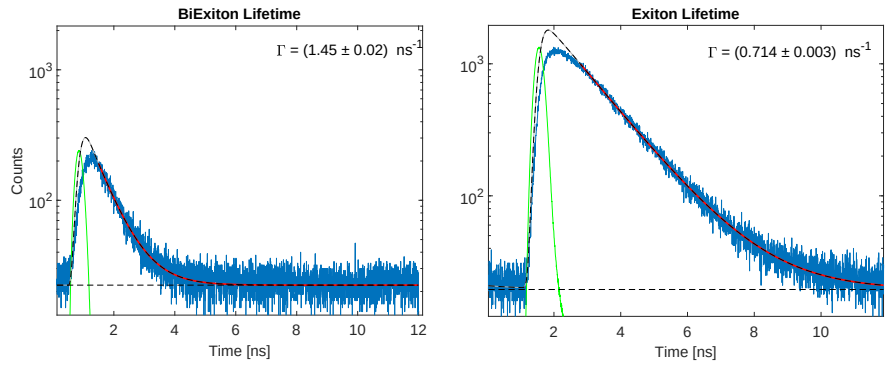

mum probability of entering the biexciton state is calculated from the Rabi π pulse model, which for the biexciton is at 21.6 μW while for the exciton it is 32.7 μW. For a clean biexciton we would expect these to be similar, but by going through a higher energy state the intricate processes become more complicated. The exciton having higher saturation power indicates that the biexciton doesn't always decay into the exciton state, and that a worse excitation of the biexciton (at higher power) couples better to the exciton.

Having split the exciton biexciton emission in two we can also take a look at the lifetimes of the two Figure 29. The decay rate of the exciton should be double that of the exciton. From single exponential fits of the lifetime a ratio of the two decay rates is: $\frac{\Gamma_{XX}}{\Gamma_X} = \frac{1.45}{0.714} = 2.03$. Which fits with what is expected of the biexiton and exciton.

With a decay rate of $0.714 ns^{-1}$, and the blinking duration being 5.7 μs, we can calculate how many single photons would be lost during a blinking event. $n_{photons} = 5.78\mu s \cdot 0.714 ns^{-1} = 4070$ lost photons

Figure 30: Left: Illustration of the pitch of the shallow etched grating (SEG). Right: One of three transmission scans with SuperK of nanobeam waveguides with different SEG pitches on the droplet sample. The black "- -" line is the centre wavelength of quantum dot emission of a future sample. In dark blue is the SEG pitch = 0.306 µm that seems to fit that criteria the best.

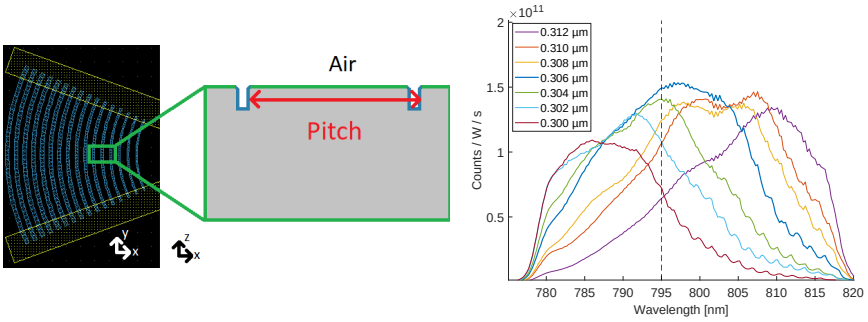

per blink. "Imagine requesting something 4070 times before it shows up, and then what shows up is two of the thing instead of one". This blinking is quite bad for deterministic operation of the quantum dot, unless one operates the quantum dot at speeds slower than the blinking.

3.4 OPTIMAL SHALLOW ETCHED GRATING PITCH AND A NEW SAMPLE DESIGN

A new droplet dot wafer was meant arrive that I should continue biexciton measurements on - but due to the COVID-19 pandemic this did not come to pass. Instead I was tasked with creating the schematic (commonly referred to as a mask) for fabrication of the next sample. As stated in the beginning of the chapter the parameters used were not yet fully optimized, so the measurements on this sample would work as a baseline for the next. The shallow etched gratings (SEG) pitch (see Figure 30) produces the transmission envelope, and is therefore important to optimize. We had been informed in advance that the droplet dots on the new sample would have a centre wavelength of 795 $\pm$ 10 nm, so we would aim for this as a centre transmission wavelength. Transmission scans of nanobeam waveguides using SuperK filtered at 780 nm and 850 nm, performed on SEGs with 7 different pitches in 3 different areas of the sample (see Figure 30). From all three data sets, it seemed clear that the 0.306 µm pitch would fit best, although no analysis further than a quick inspection was performed. For the photonic lattice structure parameters, we didn't do much inspection of the photonic band gaps so the parameters of the PCW studied in this chapter were used as new centre values (a = 206 nm, r = 46 nm). This is also around the time the sample was rendered non-functional such that further measurements could not be conducted.

I designed a new sample Fawkes21 ("phoenix out of the old sample, and the COVID-19 pandemic"), with a few improvements in mind.

1) One of the major problems with the sample featured in this chapter is spectral diffusion. As stated early in the chapter very few dots had narrow linewidth. This is fixed on Fawkes21 by having an integrated effective capacitor to induce an electric field on the quantum dots to halt electron flow and heavily reduce spectral diffusion. This should also prevent having to constantly have 30nW of ABB laser on for all measurements*.

*I cannot take credit for this idea as it was decided before I started, but having done the measurements presented in this chapter and I definitely agree with the decision

2) Aligning lasers to nanophotonic structures is not a completely trivial matter, without very careful protocol, ensuring optimal alignment and throughput of a device is difficult. With experience gained from working on another sample (Chapter 5), that having nanobeam waveguide alignment references close to all photonic structures significantly helps work flow, quality control and overall confidence.

3) The sample features 3x4 write fields wherein devices can be "printed" see Figure 31. This is to allow as many interesting devices as possible, and to make sure there will be functioning devices no matter what. The sample features nanobeam waveguides (NBWG) in every write field with devices that use SEGs. The device features photonic crystal waveguides (PCW) for performing spectroscopy on Purcell enhanced quantum dots. It features glide-plane waveguides (GPW) for creating a path entangled photon source though the biexciton cascade. And to quantify chiral coupling of the GPWs. The sample also features Single Sided Devices (SSD). These are PCWs with the crystal closed off and only a single SEG. This allows near unity collection of single photons emitted from the quantum dot [7]. These devices are useful for quantifying and operating a single photon source quantum dot. The SSD write fields also contain NBWGs with increased width from the single mode 260 nm to the multi mode 300 nm. If finding quantum dots in photonic structures is difficult we want some devices that feature larger width defects for a higher chance of having a quantum dot in the waveguide. Then there is a write field for L3 Cavities, I will not go into detail with these in short they are cavities made by removing just a few holes of a photonic crystal. Cavities can have very high Purcell enhancement which could be interesting to study. Something I have not discussed is that light propagation in semiconducting (any) material comes with some loss. Exactly how much can be quantified with a ConCentric Waveguide (CCW) the nanobeam waveguides in this field all have different lengths, allowing probing of propagation losses. Lastly a field of PCW with lattice constants scanning at double the pace of the regular PCW. The new parameter space would require fabrication to produce smaller lattice hole radii than they had previously done, therefore more "extreme" structures were included as a fail safe. The structuring of the top 3x3 write fields to not sit uniformly is a premeditated decision. The capacitors used to

Figure 31: The Fawkes21 sample featuring gated GaAs droplet dots in: Glide-plane waveguides (GPW), photonic crystal waveguides (PCW), single sided devices (SSD), photonic cavities (L3Cav), concentric waveguides (CCW), and photonic crystal waveguides with expanded parameter space (PCW+). All write fields except for the cavities also feature nanobeam waveguides for alignment.

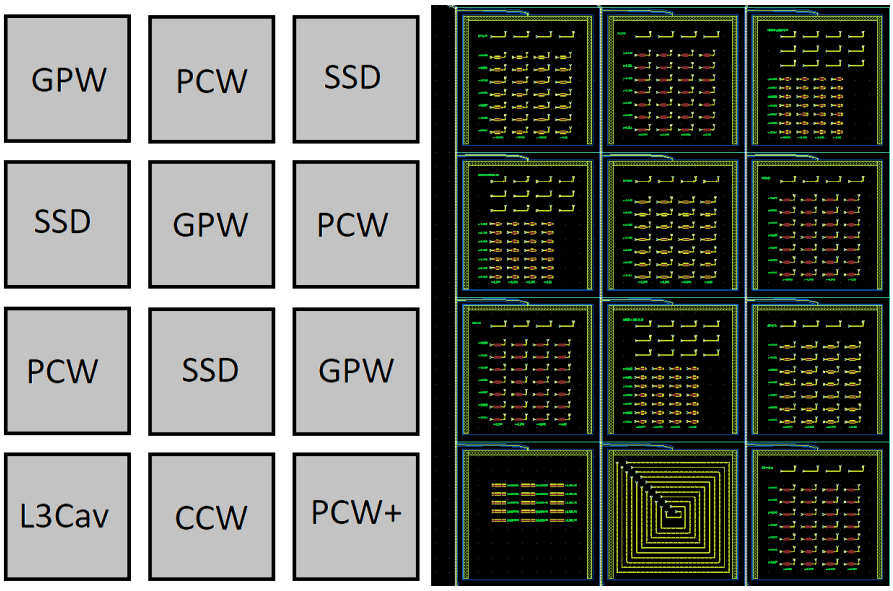

induce electric fields in the quantum dots are connected electronically along the column. Fabricating and connecting these very delicate devices to a voltage source is tricky and can sometimes fail. Therefore there is a unique write field in every column and row to improve success rate. Designing the Fawkes21 sample was the last experimental thing I did for my masters thesis, and new experiments are currently being run on it.

CONCLUSIONS ON DROPLET DOT SPECTROSCOPY

The passive droplet dot sample suffered from heavy spectral diffusion, which lead to wide quantum dot emission. This combined with the wide parameter sweep for finding good transmission resulted in limited options for spectroscopy.

The quantum dot found in a photonic crystal, was in proximity to another quantum dot as could be seen from aboveband (ABB) excitation. The quantum dot showed relative low brightness compared to InAs quantum dots. With ABB the quantum dot saturated at 1.92 µW.

An attempt at resonant fluorescence was performed but failed due to low dot brightness.

Next quasi-resonant excitation was performed by scanning the laser frequency 5-20 nm below resonance. This excitation could be p-shell since it was the brightest quasi resonant (Qres) excitation. During these measurements it was realized that the quantum dots require constant application of ABB laser to be "turned on". With Qres ex-

citation the spectrum was much cleaner, suppressing excitation of the second quantum dot seen in the ABB spectrum. The quantum dot also saturated at higher power, indicating that the quantum dot dipoles couple to the photonic crystal. With pulsed Qres excitation the saturation or π pulse power was lower, attributed to the increased instant power within a pulse compared to CW.

The single photon properties of the quantum dot was quantified with g^2 measurements of CW and pulsed Qres excitation a $g^2_{CW}(0) = 0.37 \pm 0.07$ compared to pulsed $g^2_P(0) = 0.12 \pm 0.04$. Compared to state-of-the-art InAs dots $g^2(0) = 0.015 \pm 0.005$ (Uppu et al. [8]), this is not impressive.

The blinking duration was calculated from the CW g^2 measurement and comes out to 5.79 ± 0.05 µs. Deterministic operation of this quantum dot (assuming no other losses) would produce 172 thousand photons per second, which is ~700 times slower than Uppu et al. [8].

Phonon assisted 2-photon excitation to the biexciton state was performed. Power series indicated that the exiton required higher power than the biexciton to reach a π pulse. The decay rate of the exciton and biexciton matches theory of $\Gamma_{XX} = 2\Gamma_X$. And the decay rate of the exciton is $0.714 \pm 0.003 ns^{-1}$.

The design of Fawkes21 gated droplet sample was shown and drew from both quantified values and my experiences working with integrated photonics throughout this thesis.

4

GATED SELF ASSEMBLED QDS IN GLIDE-PLANE WAVEGUIDE

In this chapter the coupling of gated self-assembled InAs quantum dots to glide-plane waveguides (GPW) is investigated. First a general look at the GPW transmission spectrum for different lattice constants and hole radii. Then resonant transmission will reveal the coupling of a quantum dot to the GPW, and resonant fluorescence of another dot will give insight into the voltage bias tuning of the quantum dot. The decay rate of a quantum dot will be probed for comparison to the droplet dot in the previous chapter. Lastly the AC-Stark effect will be demonstrated through p-shell excitation with different polarizations.

Measurements (except for one) in this chapter are done on the "RobustHOM" sample. Also known as the magic sample receiving its nickname from having *magically* fast decaying self-assembled InAs in GaAs quantum dots. The sample is also gated, which means an integrated capacitor can apply a voltage bias to the sample. This allows tuning of the quantum dots by straining the quantum dots and also reduces spectral diffusion reducing the quantum dot linewidth.

4.1 GLIDE-PLANE WAVEGUIDE TRANSMISSION SPECTRA

To understand the GPW, it is nice to have a general idea of what transmission through the structure looks like. The glide-plane band-diagram can be engineered to have a bandgap (interesting for slow light applications) but does not necessarily feature one (Mahmoodian et al. [17]). Unfortunately the GPW transmission was not measured on the RobustHOM. It had to be done on a different sample (HybridMask) due to time constraints. The HybridMask GPWs are very similar to the ones featured on RobustHOM, except for the quantum dots, which we do not care about for regular transmission measurements. The transmission of a select few can be seen in Figure 32. The transmission measurements were done using the SuperK laser (Section 2.3.3), bandpass filtered between 900-980 nm, but no interesting features appear above 955 nm.

Looking at the lattice constant a = 255 nm structures, we see a very consistent bandgap tuning with a wide range. Except for the bandgap the overall transmission features do not seem to follow a pattern. The bandgap tunes linearly with ~10 nm per 2 nm hole radii. For the a =

Figure 32: Glide-plane waveguide transmission with highlighted areas presumed to be bandgaps. For the a = 255 nm structures we see a clear band gap that moves towards lower wavelength as the radius of the holes increase by about 5 nm bandgap per nm hole radius. The a = 265 nm structures behave quite differently. First off they seem to tune in the different direction and also seems to have two distinct bandgaps.

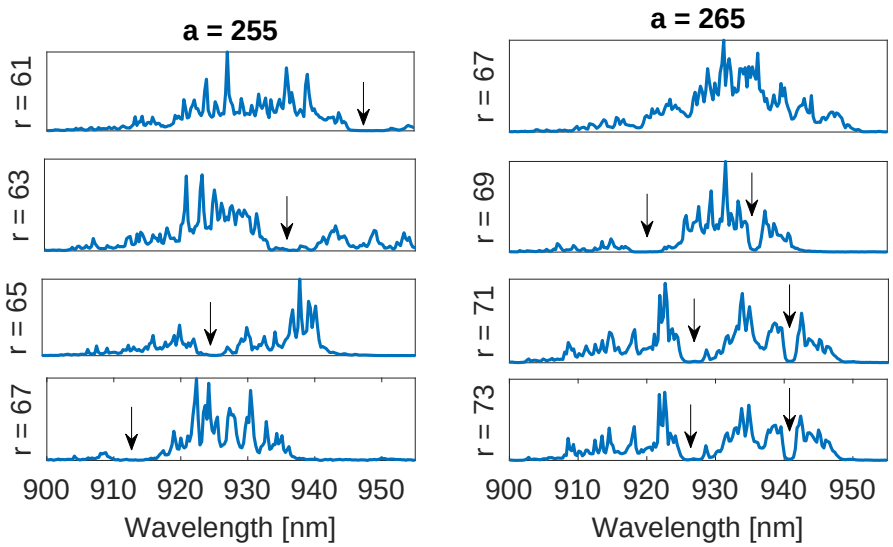

265 structures, we see two bandgaps very suddenly appear between r = 67 nm and 69 nm. The two gaps also seem to tune inhomogeneously with the radius as well as the opposite direction of the a = 255 nm structures. For r = 71 and 73 nm the bandgaps do not seem to tune at all, but the overall spectrum looks very similar. This could be due to a fabrication error, or an error in the data gathering process. The origin of the two bandgaps in one structure is unknown but could be speculated to be an inherent property of the glide-plane, when compared to the extra mode found in Figure 9.

4.2 RESONANT TRANSMISSION OF QUANTUM DOT IN GLIDE-PLANE WAVEGUIDE

Opposed to the passive droplet dot sample this sample is gated. This means that quantum dots needs to be turned on by applying a bias voltage. Applying a constant bias voltage and using ABB laser excitation a quantum dot in a GPW was located. After finding the quantum dot, an attempt at resonant transmission is performed. Using ABB excitation, a quantum dot is found in the waveguide, and the resonant frequency of the quantum dot was found. To switch to resonant transmission low power CTL laser is coupled into the glide-plane shallow etched grating (SEG) and a fine frequency scan was performed close to the quantum dot resonance (see Figure 33).

In the full RT scan the quantum dot shows as a few GHz wide dip in the transmission highlighted in blue. The RT scan also shows sig-

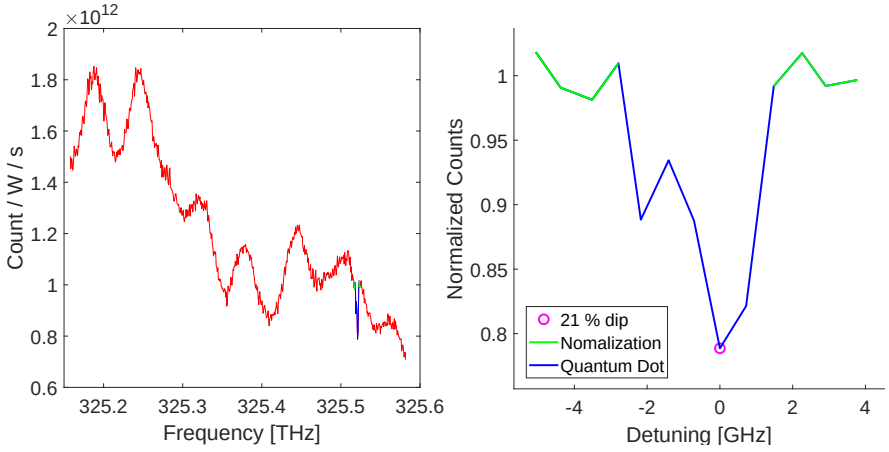

Figure 33: Resonant transmission of InAs quantum dot in glide-plane waveguide. Left: The full resonant transmission (RT) scan, an ideal RT scan is expected to feature constant transmission, except for the quantum dot. Here we see significant oscillations, due to high shallow etched grating reflections. Right: Zoom in on quantum dot reflection. There are two visible dips, these are the two dipoles of the quantum dot. Normalizing with the surrounding counts(green), the quantum dot seems to reflect ~21% of incident light.

nificant oscillations in the spectrum. These oscillations are periodic occurring every ~60 GHz. They could be described by the transmission experiencing a cavity effect with a free spectral range of 60 GHz. Supporting this theory the RobustHOM sample is not optimal for growing efficient SEGs. This causes some of the light incident on SEG to be scattered into the sample and then back into the SEG. This overall increases the reflectivity of the SEGs. Therefore the oscillations are not a property of the GPW but rather of unfortunate etching conditions on this sample. Despite the oscillations, the quantum dot is still quite visible having a linewidth of a few GHz. Due to the heavy oscillations the RT dip will have to be normalized by only a few local points. The amount of light transmitted at quantum dot resonance is 79%, meaning the quantum dot reflects ~21%. This is a good measure of how well the quantum dot is coupled to the waveguide. In theory the quantum dot should reflect 100%, but if it is situated at the edge of the waveguide, or even a little ways inside the photonic crystal, it will not reflect 100%. It could also be that the quantum dot was saturated and could not reflect any more, but the incoming power on the quantum dot is less than 10 nW in this case, which should not be enough for saturation.

4.3 RESONANT FLUORESCENCE OF QUANTUM DOT IN GATED GLIDE-PLANE WAVEGUIDE

A quantum dot in a different GPW was excited out of plane with resonant fluorescence (RF). First the quantum dot is found by setting the gate voltage such that the quantum dots are "on" and using ABB

Figure 34: Resonant fluorescence of quantum dot in glide-plane waveguide. The horizontal axis depicts the laser frequency, and the vertical the wavelength of collected light. The bright yellow line scanning from low to high frequency is the CTL laser, that is also collected. Vertically the quantum dot wavelength is visible as a feint line slightly brighter than the background. When the laser frequency resonates with the quantum dot at 327.12 THz, it emits light broadened by the high power laser excitation.

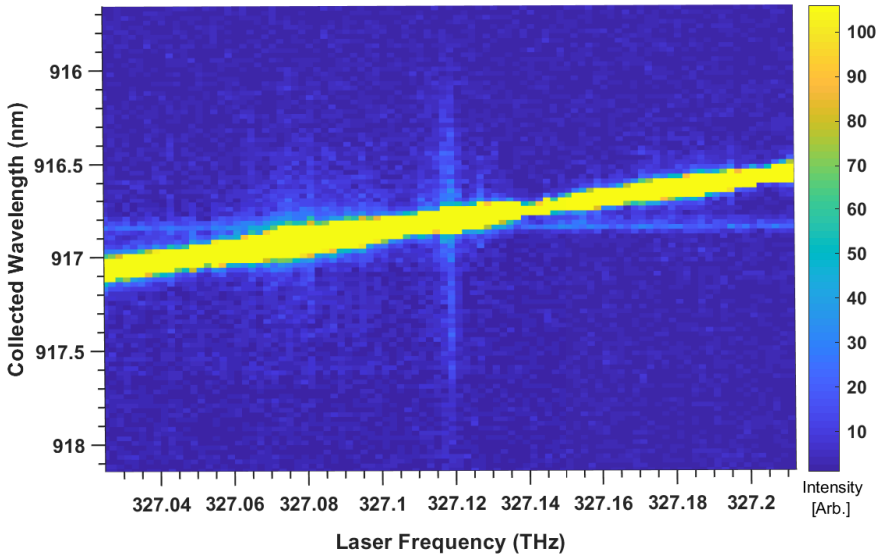

excitation collecting emission a SEG of the structure. Knowing the resonant frequency of the quantum dot it is possible to scan the CTL laser (Section 2.3.2) frequency finely across the quantum dot emission wavelength at high power and collect the emitted light on the spectrometer to view the resonant fluorescence as seen in Figure 34. The CTL polarization is cross from the collection SEG, to reduce laser scatter, however the laser still bleeds through due to high power.

The laser is at relatively high power so quantum dot emission is visible even when detuned. As the laser tunes from low wavelength to high it hits resonance with the quantum dot around 327.12 THz. The saturated quantum dot emits with a wide linewidth visible on the spectrometer. This measurement was done with a fixed gate voltage. This also demonstrates how much easier it is to perform resonant fluorescence with a tunable laser and a gated structure compared to the droplet dot where we were unable after doing much more work.

To showcase high control of the quantum dot in the GPW the resonant frequency can be tuned using the gate voltage, while also scanning the laser to follow the RF. Thereby we perform resonant fluorescence at multiple different frequencies. For this the CTL laser power is reduced significantly below saturation to avoid broadening effects, and to increase resolution the spectrometer is changed out for the grating filter and an APD in such that we can resolve the quantum dot linewidth. Figure 35

Figure 35: Resonant florescence of quantum dot in glide-plane waveguide, with voltage tuning. The data is normalized with the maximum count at each frequency and displayed at its respective frequency. The resonant fluorescence can be seen as the quasi-step function that tunes from 15-35 GHz. A linear fit of the top points of each step gives a slope of 450± 30 GHz/V

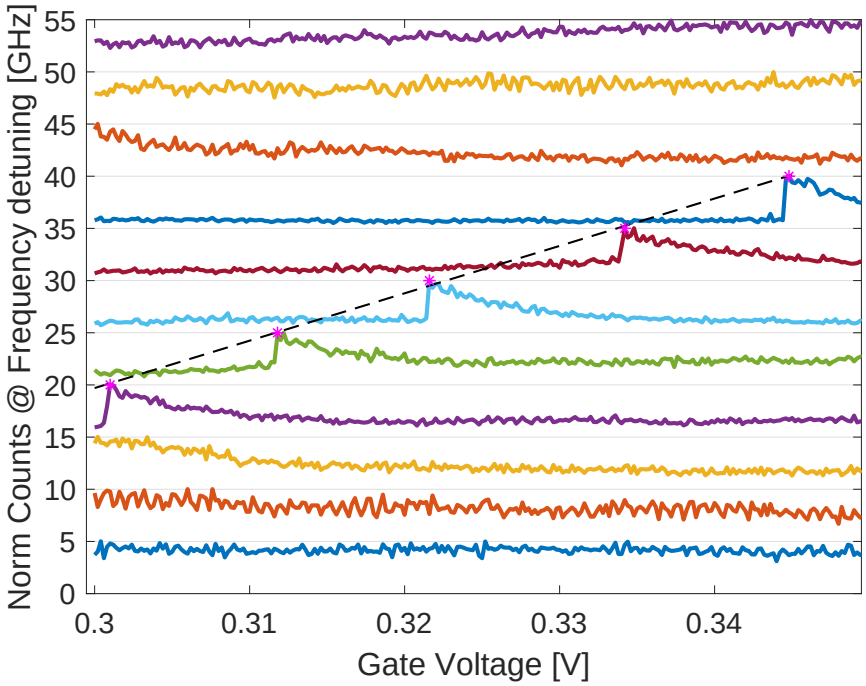

As mentioned earlier the SEGs on these structures were not optimized creating cavity effects in the waveguide. This effectively convolves the Lorentzian quantum dot emission with the cavity modes, creating a Fano line shape which looks similar to what we see in Figure 35. However, multiple attempts at fitting these line shapes with a Fano line shape have come close but ultimately failed. The cause is currently unknown. A possibility is that the SEG do not produce perfect cavity modes, which would alter the convolution.

To demonstrate control of the quantum dot in the GPW we luckily do not require a consistent emission line shape but rather that said line shape tunes with the gate voltage. With Fano lines the centre of the step in the convolved line shape is the centre of the natural quantum dot emission, and is normally used for fitted quantum dot tuning. However the shapes are only quasi-Fano, so instead the top points of the steps have been used, which seems consistent. All though not mentioned in Chapter 1, quantum dots in gated environments usually tune quadratically with voltage bias. In this case the amount of data points and range is so small that the quadratic tuning becomes linear.

Figure 36: Lifetime measurement of fast self-assembled InAs quantum dot. An exponential decay fit is in red revealing the decay rate of 5.42 ns^1. In orange the instrument response function of the APD is visible

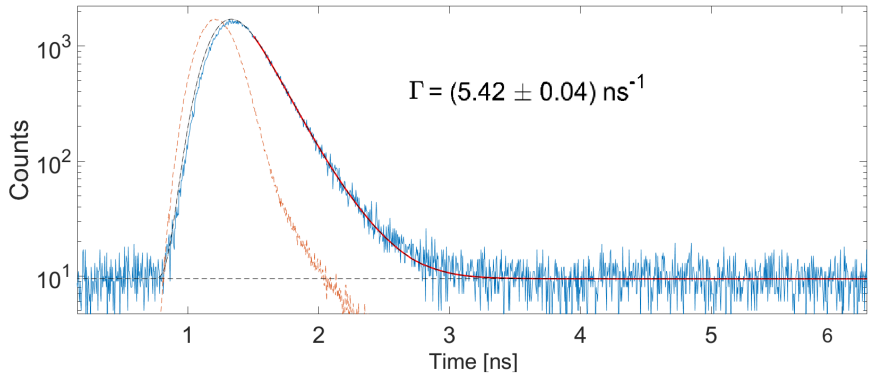

4.4 DECAY RATE

The decay rate of the quantum dot also used for RF is probed using p-shell excitation with the pulsed MIRA laser. Filtering the emission with the grating filter and then collecting with an APD, a lifetime measurement of the quantum dot is performed Figure 36.

The decay rate of this InAs quantum dot can be compared to the decay rate of the droplet dot in Figure 29. This InAs QD is $\frac{5.4ns^{-1}}{0.71ns^{-1}} = 7.6$ times faster. As mentioned at the start of this chapter the quantum dots on this sample are incredibly fast, and have not yet been reproduced, but it still works as a rough measure of how fast the InAs quantum dots can operate if fully engineered. It could also be that the quantum dot in question is being Purcell enhanced significantly. However, the decay rate of this dot matches that of previous studied of dots on this "magic" sample.

To give a more realistic comparison a study on self-assembled quantum dot lifetimes on the Shoshin sample (next chapters sample), was also done for quantum dots in nanobeam waveguides. Although the nanobeam cannot feature significant Purcell enhancement in the same order as the GPW can (compare v_g of Figure 6 and Figure 9) this is still a somewhat fine comparison. On the Shoshin 5 quantum dots in NBWGs had their decay rate measured in a similar way to how it was done here (see Figure 59 in Appendix B). There the average quantum dot lifetime is $0.93 \pm 0.3\ nm^{-1}$. A more fair estimate of the decay rate ratio is then: $\frac{0.93ns^{-1}}{0.71ns^{-1}} = 1.3$. The decay rate of the InAs quantum dots is still higher than that of the (single) GaAs QDs we have inspected.

CONCLUSIONS ON COUPLING QUANTUM DOTS TO THE GLIDE-PLANE WAVEGUIDE

Transmission of glide-plane waveguides was inspected. One set of devices showed consistent linear tuning with lattice parameters. Another varied in consistency, featuring what looks to be two bandgaps than tune non-linearly unlike the first set, this could be explained by the extra dashed mode in Figure 9.

A quantum dot was found with aboveband and consecutively performed resonant transmission yielding a 21% transmission dip, which is an indication of how well the quantum dot is coupled to the waveguide.

Resonant fluorescence (RF) was performed on another quantum dot in a glide-plane waveguide. Tuning the gate voltage, the quantum dot resonance is tuned, which could be followed with laser. RF also displayed pseudo-Fano lineshapes attributed to non-optimal shallow etched grating leading to increased reflections inducing cavity effects.

Quantum dot blue detunes with gate voltage linearly (opposed quadratic, attributed to low data), at $450 \pm 30\mathrm{GHz/V}$

The decay rate of a quantum dot in a GPW is also found to be $5.42\mathrm{ns}^{-1}$, which compared to the state of the art quantum dot (Uppu et al. [8]) is quite ("magically") fast.

5

CHARACTERIZATION OF TOPOLOGICAL WAVEGUIDES

In this chapter a characterization of topological devices is performed. This includes getting a sense of what transmission of topological devices looks like and characterizing what happens to the transmission when altering the crystal parameters and the device length. The topological devices feature mode adapters to the topological edge mode for optimizing transmission, just how much it improves edge mode transmission is calculated. Towards the end a method is presented for calculating the group index of the devices through cavity interaction in nanobeam and topological waveguides, and the results found throughout the chapter will be compared to simulations.

"Shoshin" is a Zen Buddhism word meaning "beginner mind". The Shoshin sample is our groups first sample fully dedicated to studying topological photonic structures. It features over 1800 devices and was designed to scan out a huge parameter space, to find optimal parameters for future generations and probability of finding a good device. The sample is etched in GaAs featuring InAs quantum dots in a low to medium density. The sample was created using a new, untested, fabrication technique which might lead to some inconsistencies with the structures.

5.1 THE SHOSHIN SAMPLE - TOPOLOGICAL STRUCTURES

The Shoshin sample is a 3x3 mm wide GaAs chip featuring InAs quantum dots and topological photonic devices. Topological photonic devices are different from the ones we have studied so far. To create a topological edge mode we need to create an interface between two lattices with different Chern numbers as is requires as introduced in Section 1.3. In the example given, I used circles of different sizes to demonstrate the topological edge mode, the topological devices on the Shoshin sample features shamrocks instead of larger holes to break the 6-fold symmetry (see Figure 38). In the Topology chapter I introduced the Zigzag type device, but the Shoshin also features bearded type devices. The bearded type devices are similar to the glide-plane waveguides (GPW) in that a π/a shifts along the propagation direction are not translational symmetric, which is exactly the requirement for creating chiral coupling in the GPW. Zigzag devices

Figure 37: A singular lattice element of a topological lattice. And two types of interfaces, bearded where the shamrocks meet at the interface, and "zigzag" where the circles meet at the interface

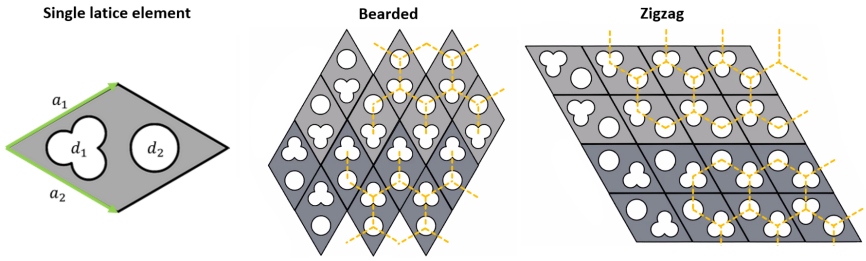

Figure 38: Adapters used for adiabatically adapting light from a nanobeam to a topological mode, for both the bearded and zigzag devices.

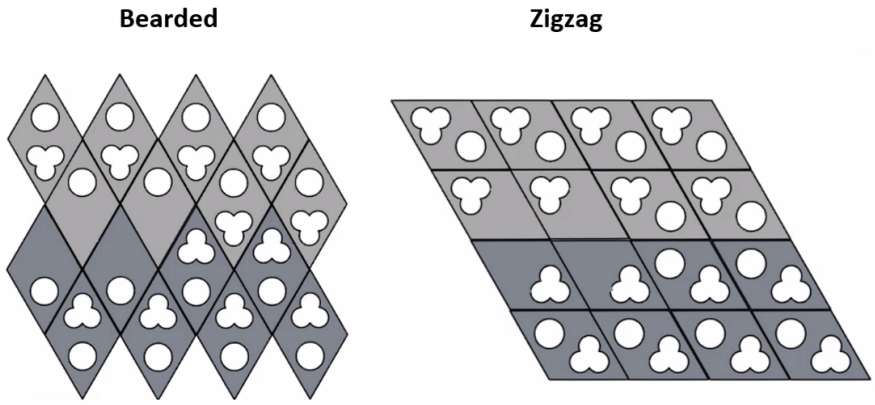

are translational symmetric and are therefore more akin to the photonic crystal waveguides.

Something we have not looked into in previous chapters is the effective coupling of light into the photonic crystal waveguides (PCW) from the nanobeam waveguide (NBWG). Both the photonic crystal waveguide and the GPW features adapters that help couple the light from the nanobeam waveguide mode into the modes of the either photonic crystal or glide-plane. This is usually done gradually changing from the NBWG to the crystal with propagation (in Figure 19, it can be seen as a region where the photonic crystal is less wide). The idea is to adapt the mode adiabatically. The same thing goes for topological crystals and maybe even to a larger degree, where we try not only to adapt to a mode but also to a topological phase (see Figure 38). The effectiveness of these adapters will also be identified in this chapter.

As we learned in Section 1.3 the topological devices do not have bandgaps in the same way as a photonic structure does. When referring to a topological bandgap it refers to the bandgap created in topological insulator. When two topological insulators with different Chern number are brought together a topological edge mode is cre-

Figure 39: The entire Shoshin sample featuring over 1800 structures. The zoom-in shows a column of devices featured with different lengths of photonic crystal L1 = 13 µm and L2 = 23 µm. Each column contains a nanobeam waveguide, zigzag and bearded devices with and without adapters and topological interfaces, making a total of 9 devices per column. Lastly an inlet of a singular device is shown.

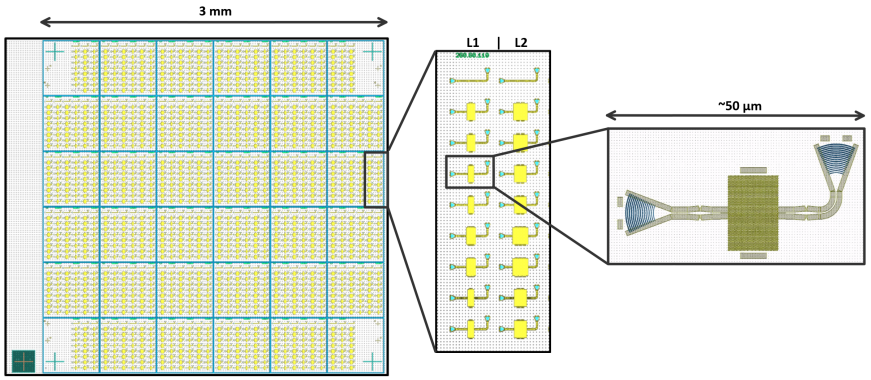

ated connecting the top and bottom of the bandgap effectively closing the bandgap created by the insulators. The way to measure, if a mode is indeed a topological edge mode would be to compare the transmission through a topological insulator with that of a structure featuring a topological interface. If the transmission of a structure featuring a topological interface is larger in the bandgap area, than the one without, the additional transmission is attributed to the existence of an edge mode. For this reason all transmission measurements of topological interfaced devices must always be taken in comparison with one of its topological insulators.

This is one of the reasons the Shoshin have many devices, for each parameter-set there needs to be 1. A NBWG (for alignment), 2. a topologically interfaced device with adapter, 3. a topologically interfaced device without adapter, 4. a topological insulator with adapter, 5. a topological insulator without adapter (and then 4 more of the other type (zigzag vs bearded)) as shown in Figure 39. Additionally to get a better idea of the transmission for each device there are also two different lengths of topological crystal featured 13 and 23 µm. Meaning for each parameter set there is a total of 18 structures. Also because of the possibility of fabrication imperfections the devices were produced in 3 copies.

The parameter sets consisting of different: Lattice constants "a" (in nm), shamrock circles offset from its centre "d_1" (in nm), and radii of the circles "d_1" (in nm).

For easier writing, I will from now on reference topological structures with 3 letters, the first indicates if it features an adapter "A/X" where X means no adapter. Then either "Z/B" for zigzag or bearded. Lastly "T/X", for topological interface T, and no interface X. e.g. ABT is Adapter-Bearded-Topological interface and XZX would be No-adapter-Zigzag-No-interface. Additionally the parameter-set, length and copy

will be written out in order a_d_1_d_2_L_C. With this code in place a full device name could be 270_60_125_L1_C2_ABX.

5.2 FINDING AN EDGE MODE

When scanning out an enormous parameter space it is important to have a "battle plan" as to keep track of numerous measurements. Therefore getting an early idea of what scanning different parameters does to the transmission spectra is crucial.

Since we to be able to inspect a large quantity of structures in a short amount of time using the SuperK laser to instantly probe the entire transmission spectrum is optimal. For these measurements the SuperK was filtered at 875 nm but no filter limiting the upper wavelength was used. The SuperK does not have a constant optical density so we need a reference spectrum. The reference is collected from the NBWG situated in every line of structures. This means that the SuperK measurements going forward will be normalized using the NBWG transmission from its own line. The NBWG is also used for alignment reference, so after maximising SuperK transmission through the NBWG only a translation of the optical set-up is required to measure the next structure. This removed inconsistencies arising from alignment of the laser. An example of a NBWG transmission is seen in Figure 39. For comparison: (Zhou et al. [29]) reported a 74.6% total transmission on similar NBWG devices, meaning that for reference one can multiply numbers by 3/4 to get a rough approximate total transmission.

To check the consistency of the transmission we smoothed away the rough oscillations arising from the SEGs reflecting at higher wavelengths (Zhou et al. [29]), by making each point the average of 5 surrounding data points. Then a to get a measure of the spectral variations a linear correlation calculation between 5 nanobeam pairs was performed. The resulting correlations are all $> 95\%$, so the transmission is very consistent, when using this method of using the NBWG for reference.

We also see that the NBWG transmission is significantly decreased above 980 nm and below 900 nm, and will therefore focus our analysis in this region. To make our measurements even more consistent every time we would perform a measurement series on a row of structures the optical set-up would be aligned to the NBWG in the row (reference Figure 39)and optimize the total throughput - then by only moving the translation stage of the breadboard the alignment of the next structure is performed. This assures that the incident angle is the same, but is still slightly sensitive to offset in the plane.

To start off on the topological devices: The first thing we want to find is a topological bandgap. But the bandgap is not similar to the ones found in regular photonic devices. We are looking for wave-

Figure 40: Transmission spectrum of the SuperK laser through the NBWG in field "270_65_110". The numbers reference the parameters a, d_1, d_2 accordingly in units of nm. Counts have been normalized with power and spectrometer integration time.

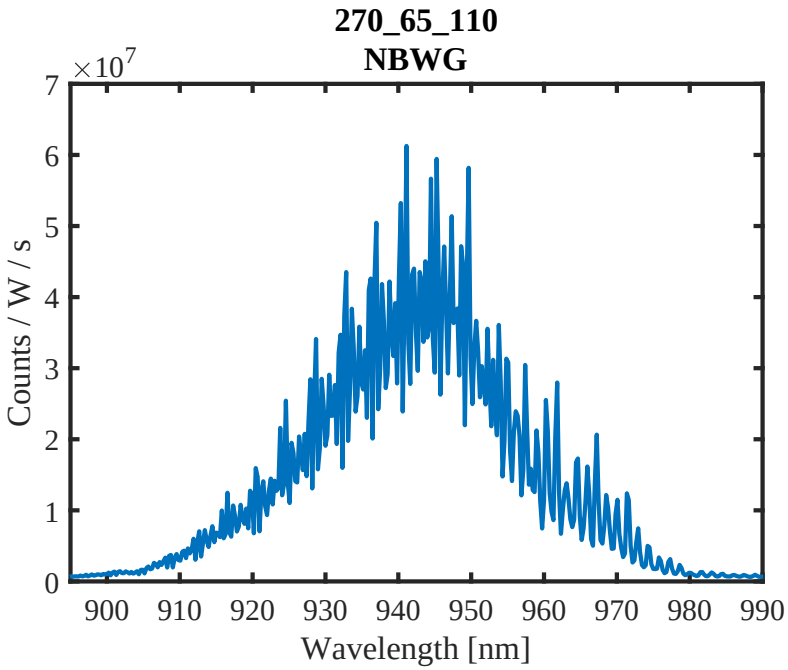

lengths where a topological device transmits and the same structure without the interface does not. Let us inspect a ABT type device and its reference ABX (see Figure 41). The transmission at 910 nm appears to be a bulk mode feature, since it is apparent in both ABX and ABT spectra. The transmission with centre at 980 nm is an indication of a topological edge mode, since there is no transmission in the topological insulator, but there is in the topological waveguide!

5.2.1 *Discards*

Over 200 transmission scans with the SuperK have been performed and it is not all of them that behaved as nicely as the one above (see Figure 42). In *a lot* of the scans we were unable to find any signs of a bandgap at all. There could be multiple reasons for this: The bandgap simply not being in view with the given parameters and faulty fabrication are also very probable. There is also the very real possibility that there is something we simply do/can not understand yet. More than 100 data sets were taken of this kind both for ABT and AZT, and I have decided not to analyse further on these - since most conclusions drawn would be speculation and ad hoc explanations, of what is going on. There are however some qualitative things that we did learn from these data set. The C2 had significantly more structures we understand than C1 and C3, not to say that there were none.

Figure 41: SuperK spectrum of structure a = 290 nm, d1 = 70 nm, d2 = 110 nm, L = 23µm copy 1. The counts have been normalized to the NBWG transmission. At 900-920 nm there is a peak which is present in both the ABT and the ABX spectrum - this indicates that it is not a feature of the topological waveguide but rather one of the photonic structure i.e. a bulk mode. The peaks centred around 980 nm however only appear in the structure with a topological interface indicating it is the edge mode.

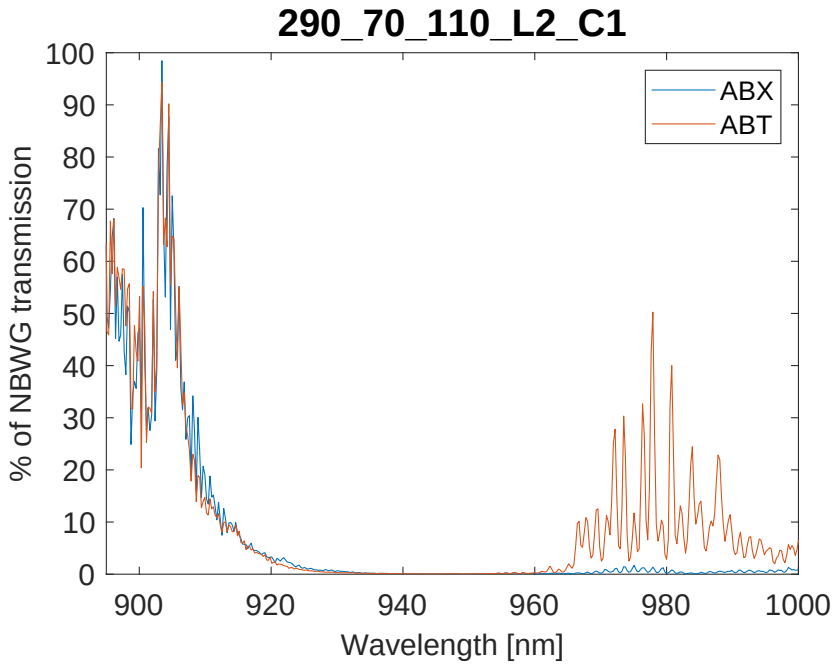

Figure 42: Showcase of some of the SuperK transmission spectra left unexplained. For example a structure without topological interface (blue) having more transmission than one with (red). Some of the structures however do have what could be an open bandgap - but the transmission is very low.

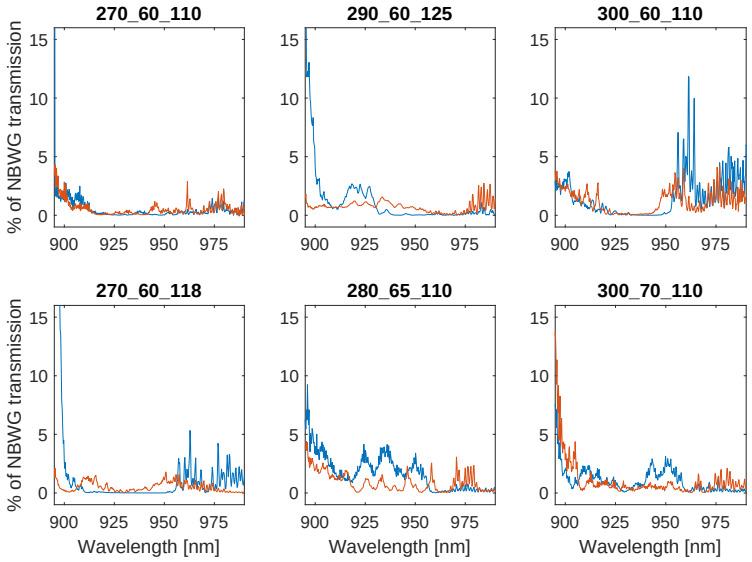

The C2 structures are located at the samples centre, making it likely that the C1 and C3 structures have not been fabricated as nicely.

5.3 CHARACTERIZING THE PARAMETER SPACE

Lets take a look at what happens when we change the lattice constant a. The bandgap of the topological structures should not change between using the bearded or the zigzag interface, therefore for these measurements we focused only the bearded interfaces for speed. To get a good view of what happens when changing a, the other two parameters need to be kept constant. Unfortunately since the Shoshin scans out a large parameter space the resolution between structures is not great. Of all the scans no two structures with a = 260 nm or a = 270 nm shared a bandgap with another structure for constant d_1 or d_2. Unfortunately that means we can only compare two structures ABT a = 280 nm and a = 290 nm, see Figure 43.

Increasing the lattice constant seems to increase the centre wavelength of the bandgap. This also makes sense from the hand-wavy logic of: "Increasing the lattice constant creates more room for k-vectors in the material, leading to an overall longer wavelengths". It does also seem like the bandgap gets significantly smaller, but it is always hard to draw confident conclusions from two data points. Of extra note from this figure structure 280_70_110_L1_C2 has an interesting wide edge mode centred with the SEG transmission as identified of the NBWG. Additionally the edge mode and two bulk modes

Figure 43: SuperK transmission scans with increasing lattice constant "a". Increasing "a" seems to increase centre wavelength of the edge mode. We can also here nicely identify the lower and upper band edge of the 280_70_110 structures spanning from 918 nm to 955 nm (identified as the first place the ABX transmission reappears significantly).

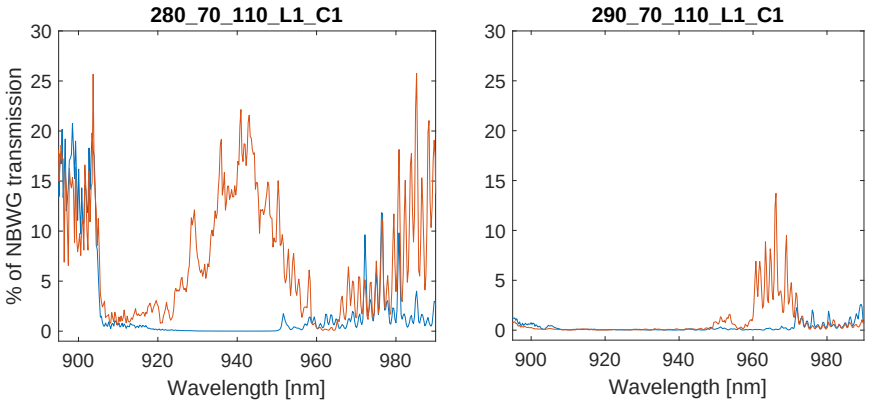

fit neatly within our filtering which will be useful later for CTL scans. A more thorough look into this structure later.

Next let us inspect what happens when alternating the shamrock circle offset d_1. Here there is more data, but we still suffer in resolution from the aforementioned conditions of the Shoshin's large parameter space, see Figure 44.

From the figure it seems that increasing the shamrock spacing decreases the centre wavelength of the bandgap. Once again a hand-wavy argument can be used to explain the behaviour: "Increasing the spacing of shamrocks effectively decreases the amount of material per lattice unit wherein k-vectors can exist, decreasing the wavelength" holds true.

Lastly let us take a look at what happens when increasing the hole radii d_2. Once again we suffer from the large parameter sweep, but here also a lot from devices simply with no transmission, see Figure 45.

Once again this makes sense with the hand-wavy argument of material to air ratio deciding the k-vectors. This is a nice result since it helps with creation of future topological samples, so smaller parameter spaces are required, and allows more premeditated control of the topological edge mode.

As an additional conclusion to this sub-chapter: We have now looked at quite a lot of SuperK scans, and it would seem that in general the bulk modes only appear below ~920 nm. This will be a good indication later for measurements with the CTL laser.

Figure 44: Comparison of shamrock offsets d_1. From the first row we can see what seems to be a bandgap around 960 nm moving to lower wavelengths with increasing d_1. For the second row, the bandgap moves very quickly from around 970 nm to 920 nm with just 5 nm difference in shamrock spacing.

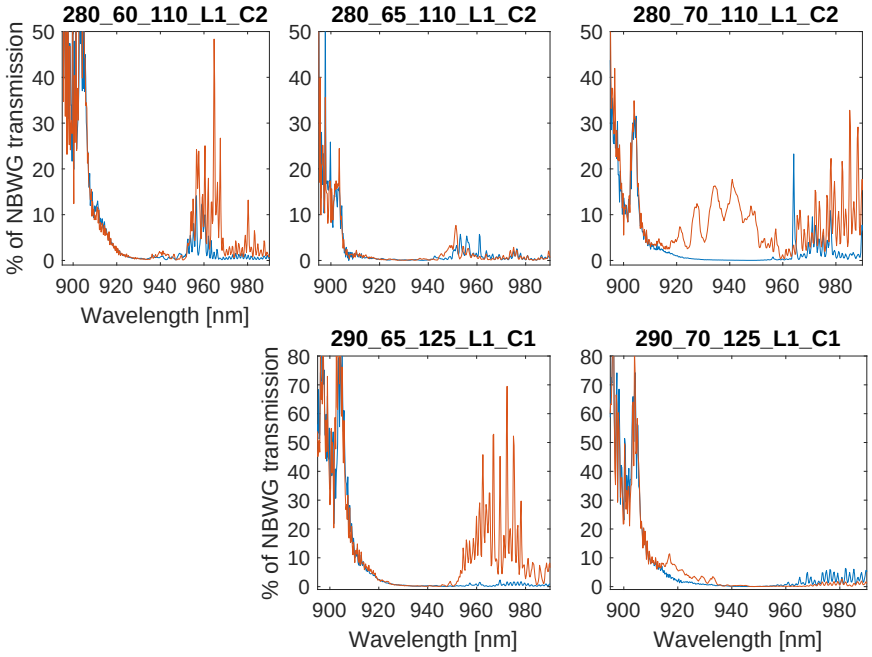

Figure 45: Increasing the hole radii d_2 seems to decrease the centre wavelength of the band gap. On the d_2 figure it even seems the edge mode has almost merged with the bulk transmission.

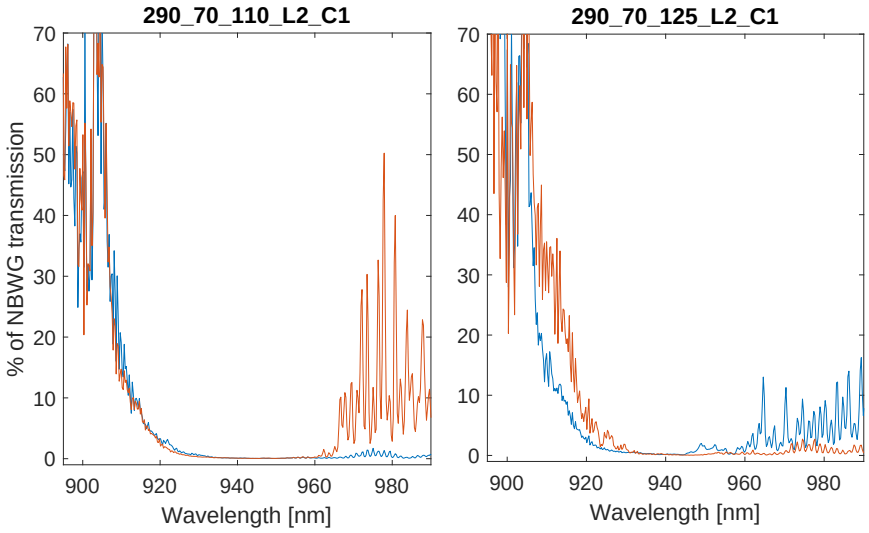

Figure 46: Topological bandgap of 280_70_110 ABT device. The bandgap is here defined as the wavelength span wherein the transmission of the topological interfaced device is larger than the topological insulator and the Poissonian errors assigned to both. Some ABT data points have missing lower error bars, this is due to the uncertainty going below 0 which does not play well with log plots. The gap width is displayed at 1% for no reason in particular.

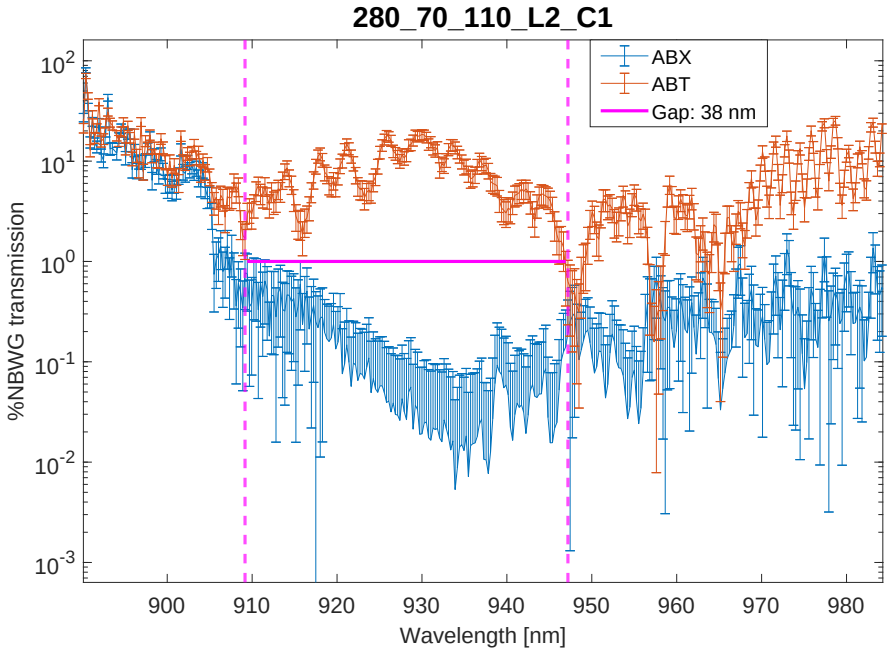

5.3.1 *Topological device length effect on transmission*

The topological crystals on the Shoshin have a device length of either L1 = 13 µm or L2 = 23 µm. Studying the edge mode transmission loss per device length would be most interesting, for gaining but a slight insight into the possible backscattering protection. A precise indication of where the edge mode starts and stops is required. Assuming that the transmission of each bin (like the wavelength bin of the spectrometer) is Poissonian, the standard error on the bin becomes $\sqrt{N}$ where N is the number of entries into the bin (Barlow [40]). Then we can identify the edge mode as the the wavelength span where the transmission T is larger than the uncertainties of the error on T as well as the X and error on X, i.e. $T > X + \sigma_X + \sigma_T$. This method was performed on four ABT devices with parameters 280_70_110, L1/2 and C1/2, and example of the analysis yield is shown in (see Figure 46), the figure is shown in semi-log to get a better view of the band gap.

This method is somewhat dependent on how the error is chosen, had the error been just a little larger from the fig it seems the bandgap would close at ~917 nm instead of ~909 nm. From the four structures together the mean lower wavelength is 916 ± 5 nm and the higher 952 ± 8 nm giving an average bandgap span of 36 ± 9 nm. Summing the discrete data points in the band and dividing with the total number

Figure 47: Example of two of the AZT devices that feature band gaps with very different widths, and one reaching into the thousands.

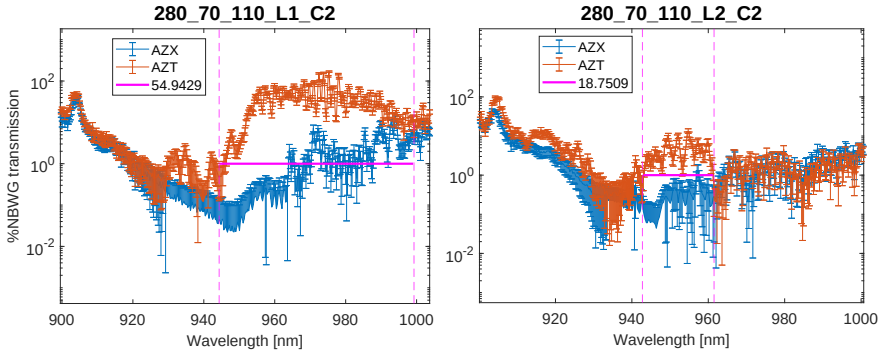

of points in the gap, we get the average edge mode transmission as seen in figure Figure 46.

Some places on the ABX part the lower errorbar is removed. This is due to the errorbar extending below zero which is not displayable in log scale. The results from all 4 structures are in Table 1.

Table 1: The Gap width and transmission of 4 ABT structures with parameters 280_70_110.

Gap Width / Transmission	L1 = 13 µm	L2 = 23 µm
C1	37.5 nm / 9.4 %	38.0 nm / 7.8 %
C2	41.4 nm / 8.2 %	25.8 nm / 9.6 %
Mean	39.5 nm / 8.8 %	31.9 nm / 8.7 %

First thing of note is that the L2_C2 device has higher transmission than its L1 counter part, which is slightly troubling. It does however also seem like the bandgap of that one is more than 1 standard deviation off from the mean gap width, and were it to not be included in the mean calculations it would be almost 7 standard deviations away from the mean. Without excluding the data point the transmission per length coefficient becomes: a = -0.0088 $\pm$ 0.4 [%NBWG/µm]. And with excluding L2_C1: a = -0.1 $\pm$ 0.08 [%NBWG/µm], with the error given as the propagated standard deviation of the spread for the individual sides. With a difference of more than a factor of 10 in the end result, and data fits between two points, this is by no means a complete picture.

There might be differences in transmission between the ABT and AZT devices. Unfortunately the AZT devices feature less straight forward structures, and also had huge variations in bandgaps for structures that should have been the same (see Figure 47).

This could point toward a major fabrication inconsistency for the AZT devices. An example of this device inconsistency can be found in Figure 47. The bandgaps differ by 30 nm. Using the same method

Figure 48: Nanobeam waveguide reference for CTL. Left: the raw CTL scan, featuring significant oscillations at higher wavelengths from shallow etched grating reflections. Right: The smoothed scan taking the average of 25 data points.

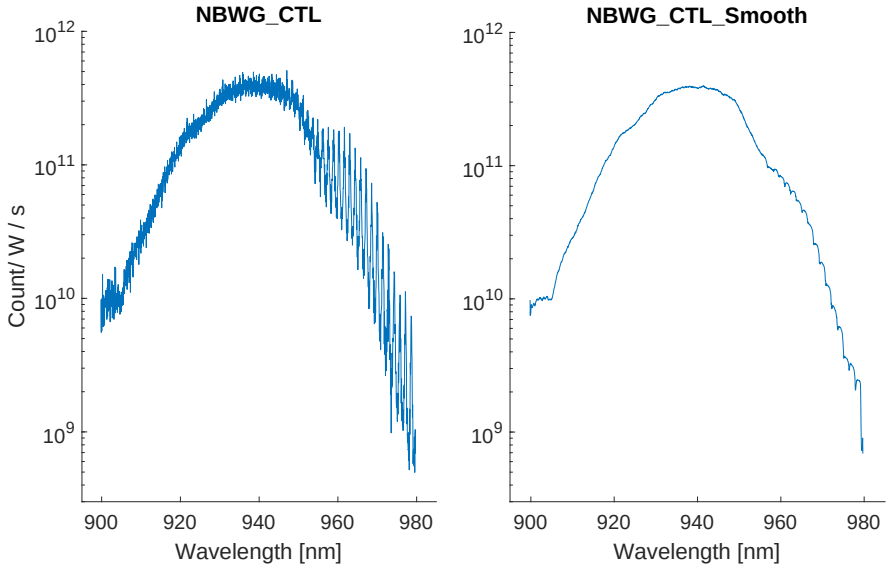

as used on ABT devices the L1 device has an average transmission of 36 % while the L2 device has 4.4 %. While the bandgaps do seem to start close to the same wavelength the L1 device bandgap stretches much further. This could be simply due to the decreased transmission of the L2 device, that the bandgap effectively closes earlier due to the method chosen for this analysis. Other inconsistencies in the AZT devices featured structures with two bandgaps (Figure 57, in Appendix B). I will not look further into the transmission of these devices with this method, since the results are too inconsistent.

5.4 HIGH RESOLUTION CTL SCANS OF TOPOLOGICAL DEVICES

Characterizing structures found from the SuperK measurements in greater optical resolution might reveal additional information, and could also give a more precise measurement of the actual transmission. Therefore measurements henceforth are done with the CTL. It is also nice to confirm the edge mode with not only one type of measurement but actually confirm it with another. The CTL measurements are collected with the APD, and the laser frequency is measured on the wavemeter.

For the CTL study NBWG references are once again employed for all transmission measurements (see Figure 48). Again the NBWG data is smoothed with 25 data points (more points here since it is higher resolution). To get a better idea of the transmission as well the vertical axis will from now on also be displayed in log - to give a better view of what is going on in the topological insulators and non-adapter figures.

Figure 49: Comparison of devices with and without adapters. In red are devices with adapters and they seem to perform remarkably better than those without.

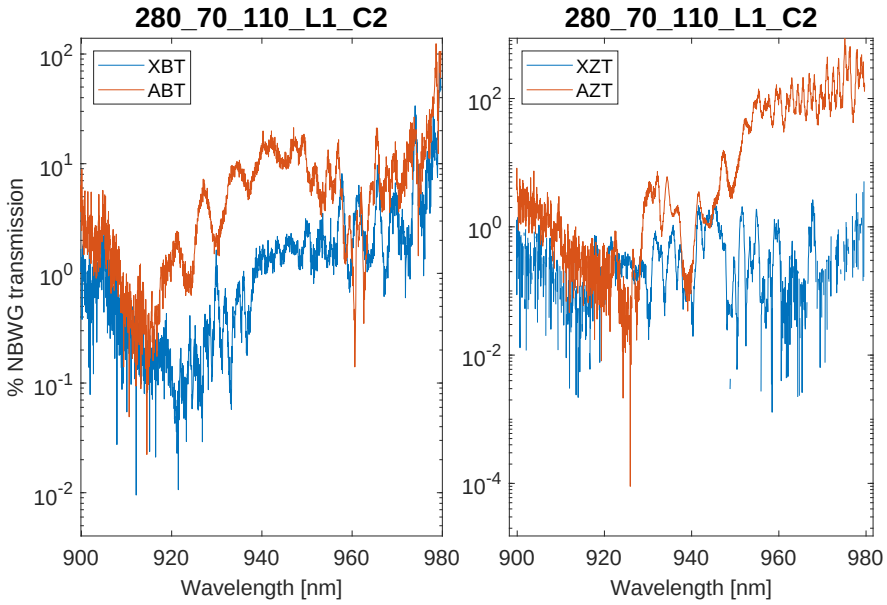

5.4.1 *Adapter versus no adapter*

To see if the adapters works we need to look at the difference in transmission between two devices with interfaces but one with and one without the adapters (see Figure 49). We are not as interested in knowing exactly how much better the adapters are but rather just if they work or not. This is mostly looking towards a new sample in the future to see if a continuation of the adapter is a good idea.

The transmission seems to be increased across the full wavelength span. For the ABT structure across the full span $\frac{\mathrm{sum(ABT)}-\mathrm{sum(XBT)}}{\mathrm{sum(XBT)}} = 6.0$ and for the AZT the same calculation comes out to 25.0. So the adapter seem to overall be a good addition to the structures for improved transmission. However if we wish to know exactly how much it helps the topological mode (which is what is actually important) we have to be more crafty. We know from the SuperK measurements that for 280_70_110 the band gap starts about 916 nm and stops around 952 nm (see Figure 46). Calculating the transmission increase in this range comes out to the edge mode being a 7.5 times increased for the bearded adapter and a 8.7 times increase for the zigzag adapter. This is quite significant and it is definitely worth including adapters in all future topological devices of these kinds.

Figure 50: Two cavity model of the topological devices. Cavity 1 is between the two SEGs of the device, and cavity two is between the two nanobeam-crystal interfaces. The length between the centre of the SEGs L_1 is 73.1 µm, while the length of the crystal L2 depends on the device being either 13 or 23 µm

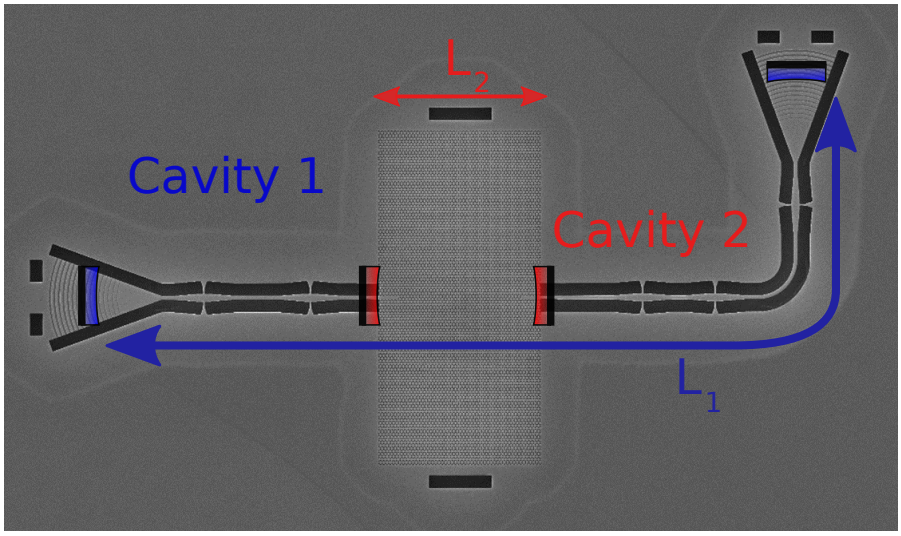

.

5.5 CALCULATING THE GROUP INDEX FROM FABRY-PÉROT INTERACTION

From the previous chapter we learned that the topological edge mode of the devices on this sample are not excellent at efficient light transmission. We can try to turn this to our advantage for characterizing these devices. The lost transmission is an indication that the light is reflected or scatters out of the device in ways we had not planned for. This most likely happens at the interfaces between different parts of the device. We already know (from (Zhou et al. [29]) that the SEGs have increased reflection at higher wavelengths, and we know that using a mode adapter at the interface between the nanobeam and the topological crystal can significantly increase transmission. Assuming that the adapter is not perfect and there is not a 100% transmission at the adapter interface this is the second point of interest. If the reflections are prominent enough, this would result in the device effectively becoming a two cavity system as depicted in Figure 50.

Two cavity systems are difficult to analyse, so ideally finding a work around to avoid having to deal with them is preferable. Luckily the NBWG devices, do not have photonic crystals so they only feature the SEG cavity and can be used for reference. This boils down to a single cavity model which is much more manageable. From the free spectral range (FSR) Equation 6 in Section 1.2.1.1 we can calculate the group index, from the oscillations arising from the cavities FSR:

$$n_g = \frac{\lambda^2}{2L \cdot FSR} \tag{11}$$

Figure 51: Long CTL frequency scan in bulk and its fast Fourier transform. A low pass filter with cut-off "frequency" at 0.0002 nm^{-1} is applied to reduce noisy oscillations.

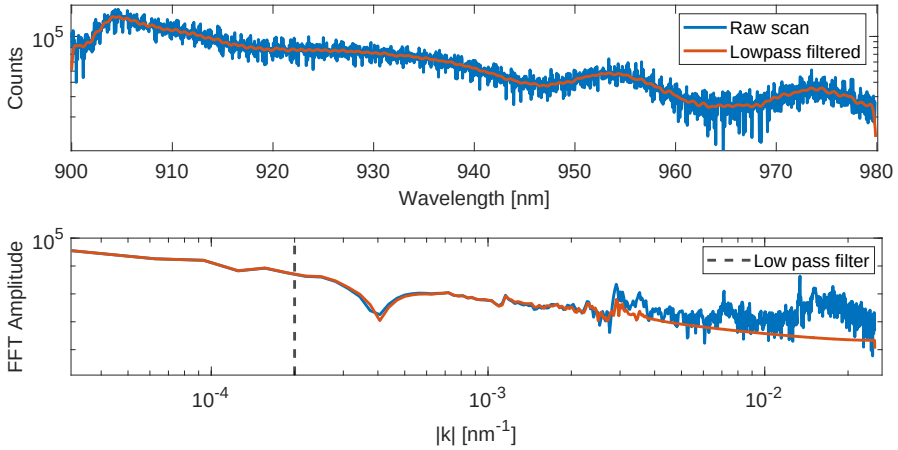

To finely resolve the cavity effect we require very fine scans with the CTL. The optical set-up has decent stability on the >1 hour scales, but going longer requires that we be clever with our methods: First too increase the visibility of the cavity oscillations a measurement of the direct reflection of the CTL laser in bulk is performed while sweeping the laser frequency, this is done at the same resolution as intended of the topological devices. This helps characterize any oscillations of the combined laser and optics set-up, caused by either drifts in the laser power and/or the excitations paths going out of alignment. Doing a bulk scan allows performing a Fast Fourier Transform (FFT) of the data to reveal any rogue oscillations (see Figure 51).

In the FFT a lot of low amplitude noise is visible at the higher "frequencies". A low pass filter at 0.0002 nm^{-1} is digitally applied to the data. The resulting scans are much smoother, and the fast oscillations that have been removed would produce $n_g > 1000$ which is not expected of these structures. This is nice for better visualization of data but it doesn't circumvent the set-up's problem with long scans. From the data gathered it is required that we are able to distinguish peaks, and identify which peaks arise from cavity interaction and which are from random fluctuations, due to instability. The solution used to combat this is to take the same frequency scan three times. Then finding the position of all peaks in the three scans. If a peak appears in one or two out of three data sets it is probably caused by a random fluctuation and not by cavity interaction. The full span the three data points are allowed within each other is set to 0.2 nm or 4 data points with the used resolution, which will be used for error estimation. Due to instability some of the data sets are low count compared to its peers (usually the last scan), in cases where the count on a sample is lower than the Poissonian uncertainty of the other samples it is discarded. Peaks of amplitude lower than the Poissonian uncertainty

Figure 52: CTL scan of nanobeam waveguide with the SEG cavities free-spectral-range utilized to calculate the group index n_g. The data has been normalized to 1 and then a average of the 3 data sets is taken. The group index of nanobeam waveguides is ~ 4.6. The SEGs have higher reflectance at higher wavelengths, which can also be seen in the increased consistency of finding the n_g at higher wavelengths. At wavelengths below ~935 nm the amount of peaks found is significantly decreased. The title of the histogram indicates how many n_g values have been calculated and the device length. The raw scan can be seen in Figure 48.

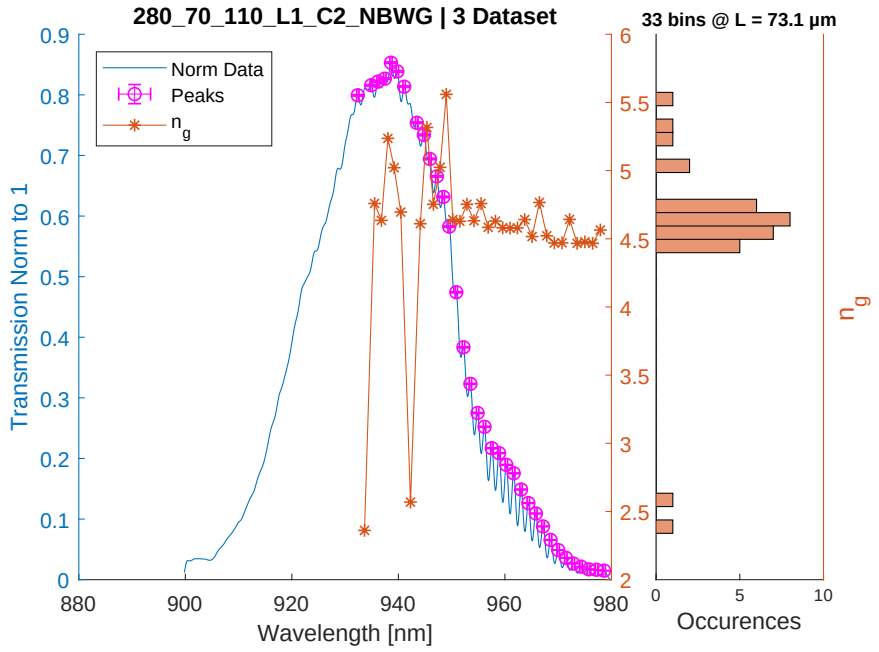

of the peak bin are also not considered. This method is first applied to the NBWG such that it can be used for comparison, see Figure 52.

The group index of refraction of bulk GaAs is ~3.5 which in a NBWG experiences slight Purcell enhancement increasing it to ~4.5, which is within what this method predicts. There are some outliers these can be explained by consistent fluctuations in the set-up not removed by the bulk filtering or simply that there are other effects going on interfering with the ideal cavity model. Figure 52 shows that below ~935 nm the SEGs stop being reflective, making the transmission very smooth. This fact can be used for the analysis of the topological devices. By looking only at oscillations below 935 nm, the two cavity model of the topological structures reduces to a single cavity of the topological crystal. When it comes to the n_g of topological devices we are mostly interested in the group index of the edge mode. Thereby a lower boundary of where to look is also applied. We have looked at 280_70_110 ABT before and found the edge mode to appear between 916 nm and 952 nm. Utilizing this we know to look in the area between 916 nm and 935 nm for the ABT devices. The result can be seen in Figure 53.

Figure 53: Group index analysis of 280_70_110 ABT of different lengths.

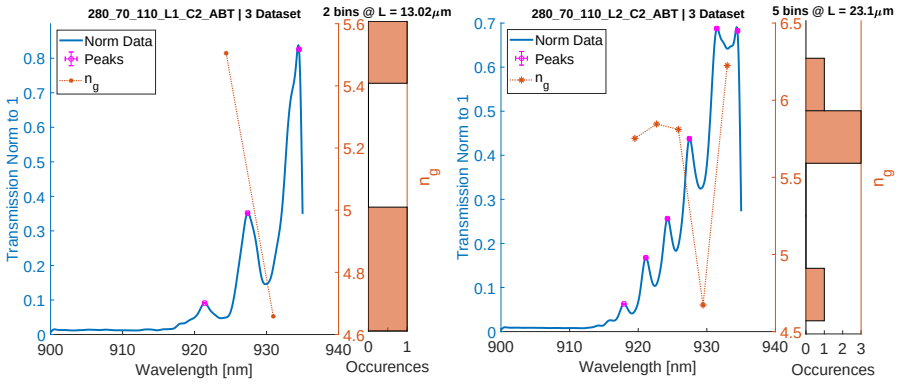

From Equation 11, it can be derived that increasing the length of the device would mean that more free spectral ranges could fit within the 916 - 935 nm window. That is why there are fewer data points for the L1 device than the L2. Both devices seem to agree somewhat that there is some n_g. The amount of data points for L1 are not many, but they somewhat agree with what we see for the L2 device.

5.6 EXPERIMENTAL FINDINGS COMPARED WITH SIMULATIONS

With courtesy of Ph.D. fellow Nils Hauff, we can compare the experimental findings with simulations of the band diagram and n_g of the 280_70_110 structures. From SuperK measurements we learned that the ABT structure has a edge mode between 916 and 952 nm, and from the cavity analysis of CTL measurements we have found the n_gs, both are depicted in Figure 54.

It seems there in general is some systematic error, and also that the error has been slightly underestimated. A systematic error to discuss is the length of the devices. The lengths are measured from the fabrication write file, and not the actual devices themselves. This could mean that the real devices are slightly shorter than what is used for the calculations and would be more prominent for the L2 devices than the L1, shorter devices increases the measured n_g so this might not be the cause of what seems to be an overestimation of the n_g. The estimation of the cavity length is also taken from the start of the crystal to the end of the crystal disregarding the adapters. This is another error on the exact location of the reflection, this however also effectively makes the cavity shorter, and does not seem to be the prominent problem. Both of these errors increase the uncertainty of the n_g by more than the initial error estimation of the n_g given by the allowed peak offsets. Other than that there are also errors on the simulations and although I do not know the exact numbers they tend to be small.

Figure 54: Left: Simulated band diagram of 280_70_110 ABT. To the very top left the light cone is visible, the shaded areas are bulk modes and the blue curve is the edge mode. The bandgap stretches from 312 - 330 THz (~ 908 - 960 nm), and the edge mode emerges from the light cone at 913 nm. The dashed lines indicate where the SuperK measurements predicts the edge mode transmission. Right: Simulated group index of 280_70_110 ABT with n_g calculated from transmission scans. Simulation credit for both figures goes to Nils Hauff.

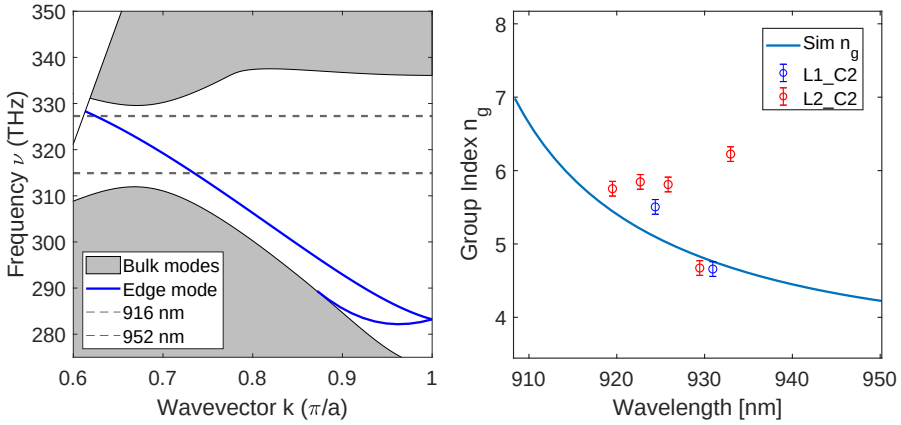

Utilizing the same analysis on the AZT structures leads to results shown in Figure 55. The two individual n_g-analysis figures similar to Figure 53 can be found in Appendix B, Figure 58. From the AZT SuperK measurements it was not possible to confidently identify the edge mode transmission. But the results from the n_g-analysis can still be compared to the simulation.

The AZT structures feature edge mode transmission that can have very high n_g but most of it is located overlapping with bulk transmission, so it would be very hard to identify. Here the n_g of the L2 device seem to be quite close to simulation, while the L1 device is some ways off. For the L1 device it seems more likely that some other stronger effect has come into play and is messing up the n_g measurements. The very high n_g data points that do occur at quite high wavelengths which indicated they might be remnants of SEG cavity action or even that a 3rd and 4th cavity appear between the SEGs and the crystal interfaces. In pure speculation, the longer of the two of such cavities has a length of ~35 nm, which would make the n_g = 16 data point become n_g = 4.8 which is directly on the simulated line. Which could be a strong indication that this the case. The same goes for the data point at n_g=13 but with the other new cavity of length ~23 nm, further supporting this theory.

CONCLUSIONS ON MEASUREMENTS OF TOPOLOGICAL DEVICES

Topological edge mode transmission was identified in multiple topologically interfaced devices when compared to their insulator counterparts. It was displayed that increasing the lattice constant lead to

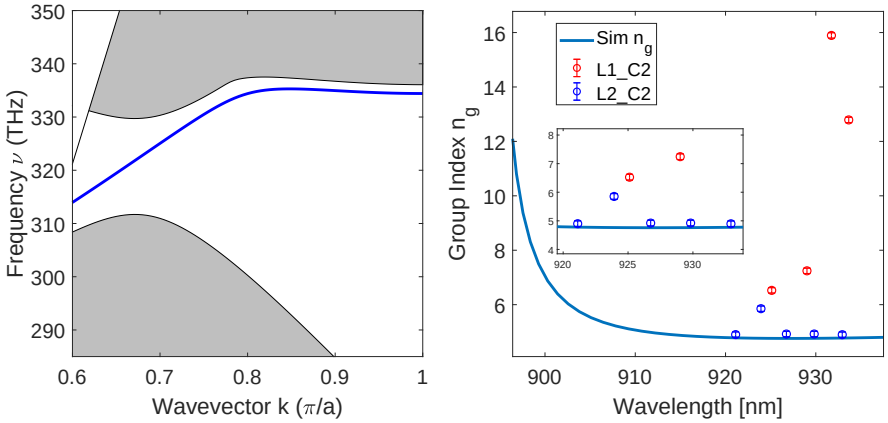

Figure 55: Left: Simulated band diagram of 280_70_110 AZT. To the very top left the light cone is visible, the shaded areas are bulk modes and the blue curve is the edge mode. The bandgap stretches from 312 - 330 THz (~ 908 - 960 nm). Credit for simulation and figure goes to Nils Hauff. Right: Simulated group index of 280_70_110 AZT with n_g calculated from transmission scans. Simulation credit goes to Nils Hauff.

an increase in edge mode transmission centre wavelength. Increasing the circles distance from middle of the shamrocks decrease the centre wavelength and the increasing the radius of the circles also decrease the centre wavelength. Bulk modes for all devices found seemed to not feature bulk modes above 920 nm. From here on focusing on 280_70_110 devices, the bandgap of ABT structures was found to stretch from 916 ± 5 nm to 952 ± 8 nm, while the results of the AZT structures were inconclusive. The mean edge mode transmission of L1 ABT structures was found to be 8.8 % of nanobeam waveguide (NBWG) transmission. In ABT devices increasing the topological crystal length was found to drop transmission by 0.10 ± 0.08 [%NBWG/µm]. While the AZT devices range from 36 %NBWG to 4.4 %NBWG, and probably suffer due to the method of error estimation. Some AZT devices also seemed to feature two topological bandgaps which is out of place for topological structures that must connect the upper and lower band. The two bandgaps are similar to how some GPW structures also feature what looks to be two bandgaps. However, AZT devices do not have parity break and should therefore not share properties with the GWP but rather the PCW. Using CTL the topological adapters were shown to improve edge mode transmission 7.5 times for ABT and 8.7 times for AZT. Using cavity model by assuming shallow etched gratings as mirrors the group index of the NBWG was identified to $n_g \sim 4.6$ which is also the n_g reported for similar devices. Proceeding with the same analysis method but using the topological crystal interfaces as mirrors the n_g of ABT and AZT devices were computed. The calculated n_gs could then be compared to simulated values, revealing a systematic offset and slightly underestimated errors. Compared to simulation the AZT L1 device showed

systematic offsets that match with cavities of lengths comparable to a pseudo-4 cavity model between all permutation of two SEGs and two interfaces.

6

CONCLUSIONS AND OUTLOOK

In this thesis I have presented and characterized three different proposals for advancement in quantum dots and nanophotonic structures towards a quantum internet.

GaAs droplet dots have been investigated for single photon properties and coupling to a photonic crystal waveguide. The dots were found lacking in brightness and linewidth, mainly attributed to high spectral diffusion caused by lack of electric control in the passive sample, combined with a large unoptimized parameter space for the photonic crystal waveguides. Power series with aboveband and quasi resonant excitation show higher saturation power for quasi resonant than aboveband excitation indicative of good coupling to the photonic structure. Single photon properties are probed with g^2 measurements where quasi resonant CW and pulsed measurements are compared yielding $g^2_{CW}(0) = 0.37 \pm 0.07$ compared to pulsed $g^2_P(0) = 0.12 \pm 0.04$ shows that pulsed excitation produces better single photon properties . g^2 measurements also reveal blinking events from regions of enhanced photon bunching the blinking duration is found to 5.79 ± 0.05 µs. The exciton decay rate is measured to $0.741 \pm 0.003 ns^{-1}$. Comparing these values to quantum the state-of-the-art InAs based single photon emitters from (Uppu et al. [8]) the GaAs dot falls short on all parameters. This is not a good single photon source. Additionally, it was possible to excite the biexciton although with an unconventional method, this was confirmed by the decay rate of the biexciton being close to double that of the exciton. With the shortcomings of the sample in mind and more practical lab experience a new sample was designed with the hopes of entangled photon generation through the biexciton cascade, and also being better suited to compete with Uppu et al. with the introduction of gated droplet dots. The measurements here are however not indicative of what others have archived with this breed of quantum dots: Schöll et al. [15] have demonstrated $g^2(0) = (9.1 \pm 1) \cdot 10^{-4}$ which is significantly better than Uppu et al. But from the display of high indestinguishability between photons, it seems that $g^2(0)$ is no longer the limiting factor.

The glide-plane waveguide has been investigated for transmission and quantum dot coupling and control. Transmission measurements reveal one set of devices tuning bandgap nicely, and another set with varying tuning and what seems to be two bandgaps. Resonant transmission measurement of a quantum dot reveals a transmission dip of 21% which can be translated into quantum dot waveguide cou-

pling. Gate voltage tunable resonant fluorescence reveals the quantum dot in the GPW to have a linear response to the electric field tuning 450 ± 30GHz/V. Good control of the glide-plane parameter space has been demonstrated as well decent coupling of a quantum dot to the waveguide. Future measurements would involve measuring the chirality of the waveguide and exciting gated quantum dots in the glide-plane as can be done on the Fawkes21 sample.

Topological edge modes have been identified, and parametric control of the topological edge mode has been demonstrated. The devices with the best found parameters features edge mode transmission of average 8.8 % of what a nanobeam waveguide of similar proportions transmit in its guided mode, dropping with increased crystal length at a rate of 0.10 ± 0.08 [% NBWG / µm]. The bandgap was easily identified for bearded type structures and was found to stretch from 916 ± 5 nm to 952 ± 8 nm. Zigzag type devices had inconclusive results for transmission and bandgap due to multiple bandgaps showing in the data. The introduction of mode adapters between the NBWG and the crystal improves topological edge mode transmission by factors of 7.5 for ABT and 8.7 for AZT.

The group index of the nanobeam waveguide and topological structures was calculated using fine frequency transmission scans for analysis of oscillations in the spectra caused by reflections from the shallow etched grating and the topological crystal interfaces. This allowed comparison of the group index to simulated results, and aside for some systematic errors the method demonstrated good accuracy.

OUTLOOK

Measurements performed on the droplet dot and the glide-plane waveguide have helped the design of Fawkes21, for which I have high hopes for measurements of chiral coupled droplet dots in pursuit of an entangled photon source. Demonstration of a deterministic integrated quantum dot entangled photons source would certainly send ripples through the quantum communications scientific community, and would be a big step towards realization of a quantum internet.

True one directional coupling of a topological photonic structures is yet to be demonstrated, but if it can be harnessed it will be a truly powerful tool for quantum communications. The topological structures featured in this thesis are the first generation from our group, so it is no wonder if they do not perform as well as photonic crystals that have been engineered since theorized in 1975 (Bykov [41]). That said realization of the promises within topological photonics would allow for improved on chip propagation efficiency a value otherwise not thought to be upgradeable in Uppu et al. [8].

To speculate, the full collimation of the work presented in this thesis could lead to a future device featuring droplet quantum dot situated in a ABT device that features chiral coupling and topological protection. This would produce topologically protected path entangled photons which in theory would have high efficiency and consistency from the topologically protected edge mode, and stable quantum states from the low fine structure splitting GaAs quantum dots. This is a paper I will look forward to one day reading or even writing.

A

APPENDIX A: POLARIZATION DEPENDENT AC-STARK SHIFT OF P-SHELL EXCITED QUANTUM DOT IN GLIDE-PLANE WAVEGUIDE

Before doing the lifetime measurement in the GPW chapter a power series of the p-shell excitation was performed. The polarization of the collection is locked to the optimal polarization of the SEGs, but the excitation polarization is varied. A total of four power series are performed changing the excitation polarization as seen in Figure 56. The collection was done on the spectrometer giving quite low resolution. By performing Voigt fits of the spectra at each power and using the centre value of the fits, the resolution can be artificially enhanced. This allows the visualization of the polarization dependent AC-Stark shift. I will not try to speculate in why the quantum dot tunes differently with power, but the result is interesting and i thought it worth to include.

Figure 56: p-shell excitation of quantum dot in glide-plane waveguide featuring polarization dependent power tuning. The individual data points are the centre of Voigt fits performed on the spectra taken by the spectrometer at each power.

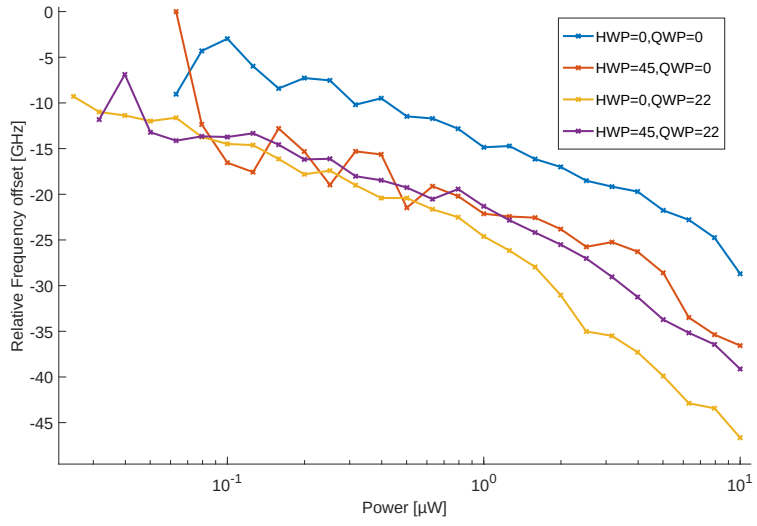

B

APPENDIX B: EXTRA SHOSHIN FIGURES

Figure 57: SuperK transmission spectra of AZT devices. The L1 structures have transmission of their magenta(M) and green(G) bandgaps respectively: L1G: 5.0%, L1M: 3.6 %, L2G: 4.8 %, L2M: 4.6%. Overall giving the L2 structure a higher transmission. Comparing only the green gaps there is a loss of 0.2 % /µW

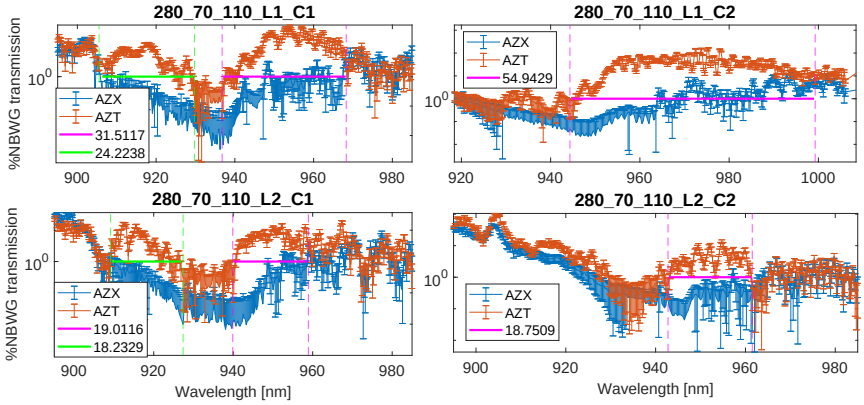

Figure 58: Group index analysis of 280_70_110 AZT of different lengths.

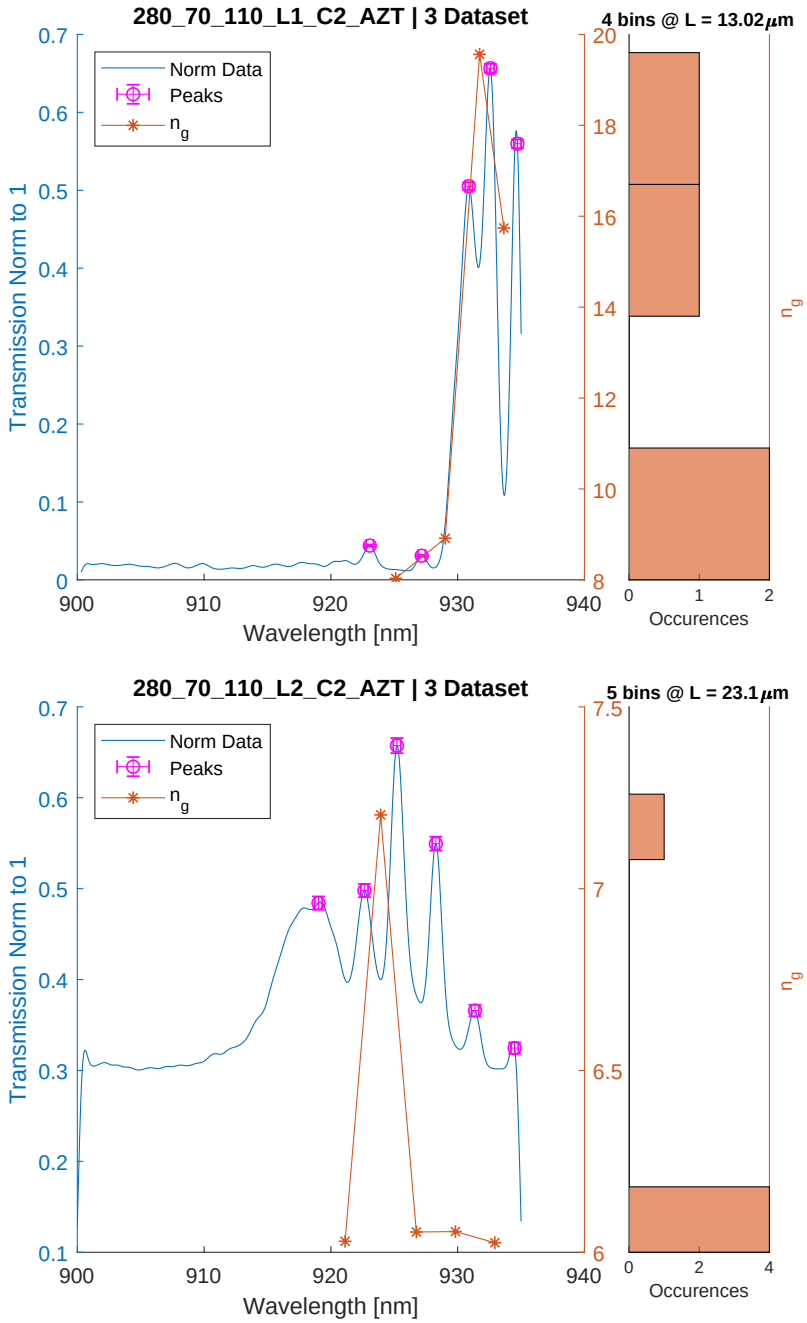

Figure 59: Decay rate measurements of quantum dots on the Shoshin sample, mean value is 0.93 ns^{-1}

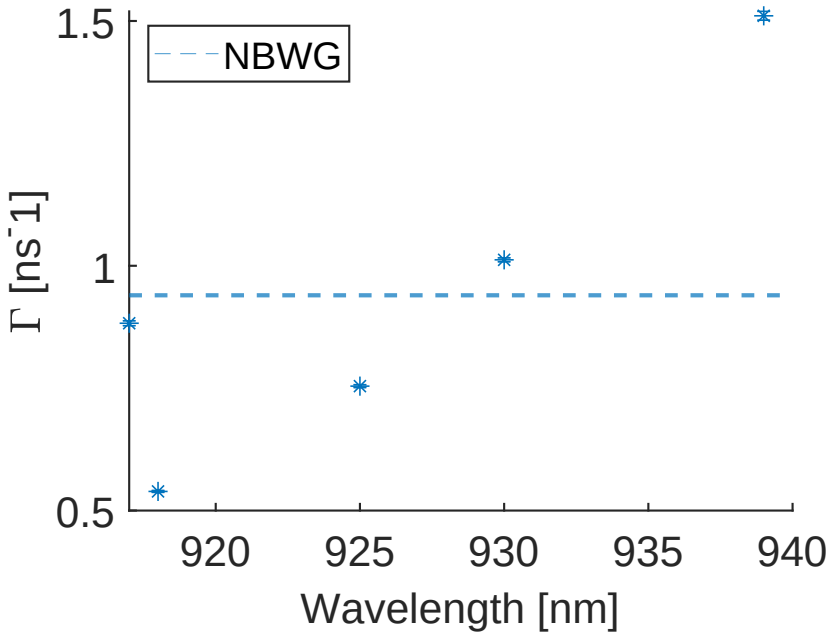

ACRONYMS

Hy-Q center for Hy-brid Quantum networks

QD Quantum Dot

ABB ABoveBand

WL Wetting Layer

Qres Quasi resonant

RF Resonant Fluorescence

RT Resonant Transmission

HBT Hanbury-Brown Twiss

HOM Hong Ou Mandel

SEG Shallow Etched Grating

PCW Photonic Crystal Waveguide

GPW Glide Plane Waveguide

FSS Fine Structure Splitting

FSR Free Spectral Range

APD Avalanche Photo Diode

SNSPD Semiconducting Nanowire Single Photon Diode

NBWG NanoBeam WaveGuide

ABT Adapter-Bearded-Topological

XBT NoAdapter-Bearded-Topological

AZT Adapter-Zigzag-Topological

XZT NoAdapter-Zigzag-Topological

LIST OF FIGURES

BIBLIOGRAPHY

[1] Tim Berners-Lee. *Information Management: A Proposal*. 1989. URL: https://www.w3.org/History/1989/proposal.html.

[2] Frank Arute et al. "Quantum Supremacy using a Programmable Superconducting Processor." In: *Nature* 574 (2019), pp. 505–510. DOI: 10.1038/s41586-019-1666-5.

[3] H Jeff Kimble. "The quantum internet." In: *Nature* 453.7198 (2008), pp. 1023–1030. DOI: 10.1038/nature07127.

[4] Charles H. Bennett and Gilles Brassard. "Quantum cryptography: Public key distribution and coin tossing." In: *International Conference on Computers, Systems and Signal Processing* 175 (1984), p. 8. URL: http://www.sciencedirect.com/science/article/pii/S0304397514004241.

[5] W. K. Wootters and W. H. Zurek. "A single quantum cannot be cloned." In: *Nature* (1982). URL: https://doi.org/10.1038/299802a0.

[6] P.W. Shor. "Algorithms for quantum computation: discrete logarithms and factoring." In: *Proceedings 35th Annual Symposium on Foundations of Computer Science*. Institute of Electrical and Electronics Engineers (IEEE), Dec. 1994, pp. 124–134. DOI: 10.1109/sfcs.1994.365700. URL: https://ieeexplore.ieee.org/document/365700.

[7] Peter Lodahl, Sahand Mahmoodian, and Søren Stobbe. "Interfacing single photons and single quantum dots with photonic nanostructures." In: *Rev. Mod. Phys.* 87.2 (2015), pp. 347–400. DOI: 10.1103/RevModPhys.87.347.

[8] Ravitej Uppu, Freja T Pedersen, Ying Wang, Cecilie T Olesen, Camille Papon, Xiaoyan Zhou, Scholz Sven Midolo Leonardo, Andreas D Wieck, Arne Ludwig, and Peter Lodahl. "Scalable integrated single-photon source." In: *Science Advances* (2020). URL: https://advances.sciencemag.org/content/6/50/eabc8268.

[9] Artur K. Ekert. "Quantum cryptography based on Bell's theorem." In: *Physical Review Letters* 67 6 (1991), pp. 661–663. DOI: 10.1103/PhysRevLett.67.661.

[10] Matthew Pelton Oliver Benson Charles Santori and Yoshihisa Yamamoto. "Regulated and Entangled Photons from a Single Quantum Dot." In: *Phys. Rev. Lett* (2000). URL: https://doi.org/10.1103/PhysRevLett.84.2513.

[11] John D. Joannopoulos Ling Lu and Marin Soljačić. "Topological photonics." In: *Nature Photonics* (2014). DOI: 10.1038/NPHOTON.2014.248. URL: https://doi.org/10.1038/NPHOTON.2014.248.

[12] Robert Keil, Michael Zopf, Yan Chen, Bianca Höfer, Jiaxiang Zhang, Fei Ding, and Oliver G. Schmidt. "Solid-state ensemble of highly entangled photon sources at rubidium atomic transitions." In: *Nature Communications* 8.1 (May 2017), pp. 1–8. ISSN: 20411723. DOI: 10.1038/ncomms15501. arXiv: 1611.03717. URL: www.nature.com/naturecommunications.

[13] Daniel Huber, Marcus Reindl, Yongheng Huo, Huiying Huang, Johannes S. Wildmann, Oliver G. Schmidt, Armando Rastelli, and Rinaldo Trotta. "Highly indistinguishable and strongly entangled photons from symmetric GaAs quantum dots." In: *Nature Communications* 8 (May 2017), p. 15506. ISSN: 2041-1723. DOI: 10.1038/ncomms15506. URL: http://www.nature.com/doifinder/10.1038/ncomms15506.

[14] Eva Schöll et al. "Resonance Fluorescence of GaAs Quantum Dots with Near-Unity Photon Indistinguishability." In: *Nano Letters* 19.4 (Apr. 2019), pp. 2404–2410. ISSN: 15306992. DOI: 10.1021/acs.nanolett.8b05132. arXiv: 1901.09721. URL: https://pubs.acs.org/sharingguidelines.

[15] Eva Schöll et al. "The crux of using the cascaded emission of a 3-level quantum ladder system to generate indistinguishable photons." In: (June 2020). arXiv: 2006.05476. URL: http://arxiv.org/abs/2006.05476.

[16] John D. Joannopoulos, Steven G. Johnson, Joshua N. Winn, and Robert D. Meade. *Photonic crystals: Molding the flow of light*. Second edition. Princeton University Press, 2011. ISBN: 9780691124568. URL: http://ab-initio.mit.edu/book/photonic-crystals-book.pdf.

[17] Sahand Mahmoodian, Kasper Prindal-Nielsen, Immo Söllner, Søren Stobbe, and Peter Lodahl. "Engineering chiral light–matter interaction in photonic crystal waveguides with slow light." In: *Optical Materials Express* 7.1 (Jan. 2017), p. 43. ISSN: 2159-3930. DOI: 10.1364/ome.7.000043. arXiv: 1610.01046. URL: http://dx.doi.org/10.1364/OME.7.000043.

[18] Nicolas Gisin, Grégoire Ribordy, Wolfgang Tittel, and Hugo Zbinden. "Quantum cryptography." In: *Rev. Mod. Phys.* 74 (1 Mar. 2002), pp. 145–195. DOI: 10.1103/RevModPhys.74.145. URL: https://link.aps.org/doi/10.1103/RevModPhys.74.145.

[19] J. Marquez, L. Geelhaar, and K. Jacobi. "Atomically resolved structure of InAs quantum dots." In: *Applied Physics Letters* 78.16 (Apr. 2001), pp. 2309–2311. ISSN: 00036951. DOI: 10.1063/1.

1365101. URL: http://aip.scitation.org/doi/10.1063/1.1365101.

[20] Christopher Gerry and Peter Knight. *Introductory Quantum Optics*. Cambridge University Press, Oct. 2004. ISBN: 9780511791239. DOI: 10.1017/cbo9780511791239. URL: /core/books/introductory-quantum-optics/B9866F1F40C45936A81D03AF7617CF44.

[21] S. Seidl A. W. Holleitner M. Kroner C. Lux and K. Karrai. "Rabi splitting and ac-Stark shift of a charged exciton." In: *Applied Physiscs Letters* 92 (3 2008). DOI: https://doi.org/10.1063/1.2837193. URL: https://aip.scitation.org/doi/full/10.1063/1.2837193.

[22] M. Toth I. Aharonovich D. Englund. "Solid-state single-photon emitters." In: *Nature Photonics* 10 (1 Sept. 2016), pp. 631–641. DOI: https://doi.org/10.1038/nphoton.2016.186. URL: https://www.nature.com/articles/nphoton.2016.186.

[23] Freja Thilde Pedersen. "Deterministic Single and Multi-Photon Sources with Qantum dots in Planar Nanostructures." PhD thesis. Oct. 2020.

[24] Y H Huo, A Rastelli, and O G Schmidt. "Ultra-small excitonic fine structure splitting in highly symmetric quantum dots on GaAs (001) substrate." In: *Appl. Phys. Lett.* 102.152105 (2013). DOI: 10.1063/1.4802088.

[25] E. M. Purcell. "Proceedings of the american physical society." In: vol. 69. 11-12. American Physical Society, June 1946, pp. 680–681. DOI: 10.1103/PhysRev.69.674.2. URL: https://journals.aps.org/pr/abstract/10.1103/PhysRev.69.674.2.

[26] R. Hanbury Brown and R. Q. Twiss. "Correlation between photons in two coherent beams of light." In: *Nature* 177.4497 (1956), pp. 27–29. ISSN: 00280836. DOI: 10.1038/177027a0. URL: https://www.nature.com/articles/177027a0.

[27] Camille Papon, Xiaoyan Zhou, Henri Thyrrestrup, Zhe Liu, Søren Stobbe, Rüdiger Schott, Andreas D. Wieck, Arne Ludwig, Peter Lodahl, and Leonardo Midolo. "Nanomechanical single-photon routing." In: *Optica* 6.4 (Apr. 2019), p. 524. ISSN: 2334-2536. DOI: 10.1364/optica.6.000524. arXiv: 1811.10962. URL: https://doi.org/10.1364/OPTICA.6.000524.

[28] C. K. Hong, Z. Y. Ou, and L. Mandel. "Measurement of subpicosecond time intervals between two photons by interference." In: *Physical Review Letters* 59.18 (Nov. 1987), pp. 2044–2046. ISSN: 00319007. DOI: 10.1103/PhysRevLett.59.2044. URL: https://journals.aps.org/prl/abstract/10.1103/PhysRevLett.59.2044.

[29] Xiaoyan Zhou, Irina Kulkova, Toke Lund-Hansen, Sofie Lindskov Hansen, Peter Lodahl, and Leonardo Midolo. "High-efficiency shallow-etched grating on GaAs membranes for quantum photonic applications." In: *Applied Physics Letters* 113.25 (Dec. 2018), p. 251103. ISSN: 00036951. DOI: 10.1063/1.5055622. arXiv: 1809.03189. URL: http://aip.scitation.org/doi/10.1063/1.5055622.

[30] Immo Söllner et al. "Deterministic photon-emitter coupling in chiral photonic circuits." In: *Nature Nanotechnology* 10.9 (Sept. 2015), pp. 775–778. ISSN: 17483395. DOI: 10.1038/nnano.2015.159. arXiv: 1406.4295. URL: www.nature.com/naturenanotechnology.

[31] Gal Harari Midya Parto Jinhan Ren Mordechai Segev-Demetrios N. Christodoulides-Mercedeh Khajavikhan Miguel A. Bandres Steffen Wittek. "Topological insulator laser: Experiments." In: *Science* (2018). DOI: 10.1126/science.aar4005. URL: https://doi.org/10.1126/science.aar4005.

[32] Alexander Tsukernik Yun Xu Mikhail I. Shalaev Wiktor Walasik and Natalia M. Litchinitser. "Robust topologically protected transport in photonic crystals at telecommunication wavelengths." In: *Nature Nanotechnology* (2019). DOI: 10.1038/s41565-018-0297-6. URL: https://doi.org/10.1038/s41565-018-0297-6.

[33] A. Zee. Princeton University, 2016. ISBN: 0691162697. URL: lccn.loc.gov/2015037408.

[34] Di Xiao Xiaodong Xu Wang Yao and Tony F. Heinz. "Spin and pseudospins in layered transition metal dichalcogenides." In: *Nature Physics* (Apr. 2014). DOI: 10.1038/NPHYS2942. URL: https://doi.org/10.1038/NPHYS2942.

[35] Jia-Jun Yuan Hao-Yang Qiu Xiao-Dong Chen Fu-Li Zhao Xin-Tao He En-Tao Liang and Jian-Wen Dong. "A silicon-on-insulator slab for topological valley transport." In: *Nature Comunications* (2019). DOI: 10.1038/s41467-019-08881-z. URL: https://doi.org/10.1038/s41467-019-08881-z.

[36] Tzuhsuan Ma and Gennady Shvets. "All-Si Valley-Hall Photonic Topological Insulator." In: *OSA Publishing* (2016). DOI: 10.1364/CLEO_QELS.2016.FF1D.3. URL: https://tinyurl.com/TopMA2016.

[37] A. W. Walker-P. Kleinschmidt R. Lang T. Hannappel-F. Dimroth M. Niemeyer J. Ohlmann and D. Lackner. "Minority carrier diffusion length, lifetime and mobility in p-type GaAs and GaInAs." In: *Applied Physiscs Letters* 122 (2017). URL: https://aip.scitation.org/doi/10.1063/1.5002630.

[38] U. Fano. "Effects of configuration interaction on intensities and phase shifts." In: *Physical Review* 124.6 (Dec. 1961), pp. 1866–1878. DOI: 10.1103/PhysRev.124.1866. URL: https://journals.aps.org/pr/abstract/10.1103/PhysRev.124.1866.

[39] Jelena Vučković Glenn S. Solomon Edo Waks Charles Santori David Fattal and Yoshihisa Yamamoto. "Submicrosecond correlations in photoluminescence from InAs quantum dots." In: *Phys. Rev. B* (2004). DOI: https://doi.org/10.1103/PhysRevB.69.205324.

[40] R.J. Barlow. *Statistics - A guide to the Use of Statistical Methods in the Physical Sciences*. Wiley, 1991. ISBN: 0471922943.

[41] V.P. Bykov. "Spontaneous emission from a medium with a band spectrum." In: *Soviet Journal of QUantum Electronics* (1975). URL: https://doi.org/10.1070/QE1975v004n07ABEH009654.